Reactive metal–oxide interfaces: A microscopic view

A. Picone*, M. Riva, A. Brambilla, A. Calloni, G. Bussetti, M. Finazzi, F. Ciccacci, L. Duò**

Dipartimento di Fisica, Politecnico di Milano, piazza L. da Vinci 32, 20133 Milano, Italy

Abstract

Metal–oxide interfaces play a fundamental role in determining the functional properties of artificial layered heterostructures, which are at the root of present and future technological applications. Magnetic exchange and magnetoelectric coupling, spin filtering, metal passivation, catalytic activity of oxide-supported nano-particles are just few examples of physical and chemical processes arising at metal–oxide hybrid systems, readily exploited in working devices. These phenomena are strictly correlated with the chemical and structural characteristics of the metal–oxide interfacial region, making a thorough understanding of the atomistic mechanisms responsible of its formation a prerequisite in order to tailor the device properties. The steep compositional gradient established upon formation of metal–oxide heterostructures drives strong chemical interactions at the interface, making the metal–oxide boundary region a complex system to treat, both from an experimental and a theoretical point of view. However, once properly mastered, interfacial chemical interactions offer a further degree of freedom for tuning the material properties. The goal of the present review is to provide a summary of the latest achievements in the understanding of metal/oxide and oxide/metal layered systems characterized by reactive interfaces. The influence of the interface composition on the structural, electronic and magnetic properties will be highlighted. Particular emphasis will be devoted to the discussion of ultra-thin epitaxial oxides stabilized on highly oxidizable metals, which have been rarely exploited as oxide supports as compared to the much more widespread noble and quasi noble metallic substrates. In this frame, an extensive discussion is devoted to the microscopic characterization of interfaces between epitaxial metal oxides and the Fe(001) substrate, regarded from the one hand as a prototypical ferromagnetic material and from the other hand as a highly oxidizable metal.

Keywords: Scanning tunneling microscopy and spectroscopy; X-ray photoemission spectroscopy; Molecular beam epitaxy; Metal–oxide interfaces; Oxide surfaces

Nomenclature

DFT	density functional theory
E_F	Fermi energy
L	Langmuir
LEED	low energy electron diffraction
MBE	molecular beam epitaxy
ML	monolayer
STM	scanning tunneling microscopy
STS	scanning tunneling spectroscopy
UHV	ultra-high vacuum
UPS	ultraviolet photoemission spectroscopy
XMCD	x-ray magnetic circular dichroism
XPS	x-ray photoemission spectroscopy

*Corresponding author. Tel. : +39 02 2399 6089.
**Corresponding author. Tel.: +39 02 2399 6179.
E-mail addresses: andrea.picone@polimi.it (A. Picone), lamberto.duo@polimi.it (L. Duò).

Published Journal Article available at: http://dx.doi.org/10.1016/j.surfrep.2016.01.003

1. Introduction

Interface formation between metals and oxides are one of the most widely investigated topic in physics, chemistry and material science. The reason for this huge interest is that there is almost no technological field in which the metal–oxide interaction does not play a prominent role, including (nano) catalysis [1–3], microelectronics [4,5], magnetic storage media [6], and protective coatings against corrosion [7,8].

From a more fundamental point of view, the metal–oxide interface represents an interesting example of boundary between two materials possessing markedly different and often antithetical electronic and structural properties [9]. As a relevant case, let us mention that a few nanometer-thick (hydro)oxide skin forms at the surface of almost every metal exposed to environmental conditions [10]. The characteristics of this thin surface oxide layer and its interaction with the underlying metallic support are often key factors in determining the physical and chemical properties of metal surfaces.

The material science community has also dedicated a remarkable attention to the investigation, both theoretical and experimental, of heteroepitaxial metal–oxide systems, where, at variance from native oxides, the metal element is different from the cationic species of the oxide phase. Many physical phenomena arising in artificial metal–oxide heterostructures have been reported, spanning from magnetic instabilities [11,12], charge transfer across the metal–oxide interface [13], magnetoelectric coupling in layered multiferroic structures [14], and tunneling-induced spin filtering [15,16], just to mention a few. All these phenomena are intimately connected with the structural and chemical characteristics of the metal–oxide interfacial region. In order to control, and to some extent tuning, the functionalities of these heterostructures, it is of crucial importance to gain an in-depth understanding of the mechanisms driving the formation of metal–oxides interfaces, in terms of both thermodynamical stability and kinetic constraints imposed by the specific preparation method.

Two different classes of systems can be identified, the metal/oxide (M/O) and the oxide/metal (O/M) heterophases, sketched in Fig. 1. These two seemingly symmetric interfaces often possess different structural and chemical characteristics, mainly because different are the experimental procedures exploited for their preparation (see Section 2.1). The O/M interface is grown by depositing ultra-thin (0–10 nm thick) oxide films on metallic substrates, exploiting the so-called reactive deposition, in which metal atoms are deposited in the presence of an oxidizing atmosphere [17]. On the other hand, the M/O interface can be obtained by depositing metallic films on well-defined oxide surfaces [18,19]. In the latter case, in order to alleviate charging problems related to the use of electron-based microscopic and spectroscopic techniques, the oxide layer of the M/O structure is often supported by a metallic substrate. Despite beyond a critical thickness the surface properties of these metal-supported ultra-thin oxide films have proven to mimic those of the corresponding bulk compounds [20,21], for few unit-cell-thick oxide films the influence of the bottom metallic substrate on the M/O properties cannot be neglected, so that the system is better described as a M/O/M layered structure.

Besides the different experimental constraints characterizing their preparation, the O/M and M/O interfaces bear also intrinsic differences, since the surface free energy of oxidic compounds is generally lower with respect to that of metallic elements (see Section 2.1). For this reason, oxide films tend to wet metallic substrates, while metals deposited on oxide surfaces are prone to clustering, or even to being encapsulated by a thin oxide layer. Such a fundamentally different growth mode observed in the early stages of formation of M/O and O/M interfaces can remarkably influence their final morpho-logical and chemical characteristics.

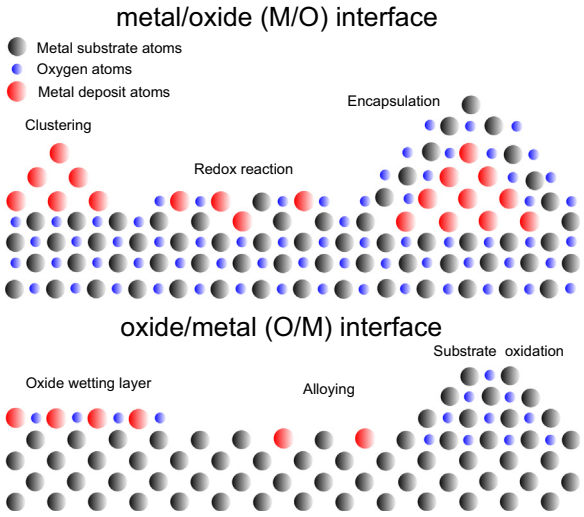

Fig. 1. Metal/oxide (M/O) and oxide/metal (O/M) interfaces. The main phenomena occurring in the early stages of interface formation are displayed.

In this work, we will provide a survey of the mechanisms governing the formation of O/M and M/O interfaces in those cases in which these interfaces cannot be considered chemically and structurally sharp. Of course every real interface is characterized by a certain degree of defectiveness and intermixing, so that a perfectly abrupt metal–oxide interface is not realizable in practice. However, in the present review the focus will be on those cases where *the chemical and structural inhomogeneities at the metal–oxide interface are the prominent driving forces determining the final heteroepitaxial system structure and its physico-chemical properties*. Such chemical and structural inhomogeneities are often regarded as an unwelcome side effects occurring during the preparation of the heterostructures, because the presence of complex phases at the M/O (O/M) boundary makes the interpretation of the experimental data and the theoretical modeling a much more difficult task than for ideally abrupt interfaces. Nevertheless, once properly mastered, such "imperfect interfaces" could represent an opportunity to tune the chemical and physical properties of the nano-structures under consideration.

Particular emphasis will be devoted to the discussion of O/M systems in which the metallic substrate possesses a low electronegativity, i.e. a high oxygen affinity. To this class of materials belong in particular the magnetic 3*d* transition metals such as Fe, Co and Ni, which are largely exploited in spintronic devices and for magnetic storage applications. Due to their high reactivity, little is known about the atomic scale mechanisms driving the formation of epitaxial oxide on these substrates, as compared to the large body of literature focusing on the preparation and characterization of ultra-thin oxide films on inert materials such as noble and quasi noble metals.

The review is organized as follows. In Section 2 the main physical processes driven by the chemical reactions occurring at the M/O and O/M interface are introduced. Section 3 describes the growth and characterization of ultra-thin oxides stabilized on highly oxidizable substrates. Section 4 focuses on transition metal oxides grown on Fe(001), a topic which has been thoroughly investigated by the authors. Conclusions and perspectives are given in Section 5.

2. Physics and chemistry at reactive metal–oxide interfaces

2.1. Interface chemical reactions

The main chemical interaction between a metal and an oxide upon interface formation is the redox reaction, in which few atomic planes of the metallic layer in contact with the oxide surface become oxidized, while the oxide cations reduce their oxidation state. The process is driven by charge transfer and migration of cationic and/or anionic species across the metal–oxide interface.

Starting from a metallic and an oxide layer, the metal oxidation and the oxide reduction upon interface formation are described by the reaction $M^a + M^bO_y \rightarrow M^aO_x + M^bO_{y-x}$. As already pointed out by Campbell [18] and Fu et al. [19] for the M/O interface, the most appropriate parameter to understand whether a redox reaction can occur upon interface formation is the oxide standard heat of formation per mole of oxygen (ΔH_f^0), which has to be considered for the most stable oxide of the elements involved in the interface formation. ΔH_f^0 corresponds to the energy gain for the formation of an oxide compound starting from molecular oxygen and metal atoms, with all substances in their standard states, at $T = 298.15$ K and $p = 100$ kPa. The lower ΔH_f^0, the higher the energy released during the formation of the corresponding oxide. Table 1 reports the ΔH_f^0 values for some oxide compounds that will be discussed in the present review.

Despite the ΔH_f^0 values provide a useful guide to predict if the reaction is thermodynamically favored and can be expected to occur when the corresponding interface is formed, additional considerations should be taken into account. First of all, even in cases where there is no transfer of oxygen atoms from the oxide to the metallic lattice, the metal proximity can influence the stoichiometric composition of the oxide interfacial layer, as a result of charge transfer from the metal to the oxide layer (or vice-versa). This effect should be taken into account especially for interfaces between oxides and inert metals, such as noble metals, for which the small ΔH_f^0 absolute values of the corresponding oxide compounds would suggest a negligible effect on the oxide composition. Charge transfer is expected to be more significant on reducible oxides, such as transition metal or rare earth oxides. On the other hand, for wide gap insulators such as MgO, CaO, and Al_2O_3, characterized by a high ionization potential and a low electron affinity, the effect is limited [24].

A noteworthy phenomenon that might be observed in association with charge transfer across an O/M interface is the formation of reduced species in the interfacial oxide region. This might happen, for instance, when Au, for which ΔH_f^0 is positive (i.e. the oxidic compound is not stable [18]), is employed as a substrate for the stabilization of ultra-thin oxides. As an example we might mention the MoO_3/Au interface, where Mo cations are reduced from a 6+ to a formal 5+ oxidation state [25]. Another case is represented by

Table 1
Standard enthalpy (heat) of formation ΔH_f^0 per mole of oxygen at $T=298.15$ K and $p=100$ kPa. The more negative ΔH_f^0, the more energetically favored the oxide formation. Adapted from [22].

Oxide	ΔH_f^0[kJ/(molO)]
Co_3O_4	−222.75
CoO	−237.9
NiO	−240.6 [23]
FeO	−272
Fe_2O_3	−274.7
Fe_3O_4	−279.6
MoO_2	−294.4
WO_2	−294.8
Cr_2O_3	−379.9
Cr_3O_4	−382.75
MnO	−385.2
BaO	−548
Al_2O_3	−558.57
MgO	−601.6
CaO	−634.9

TiO_2 ultra-thin films grown on Au(100), which are characterized by the presence of reduced oxide species (Ti^{3+} ions) at the interface, as deduced from the evolution of the lineshape of the Ti 2*p* XPS peaks as a function of the oxide coverage [26]. The WO_3 wetting layer covering a Pt(111) substrate is also characterized by the presence of tungsten atoms with a reduced (5+) oxidation state [27].

Similarly, for the reverse case of M/O interfaces, De Masi et al. [28] and Benedetti et al. [29] found that Au deposited on the NiO(001) surface induces the reduction of a small fraction of surface Ni atoms from the oxidation state +2 to 0. Analogous results were obtained for Ag nanoparticles deposited on stoichiometric CeO_2(111), where the Ag-induced reduction of Ce cations from the oxidation state +4 to +3 has been detected [30].

Charge transfer can also promote the stabilization of oxide layers where the cation is characterized by a *higher* oxidation state than the one it typically assumes in stable bulk oxides. For instance, vanadium oxide thin films possessing a formal VO_3 stoichiometry have been grown on Rh(111) [31,32]. Since the maximum oxidation state of vanadium is 5+, electron transfer from the metallic substrate to the oxide overlayer has been invoked to explain such a high oxidation state. Similarly, charge transfer at the O/M interface has been proposed to explain the formation of highly oxidized Co oxide islands on Au(111) [33]. More specifically, investigating the influence of oxygen pressure on the structural and chemical composition of Au(111)-supported Co oxide islands, Walton et al. found that CoO islands are mainly stabilized at low oxygen pressure, with Co cations in a 2+ oxidation state. When Co deposition is performed at higher oxygen pressures, an extra layer of oxygen atoms is added at the interface with the Au (111) substrate, resulting in a trilayer O–Co–O structure, with Co cations in a formal 3+ oxidation state [33].

Beside charge transfer, a second issue to be considered to understand M/O and O/M interface formation is that these apparently identical interfaces often do not display the same chemical composition. As we mentioned in the Introduction, this stems from the different preparation protocols. Generally, metal-supported ultra-thin oxide films are grown by reactive deposition, i.e. by means of MBE performed in an oxidizing atmosphere, while M/O heterostructures are obtained by direct metal evaporation onto well-defined oxide substrates in UHV conditions. The main difference between these two procedures consists in the different oxygen availability during the growth, as well as its physical and chemical states (gas in the case of reactive deposition, bound to cations in the case of metals deposited on oxide surfaces).

A paradigmatic example of such an asymmetry can be recognized in the case of NiO/Fe (Fe/NiO) interfaces. The interfacial structure of ultra-thin Fe films deposited on NiO has been deeply investigated by means of spectroscopic and diffraction techniques [34–39], as well as modeled by *ab initio* DFT calculations [37,40]. These studies reveal that, upon Fe deposition on the NiO(001) surface, an interfacial FeO layer is formed and NiO is reduced to metallic Ni, with the formation of an alloyed NiFe layer [37].

On the other hand, the reverse NiO/Fe interface, obtained by means of reactive deposition of Ni on the Fe(001) surface, is characterized by the development of a thick Fe_3O_4 oxide [41–43], while no metallic Ni is detected at the interface [42]. Upon annealing, Fe_3O_4 reduction to FeO is observed, along with the reduction of NiO and dissolution of Ni atoms into the Fe(001) bulk [42,41]. The different chemical compositions of Fe/NiO and NiO/Fe interfaces can be easily rationalized considering that, in the reactive deposition of NiO on Fe, the evaporation of metallic Ni is performed at a rate of about 1 ML/min in an oxygen background typically of 10^{-6} mbar. In these conditions, the ratio between the flux of oxygen molecules and of metal atoms impinging on the surface is about 45. The substrate is thus covered by its native oxide film before a significant amount of Ni is deposited.

Owing to the similar heat of formation and preparation procedures, CoO/Fe (Fe/CoO) heterostructures behave similarly to the NiO/Fe (Fe/NiO) systems. While metallic Fe deposited on the CoO(001) surface reacts forming a thin FeO layer [44] and a CoFe alloy [45], reactive deposition of CoO on the Fe(001) surface leads to the formation of thicker Fe oxides with higher oxidation states [46,47].

An extensive substrate oxidation has been reported also in the case of the TiO_2/Fe(001) interface [48]. Moreover, when the TiO_2 growth is performed at 573 K, a thick Fe_3O_4 layer covers the TiO_2 film. Conversely, a limited amount of Fe oxide forms at the Fe/TiO_2 interface [49]. Upon thermal treatments in UHV, Fe forms metal clusters which are almost completely covered by Ti suboxides [49].

An even richer phenomenology and somehow controversial results can be found in the case of interfaces formed between MgO and Fe(001). While most of the experimental works report on the formation of an atomically sharp Fe/MgO interface [50–52], in line with the lower heat of formation of MgO with respect to that of Fe oxides (see Table 1), in some cases the presence of Fe oxide at the Fe/MgO interface has been reported [53,54]. Concerning the MgO/Fe interface, high

quality MgO films can be obtained by direct evaporation of stoichiometric MgO [55,56], a procedure that allows avoiding the strong Fe oxidation induced by the oxygen atmosphere employed during reactive deposition [57]. Nevertheless, a sub-stoichiometric FeO layer has been found to develop at the MgO/Fe(001) interface [58].

2.2. Interface structure

The structural properties of M/O and O/M interfaces have been investigated by aiming the focus of the discussion mainly on three issues: (i) mesoscopic interface morphology, (ii) thermodynamic properties, described in terms of free energy surface densities, and (iii) lattice mismatch across the interface. Here, by "mesoscopic morphology" we mean the M/O (O/M) structure on a length scale of tens/hundreds of nanometers, including interface roughness, defect density, island size and distribution, etc. The mesoscopic morphology is, to a large extent, influenced by the quality of the substrate and by the specific preparation methods employed to grow the hetero-structure. Surface and interface free energies determine instead the energetic balance of the heteroepitaxial system, driving its morphological evolution during the early stages of growth. Finally, lattice mismatch is directly connected with the microscopic details of the interface formation between materials characterized by different lattice constants. Its role is prominent at high coverages, since the elastic energy stored in the system increases linearly with the film thickness. In the following, for clarity sake, we will artificially try to isolate and discuss the importance of these phenomena in determining the final interface characteristics, however one should always keep in mind that they are intimately interwoven and cannot really be treated separately.

2.2.1. Mesoscopic morphology

Because of the high stability of oxide materials, metal deposition barely affects the mesoscopic morphology of their surfaces, while oxide layers deposited on metallic surfaces generally induce significant modifications of the substrate morphology at the nanometer scale. When oxide layers are stabilized on inert but mechanically soft substrates, such as, for instance, Au or Ag, a remarkable surface etching is promoted by the overlayer. A widely investigated system in which such a process has been observed is the NiO/Ag(001) interface, where the deposition of NiO induces the displacement of Ag atoms from the terraces. The resulting complex interface is characterized by the presence of vacancy islands on the substrate and NiO islands embedded in the topmost layers of the Ag(001) surface [59–65]. Oxide islands embedded in metallic substrates have been observed also for MgO [66,67] and FeO [68] nanolayers grown on Ag(001), as well as for FeO [69] and CoO [70] films deposited on Au(111).

A quasi-unidimensional etching of the substrate characterizes the growth of CoO onto stepped Pd surfaces [71]. Here, the decoration of step edges by CoO nanowires induces the ejection of a fraction of Pd atoms from the outer terrace, resulting in nanowires partially embedded in the upper terrace. Fig. 2(a) displays a large-scale constant-current STM image of the Pd(1 1 23) surface covered by an oxygen overlayer [71]. The substrate mesoscopic morphology is characterized by straight step edges, arranged periodically over the surface. The oxygen overlayer forms a $p(2 \times 2)$ pattern with respect to the substrate unit cell, as visible from the atomically resolved STM image shown in the inset of Fig. 2(a). After reactive deposition of Co, CoO_x rows with a pronounced chemical contrast decorate the step edges. In Fig. 2(c) and (d) these CoO_x quasi-unidimensional nanostructures are delimited by dashed lines. In addition, rod-like structures decorating the CoO_x nanowires are visible, marked with arrows in Fig. 2(b) and ellipses in Fig. 2(d). These rods are arranged periodically along the direction parallel to the step edges, as evident from the Fast Fourier Transform of the STM image displayed in the inset of Fig. 2(b). STS data (not shown) reveal that the rod-like structures are composed by Pd atoms displaced from the substrate upper terrace [71].

Another important issue to be considered for understanding the O/M interface morphology is represented by the substrate roughening induced by the oxygen background employed during reactive deposition. This phenomenon is particularly relevant when highly oxidizable metals are used as substrates (see Section 3), while for metallic substrates with a lower oxygen affinity the effect is less pronounced. However, a remarkable exception is provided by the case of NiO films stabilized on Pd(001) [72]. Despite Pd cannot be bulk-oxidized under UHV conditions [72], the post-oxidation of ultra-thin Ni films (thickness below two ML), deposited on the Pd(001) surface, promotes a considerable degree of substrate oxidation, preventing the stabilization of long-range ordered NiO overlayers. The promotion of Pd oxidation was ascribed to a lowering of the Pd work function induced by the Ni overlayer [72]. On the other hand, a negligible substrate oxidation and well ordered epitaxial NiO(100) layers are obtained if Ni deposition and post-oxidation cycles are performed on an oxygen pre-saturated Pd surface [72].

The roughening of the substrate can be also associated with a modification of the step/terrace morphology. When vicinal surfaces are employed as templates for the stabilization of unidimensional or quasi unidimensional oxide structures, oxygen-induced step bunching or faceting often occurs [73–75]. Step bunching generally has a detrimental effect on the surface mesoscopic order, since step coalescence destroys the periodic arrangement of the steps. An interesting case in which the oxide overlayer stabilizes the step-terrace morphology is represented by nanowires [76] and stripes [77] of Mn oxide grown on Pd(1 1 17), a surface vicinal to Pd(001). After step decoration by Mn oxide wires, the step edges become straighter with respect to those of the oxide-free surface. At higher oxide coverages, a $c(4 \times 2)$ phase is stabilized on the terraces, and the surface is characterized by a sharp terrace-width distribution, for which the mean step–step separation increases from 23–24 Å, characteristic of the Pd(1 1 17) surface, to 28–29 Å.

The mesoscopic order of the oxide film can be also affected by chemical reactions occurring at the O/M interface. Pal et al.

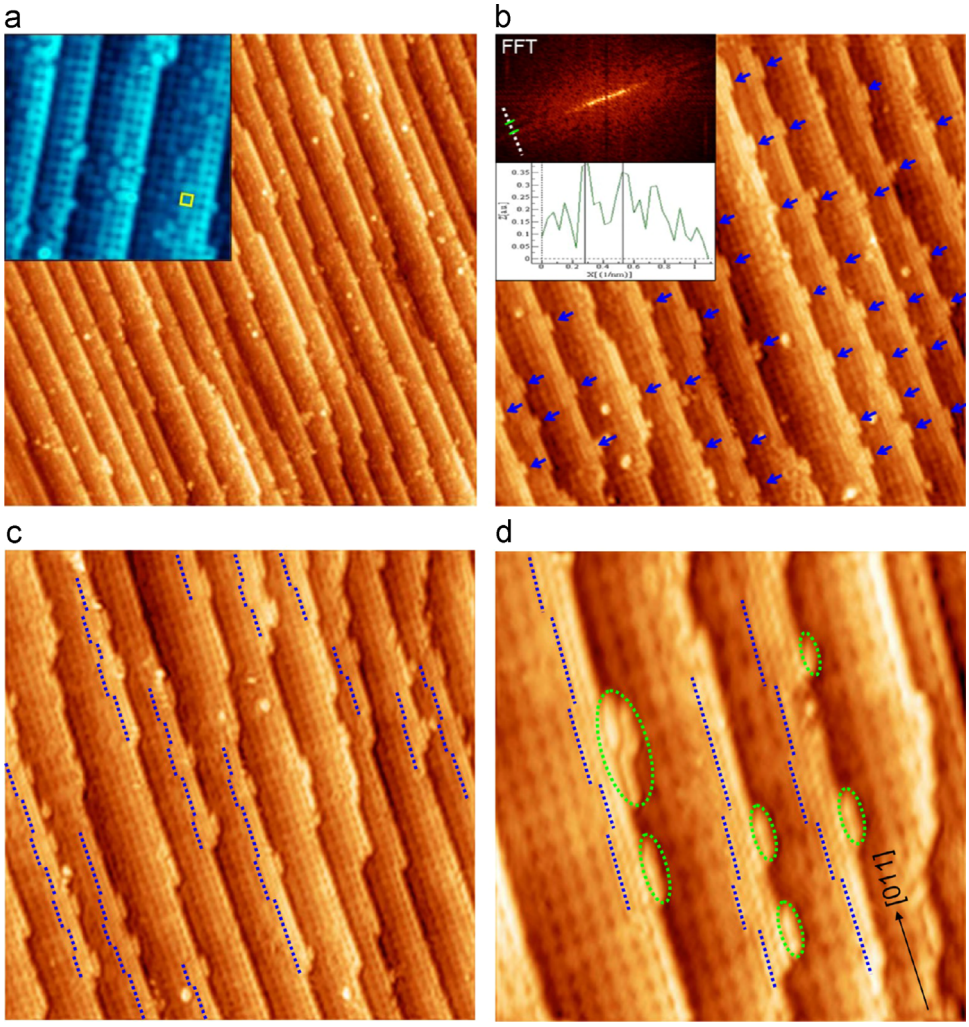

Fig. 2. (a) Pd(1 1 23) surface covered by a $p(2 \times 2)$ overlayer of oxygen. The inset shows an atomically resolved image, in which the $p(2 \times 2)$ unit cell is indicated. (b–d) Surface morphology after deposition of 0.08 ML of CoO_x. Dashed lines and arrows marks the CoO_x nanostructures decorating the Pd(1 1 23) substrate. The ellipses indicate rod-like structures formed by Pd atoms ejected from the outer terrace. The inset of panel (b) displays the fast Fourier transform of the STM image. The line profile (dotted line) is acquired along the direction parallel to the step edges. Reprinted with permission from Ref. [71]. Copyright (2013) by the American Chemical Society.

recently demonstrated the possibility of stabilizing well-ordered MgO ultra-thin films on Ag(001) [78]. After high-temperature reactive deposition followed by a slow cooling, MgO terraces are obtained with a width reaching several tens of nanometers, while different preparation and post-growth conditions induce the nucleation of irregular monolayer islands or bi-layer islands [78]. Fig. 3(a)–(c) displays the morphology of sub-monolayer-thick MgO films stabilized on Ag(001), prepared by following different growth and post-growth protocols. The bottom part of each panel displays STM topographic images acquired at high voltage ($V \geq 3$ V), i.e. by tunneling into the MgO conduction band. In the upper part of the figure, the same surface regions are imaged at low bias ($V = 1$ V), corresponding to an electron energy within the MgO band gap. Panel (a) corresponds to a MgO film grown at moderate temperature (450 K) and rapidly cooled at 200 K. The constant current image displays relatively small islands, few nanometers wide, characterized by irregular borders. The topographic height of the islands [see Fig. 3(e)], measured at high bias voltage, is about 2 Å, corresponding to a thickness of a single atomic layer. In panel (b) the sample was obtained by a high-temperature (773 K) growth followed by a quick cooling to 200 K. The increased growth temperature allows for the development of slightly larger and regular islands. However, in this case the islands are two-atomic-layer high, as testified by the topographic line shown in panel (e). Finally, the surface in panel (c) is obtained by growing the film at high temperature and slowly cooling the sample to 250 K. In this case, large and monolayer-high MgO islands are obtained.

The formation of extended MgO monolayer terraces has been discussed in terms of interface chemistry and post-growth kinetics [78,79]. On one hand, the high deposition temperature promotes the incorporation of oxygen atoms at the MgO/Ag(001) interface. These possibly expand the substrate lattice and reduce the stress of the oxide film, improving its mesoscopic structure. On the other hand, the cooling rate determines whether the system can reach its low-temperature equilibrium state or is quenched into the configuration that is

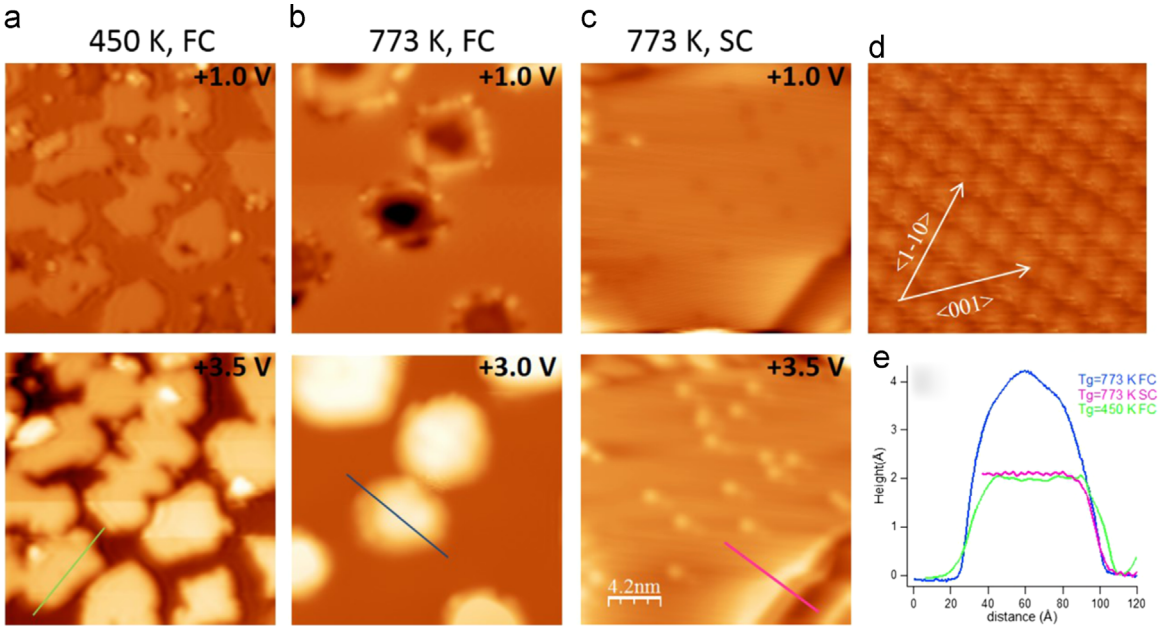

Fig. 3. (a–c) Top and bottom: STM images (21 × 21 nm^2) of 0.7 ML MgO stabilized on the Ag(001) surface at different growth conditions. If the sample cooling after MgO deposition is fast (FC), the film is characterized by the presence of small islands [panels (a) and (b), respectively], independently of the substrate temperature during MgO growth. Conversely, when the growth is performed at 773 K and the cooling rate is slow (SC), the film morphology displays extended atomically flat terraces [panel (c)]. (d) Atomically resolved image of the Ag(001) substrate. (e) Height profiles corresponding to the lines drawn in the bottom panels (a)–(c). Reprinted with permission from Ref. [78]. Copyright (2014) by the American Physical Society.

thermodynamically stable at the high temperature at which the deposition has been performed [78,79].

Interface chemistry is also crucial for the nucleation of FeO islands on Ru(0001) [80]. At low oxygen pressure, monolayer-high FeO islands cover the substrate, while bilayer islands of similar chemical composition nucleate when the growth is performed at higher background oxygen pressures. The nucleation process has been suggested to be driven by how the concentration of oxygen adsorbed on the Ru substrate changes as this oxygen is incorporated into the oxide film. More specifically, at low oxygen pressure, the oxygen concentration on Ru(0001) is limited and monolayer-high FeO islands can form. At higher oxygen pressure, monolayer growth is suppressed, leading to exclusive bilayer island nucleation, which is needed to remove oxygen atoms from the substrate [80].

Table 2
Surface free energies per unit surface of common oxides and metals. The values concerning the metal surfaces are extracted from Ref. [81].

Oxide	γ [J/m^2]
CoO(001) [82]	0.8
Fe_3O_4 (001) [83]	0.96
MgO (001) [84]	0.94
NiO(001) [85]	1.74
Al_2O_3(0001) [86]	2.03
Cr_2O_3(0001) [87]	3.1
Metal	**γ [J/m^2]**
Ag(100)	1.2
Au(001)	1.62
Fe(001)	2.222
Ni(001)	2.426
Co(0001)	2.775
Cr(001)	3.979

2.2.2. *Energetic balance*

The energetic balance, driving the early stages of growth of either M/O or O/M interfaces, is governed by the surface free energy γ, defined as the energy per unit area required to create a surface starting from the bulk material. The modification of the surface free energy $\Delta\gamma$ induced by film deposition on a substrate can be written as $\Delta\gamma = \gamma_{dep} - \gamma_{sub} + \gamma_{int}$, where γ_{dep} (γ_{sub}) are the surface free energies of the deposit (substrate), while γ_{int} is the interface energy per unit area. If $\Delta\gamma < 0$, the formation of a wetting layer is energetically favored, while for $\Delta\gamma > 0$ islanding is observed. If the interaction between the oxide and the metal is weak, the generally lower γ values of oxide surfaces with respect to those characteristic of metal surfaces (see Table 2) steer two-dimensional growth of oxide films on metallic substrates, whereas islanding is observed in the case of metals deposited on oxide surfaces.

The chemical reactions occurring at the M/O interface may change the energetic balance thanks to the lowering of the interface energy term. A stronger adhesion between the metallic overlayer and the oxide surface promotes the formation of a continuous film. An example of chemically induced switching from three-dimensional to two-dimensional growth has been observed in the case of the Co/Al_2O_3(0001) interface [88]. Co films grown on the bare Al_2O_3(0001) surface form three-dimensional clusters, while Co deposited on fully-hydroxylated Al_2O_3(0001) wets the substrate [88]. The two-dimensional growth is triggered by the chemical interaction of

Co atoms with adjacent OH groups present on the hydroxylated surface, with the formation of Co^{2+} ions. The presence of these ions, strongly bound to the substrate, allows the development of smooth Co films.

Similar results were obtained for the Cu/Al_2O_3 interface, which has been theoretically investigated by means of first-principles molecular dynamics simulations [89]. Cu nucleation on the hydroxylated Al_2O_3 surface results in the nucleation of single-layer islands composed by oxidized Cu, while three-dimensional growth is predicted on the anhydrous surface.

Interface smoothness can be improved also by direct spillover of oxygen from the oxide support, as demonstrated in the case of Cr films deposited on the $SrTiO_3$ surface [90]. A three-dimensional morphology develops after Cr deposition at room temperature, while annealing the film at high temperature induces a flattening of the Cr clusters, driven by Cr oxidation and by the consequent enhanced adhesion at the M/O interface.

Another mechanism to promote adhesion at the M/O interface can be represented by charge transfer, either from the metallic substrate on which the oxide is supported or from foreign atomic species dispersed in the oxide matrix. Gold deposited onto thin CaO films grown on Mo(001) forms two-dimensional islands, whereas on thicker CaO films a three-dimensional growth is observed. The two-dimensional growth is promoted by charge transfer from the underlying Mo substrate to the Au/CaO interface [91]. Similar results have been found in the case of Au clusters deposited on MgO thin films supported on Mo(001) [92,93].

2.2.3. Lattice matching

The relevant parameter determining the elastic interaction between the epilayer and the substrate is the lattice mismatch, defined as $f = \frac{a_o - a_s}{a_s}$, where a_o and a_s are the overlayer and substrate lattice constants, respectively. While the crystal structure of most metallic elements can be basically classified into three categories [i.e. the body centered cubic (bcc), face centered cubic (fcc) and hexagonal close packed (hcp) atomic arrangements], the oxidic compounds are characterized by a richer variety of crystal structures. Restricting the discussion to the cubic oxide crystal structures, the most common ones are fcc: rocksalt (where both anions and cations form fcc sublattices), spinel (only anions in fcc sites), and perovskite (anions and low-oxidation-state cations in fcc sublattices). In heterostructures composed by such fcc cubic oxides and fcc metals, the lattice mismatch f for interfaces parallel to the (001) plane can be obtained by directly comparing the oxide and metal lattice constants a_{oxide} and a_{metal}, respectively. On the other hand, for interfaces involving bcc metals, the oxide fcc sublattice should be rotated by 45° around the [001] direction in order match the and the bcc lattice, so that the f value should be estimated by comparing a_{metal} and $a_{oxide}/\sqrt{2}$ (see Table 3 for a list of lattice mismatch values for bcc Fe(001) with respect to the (001) surface of several oxides possessing a cubic unit cell).

The accumulation of elastic energy can be released by the growth of three dimensional islands on top of the wetting layer (Stransky–Krastanov growth) and/or by means of plastic deformations, i.e. by involving the formation of misfit dislocations, found both in M/O [101] and O/M interfaces [102,103]. The dislocations often arrange in an ordered network, developing at correspondence with the coincidence-site lattice between the overlayer and the substrate. The coincidence-site lattice is defined as the superlattice formed by Bravais vectors that the two primitive ones have in common, with a period given by $a_o/|f|$.

Table 3
Mismatch $f_{Fe(001)} = \frac{a_{oxygen} - a_{Fe(001)}}{a_{Fe(001)}}$ between bcc Fe(001) and common cubic oxides. Column a_{oxide} lists the values of the bulk oxide lattice parameter, while a_{oxygen} indicates the size of the unit cell of the square sublattice formed by oxygen atoms exposed at the oxide (001) surface. The lattice constant of bcc Fe is $a_{Fe} = 287$ pm.

Oxide	Structure	a_{oxide} [pm]	a_{oxygen} [pm]	$f_{Fe(001)}$ (%)
CoO [94]	Rocksalt	426.1	301.3	5
Co_3O_4 [95]	Spinel	808.4	285.8	−0.4
NiO [96]	Rocksalt	417.6	295.3	2.9
FeO [97]	Rocksalt	417.2	295.0	2.8
Fe_3O_4 [98]	Inverse spinel	839.4	296.8	3.4
MgO [99]	Rocksalt	421.0	297.7	3.7
$SrTiO_3$ [100]	Perovskite	390.5	276.1	−3.8

The partial modification of the oxide stoichiometry in proximity of the interface region plays an important role in accommodating strain at the metal–oxide interface. For instance, the presence of reduced species at the O/M interfaces has been associated with strain release [104]. This circumstance can be understood by considering that oxides are generally stiffer than metals, thereby the presence of reduced species at the interface can lower the elastic energy stored in the film. In the case of one-layer-thick oxides supported on metallic substrates, also cations deficient films have been observed. Pd(001)-supported transition metal (TM) oxides, where TM is Ni [105], Mn [106], and Co [107], in the monolayer limit form a $c(4 \times 2)$ phase, with TM_3O_4 formal stoichiometry. The $c(4 \times 2)$ phase is obtained by removing one quarter of TM cations from the (001) surface of the stoichiometric rocksalt monoxide. The formation of cationic vacancies partially releases the large lattice mismatch existing between the Pd(001) substrate and the bulk TMO rocksalt (001) surface, allowing for the development of ordered oxide wetting layers [107].

Besides the partial modification of the oxide stoichiometry, the development of mixed phases has also been observed and interpreted as an efficient mechanism to release the strain, as in the case of CaO films grown on Mo [108]. The (001) surface of the rocksalt CaO is symmetry-matched with the (001) surface of bcc Mo(001), but the lattice mismatch between the overlayer and the substrate is substantial (+8.1%). When CaO films are grown on Mo(001) at room temperature, the resulting film is found to be amorphous, while upon annealing the film crystallizes and long-range order is achieved. It turns out that the large misfit is accommodated by a change of the stoichiometric composition at the interface, thanks to the incorporation of Mo ions into the CaO lattice (see Fig. 4). The diffusion of

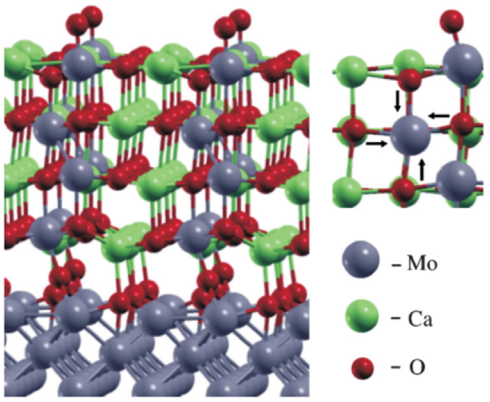

Fig. 4. Proposed model of the reactive CaO/Mo interface, for which the ternary Ca–Mo–O phase forming at the oxide/metal boundary allows an efficient strain release. The right panel displays the inward relaxation of O ions next to a Mo impurity. Reprinted with permission from Ref. [109]. Copyright (2011) by the American Physical Society.

Mo atoms from the substrate allows the stabilization of a ternary Ca_3MoO_4 oxide phase, which possesses an improved lattice matching with the Mo(001) substrate [109].

Strictly speaking, the concept of lattice mismatch applies only when the substrate and the overlayer involved in the interface formation possess the same two-dimensional symmetry. Although this is often the case, many exceptions to this rule can be found in the literature, in particular for O/M interfaces. A large number of experimental works report on the stabilization of oxide films growing with crystallographic orientations that do not follow the substrate symmetry. FeO(111) layers, characterized by an hexagonal surface symmetry, have been stabilized on square substrates such as Pt(001) [110] and Ag(001) [111,68]. Under specific preparation conditions, Co oxide on Ir(001) [112,113] and Mn oxide on Pd(001) [114] have been found to develop with the (111) orientation, notwithstanding the square symmetry of the substrate. The reverse case, i.e. squared oxide overlayers on hexagonal metallic substrates, has also been observed as in the case of MgO(001) stabilized on Au (111) [115]. In these symmetry-mismatched systems, coincidence lattice structures (or moiré patterns) are formed, characterized by periodic long range modulations of the oxide overlayer. On the other hand, similar symmetry-mismatched M/O interfaces have been rarely observed [91], because metallic deposits tend to form three-dimensional clusters on oxide surfaces, hampering the development of long range moiré superstructures.

The interface chemistry can greatly influence the crystallographic orientation of oxide layers stabilized on metallic substrates, as demonstrated in the case of Co oxide nanofilms grown on the Ir(001) substrate [116]. CoO grows on the bare Ir(001) surface exposing the (111) surface, but the crystallographic orientation can be switched to (001) by introducing a thin Co buffer layer between the oxide and the substrate. Fig. 5(a) and (b) displays the LEED pattern and the STM topography of a single-layer defective Co oxide stabilized onto a wetting layer of Co covering the Ir(001) substrate. Both the LEED pattern [panel (a)] and the STM image [panel (b)] show that the Co oxide overlayer forms a $c(4 \times 2)$ superstructure with respect to the substrate lattice, consistent with a formal stoichiometry of Co_3O_4. When the $c(4 \times 2)$ Co_3O_4/Co/Ir (001) system is further oxidized, CoO(001) islands develop on the surface [panels (d) and (e)]. In the LEED pattern [panel (c)] the $c(4 \times 2)$ spots have disappeared and a moiré pattern with a periodicity of about (12×12) is visible, arising from the superposition of diffracted electrons from the CoO(001) overlayer and from the substrate. Panels (f) and (g) display the fourfold symmetric LEED pattern and the STM image obtained after further reactive growth of Co. Both measurements are compatible with the development of a CoO(001) film. Conversely, CoO grown on bare Ir(001) exposes the (111) face, as testified by the LEED pattern and the atomically-resolved STM images displayed in panels (h) and (i), respectively.

Being the Co layer pseudomorphic to the Ir(001) substrate, f is nominally the same for both the CoO/Ir(001) and CoO/Co/Ir(001) epitaxial systems, indicating that the driving force determining the crystal growth orientation resides in the interface chemistry. In particular, the development of the $c(4 \times 2)$ superstructure, related to the presence of cation vacancies, has been suggested to be the key for the stabilization of CoO(001) [116]. A similar effect was recently observed for iron oxide grown on Pt(001), where Fe_3O_4(111) films develop on the bare Pt(100) substrate [117], while the oxide grows exposing the (001) face if a Fe buffer layer is deposited on the Pt(001) surface before oxide deposition [117,118].

2.3. Band alignment across the interface

As a result of the markedly different band structure of insulators and metals, a discontinuity on the electronic energy scale is established at the metal/insulator heterojunction, leading to the development of an energetic barrier for the electrons (or holes) traveling across the interface. The main effect of such a barrier is to produce an asymmetric bias dependence of the current flowing across the interface, leading to the so-called rectifying behavior of the heterojunction. These issues have been extensively discussed in the field of metal/semiconductor heterophases [119], but the increasing interest in all-oxide electronics has boosted a considerable effort towards the study of metal–oxide electronic coupling. In this field, besides the research aiming to achieve an improvement of the carrier mobility, a crucial issue is to find the right metal–oxide combination to obtain ohmic and low-resistance contacts.

In the original model proposed by Schottky, the p-type barrier can be written as $\phi_p = IP - \phi_m$, where IP and ϕ_m are the insulator ionization potential and the metal work function, respectively. The n-type barrier is given by $\phi_n = \phi_m - \chi$, where $\chi = IP - E_g$ is the insulator electron affinity, defined as the difference between IP and the energy gap E_g. However, this model needs to be refined to take into account the presence of interfacial states that can efficiently screen the insulator. The model should thus include an additional term in the Schottky

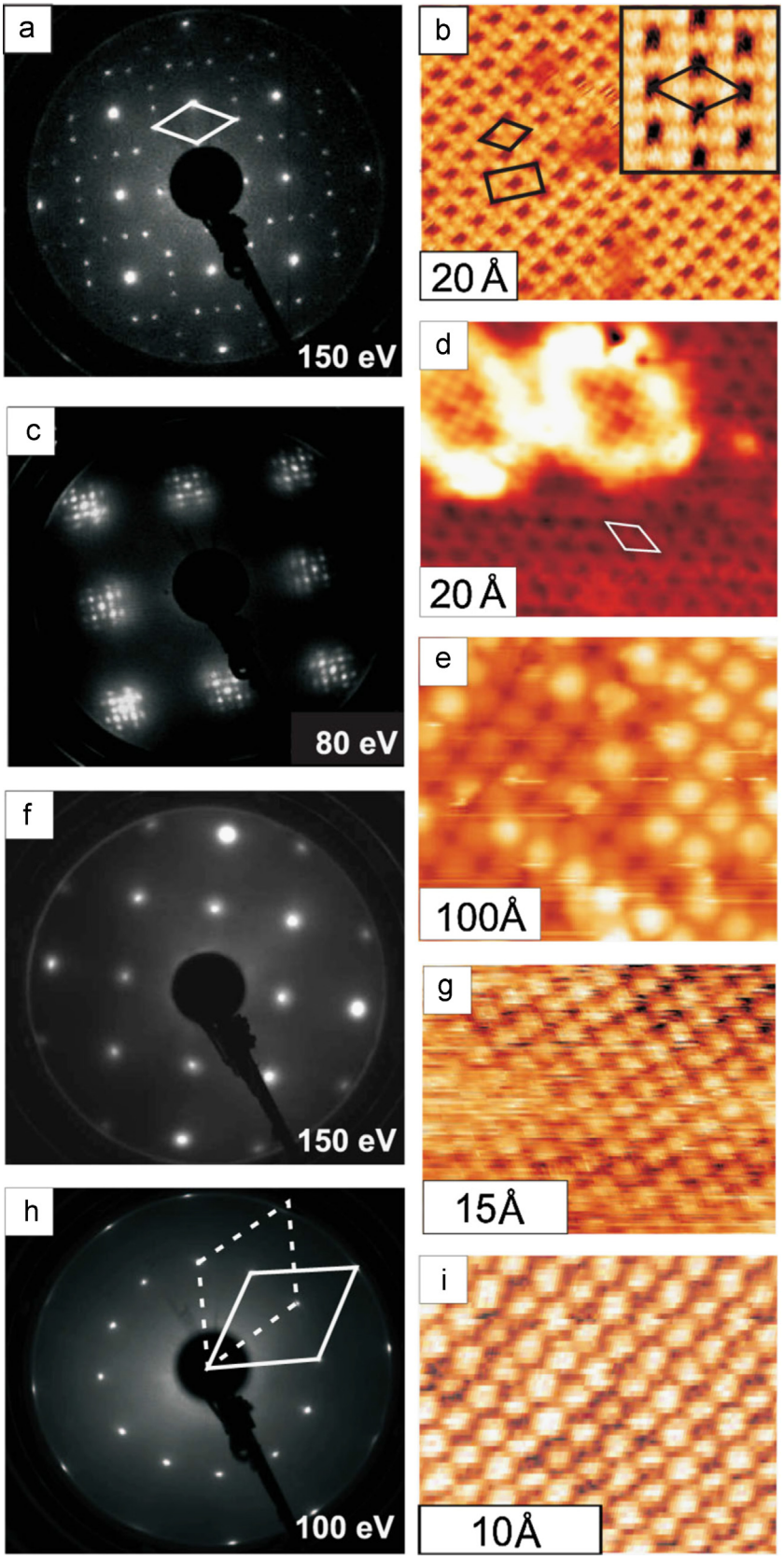

Fig. 5. (a and b) LEED pattern and STM topography of the $c(4 \times 2)$ superstructure developing on the Co/Ir(001) system. (c–e) Reciprocal and real space lattices of the surface obtained after oxidation of the $c(4 \times 2)$ phase. (f and g) Development of CoO(001) upon reactive deposition of Co on the $c(4 \times 2)$ surface. (h and i) LEED pattern and STM topography of CoO(111), developing on the bare Ir(001) substrate. Reprinted with permission from Ref. [116]. Copyright (2012) by the American Physical Society.

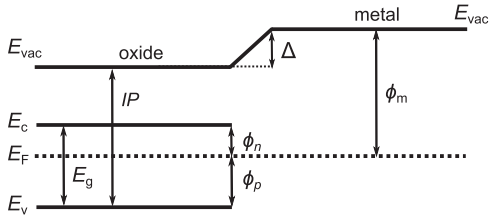

Fig. 6. Simplified scheme of the energy level alignment at the insulator/metal interface. The insulator is considered in flat band conditions. IP= oxide ionization potential, E_F= Fermi level, E_g= energy gap, E_{vac}= vacuum level, E_c= oxide conduction band minimum, E_v= oxide valence band maximum, ϕ_m= metal work function, ϕ_n= n-type barrier, ϕ_p= p-type barrier, Δ= interface dipole.

barrier, related to the presence of an interface dipole Δ (see Fig. 6). In this case the p-type and n-type Schottky barriers are given by $\phi_p = IP + \Delta - \phi_m$ and $\phi_n = \phi_m - (\Delta + \chi)$, respectively. Δ is generally related to the presence of electronic states in the insulator gap, either intrinsic or induced by the presence of the metal. Due to the intimate relation between the interface chemistry and the lining up of the insulator/metal bands, the chemical interactions of metal atoms with the oxide surface are expected to play a prominent role in the determination of the Schottky barrier.

A noteworthy situation where such an influence has been found for the M/O interface is the case of the

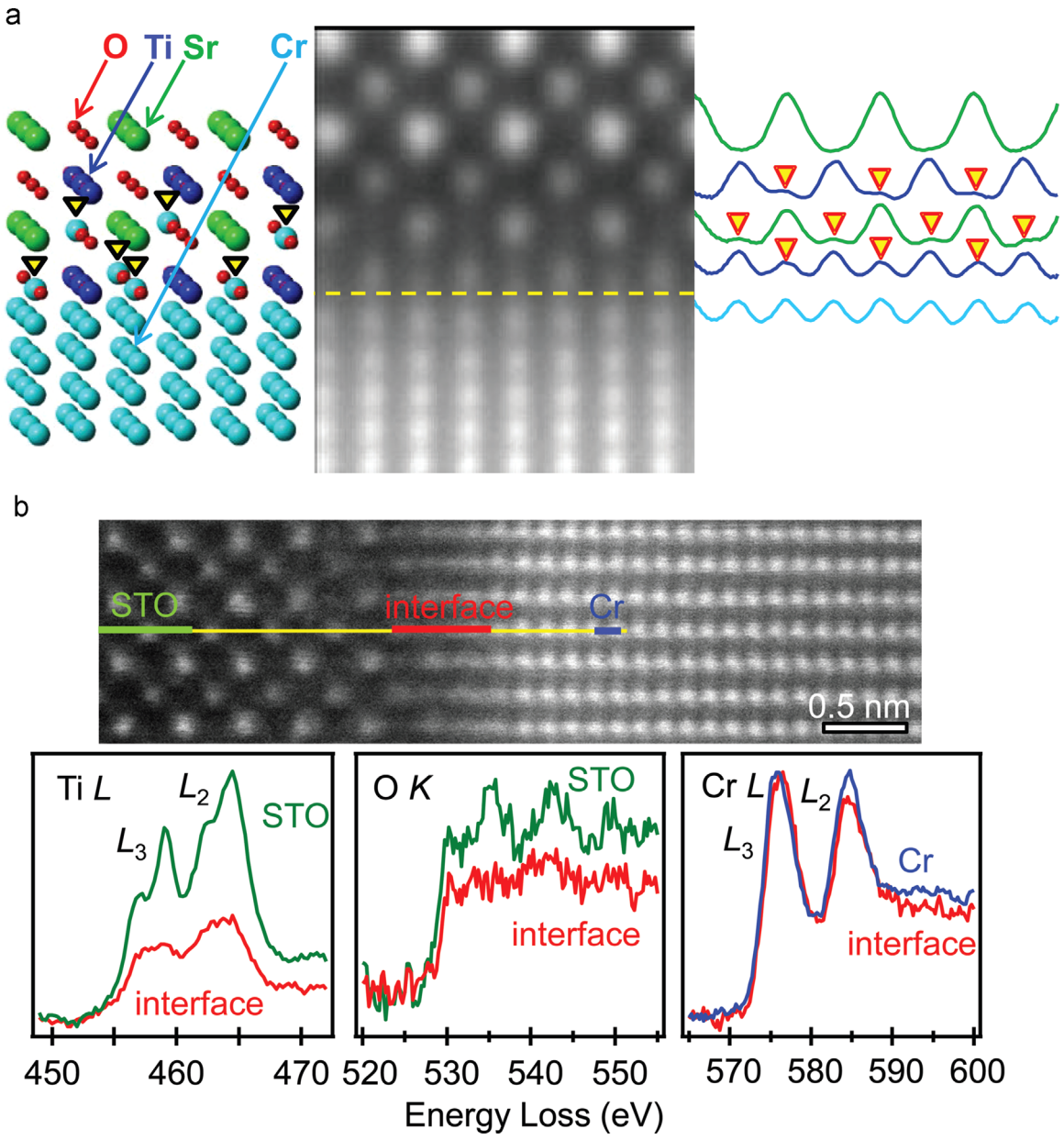

Fig. 7. (a) Single high-angle annular dark-field (HAADF) z-contrast scanning transmission electron microscopy image of Cr/$SrTiO_3$(001) interface (middle). The dashed line marks the interface. The intensity scans acquired at correspondence with different atomic planes parallel to the interface are displayed in the right part of the panel. The structural model (left) of the Cr/$SrTiO_3$(001) interface is characterized by the presence of Cr atoms interdiffused (marked with inverted arrows) into topmost atomic layers of $SrTiO_3$(001). (b) Single HAADF image of the Cr/$SrTiO_3$(001) interface. The Ti L, O K, and Cr L edge electron energy loss spectra collected along the yellow line are displayed in the bottom part of the panel. Reprinted with permission from Ref. [121]. Copyright (2013) by WILEY-VCH Verlag. (For interpretation of the references to color in this figure caption, the reader is referred to the web version of this paper.)

M/$SrTiO_3$(001) heterojunction. While the interface between a noble metal such as Au and $SrTiO_3$(001) is characterized by the formation of a Schottky barrier [120], the Cr/$SrTiO_3$(001) contact exhibits a low resistance and is ohmic [121,122]. This stems from the fact that the epitaxial Cr films do not form an abrupt interface with the $SrTiO_3$(001) substrate, but a fraction of Cr atoms diffuses into it, occupying interstitial sites within the first few atomic planes. At the same time, the Cr atoms become ionized and strongly dope the near-interface region, forcing E_F above the conduction band minimum.

Fig. 7(a) (middle) displays a Z-contrast scanning transmission electron microscopy (STEM) image of the Cr/$SrTiO_3$(001) interface [121]. Intensity profiles acquired on different atomic layers [right panel of Fig. 7(a)] indicate the presence of foreign atoms (marked with inverted arrows), located in the $SrTiO_3$(001) interstitial sites. The foreign species are identified as Cr atoms, based on Cr *L*-edge electron energy loss spectroscopy spectra measured at selected points with a transmission electron microscope along lines perpendicular to the interface [Fig. 7(b)]. A schematic structural model, showing Cr atoms interdiffused within the first two atomic layer of the $SrTiO_3$(001) substrate, is displayed in the left part of Fig. 7(a).

Lenser et al. obtained similar results by comparing the transport properties of M/$SrTiO_3$(001) heterojunctions, where the metallic electrode was either the noble metal Pt or the highly reactive metal Ti [123]. In the former case, the junction was found to exhibit rectifying properties, whereas in the latter the interface exhibits flat-band electronic structure and symmetric $I(V)$ characteristics.

Turning to the O/M case, an example of chemically induced modifications of the Schottky barrier can be recognized in the MgO/Ag(001) interface obtained by Mg reactive deposition [124,125]. Depending on the oxygen partial pressure and the substrate temperature employed during the reactive deposition of ultra-thin Mg oxide films, the *p*-type Schottky barrier has been tuned over 0.7 eV [125]. These remarkable variations of the Schottky barrier were ascribed to the decrease of the silver work function induced by the Mg enrichment of the substrate surface region (associated to the formation of a Mg–Ag alloy) when Mg is evaporated in oxygen-poor conditions or at high substrate temperatures [125,126].

Yoshitake et al. studied the relation between the chemical composition and the band alignment in Al_2O_3/M interfaces, where the metallic substrates were pure metals, Cu(111) and Ni(111), or Al-based intermetallic compounds, Cu-9 at% Al (111) and NiAl(110) [127]. The Al_2O_3/Cu(111) [Al_2O_3/Cu-9 at%Al(111)] and Al_2O_3/Ni(111) [Al_2O_3/NiAl(110)] interfaces have been found to be O-terminated [Al-terminated]. The *p*-type Schottky barrier depends on the interface composition, being larger when the interfaces are Al-terminated. The band offset for the Al_2O_3/NiAl(110) [Al_2O_3/Cu-9 at%Al(111)] interface is 1.7 eV [1.2 eV] larger than for the Al_2O_3/Ni(111) [Al_2O_3/Cu(111)] interface.

The origin of the different band offset observed in Al- and O-terminated Al_2O_3/M interfaces has been discussed in Ref. [128], where the Al_2O_3/Cu-9 at%Al(111) case was analyzed. For an Al-terminated interface, E_F aligns with the Al_2O_3 gap states induced by the presence of Al dangling bonds. The gap states are located slightly above the middle of the Al_2O_3 gap. Therefore, the maximum of the O 2*p*-derived valence band of Al_2O_3 is approximately 4 eV below E_F, resulting in a *p*-type Schottky barrier of about 4 eV. On the other hand, when the interface is established between the O-terminated alumina and Cu, a strong hybridization between the Cu 3*d* and O 2*p* electronic states occurs; this places the O 2*p* orbitals of the alumina valence band near the Cu 3*d* levels. Since Cu possesses a high 3*d* density of states approximately 2 eV below E_F, the *p*-type Schottky barrier falls to the 2 eV range.

2.4. Magnetic coupling

Interfaces between oxides and metals find a widespread application in the field of magnetic layered structures [12,129,130]. Since the magnetic coupling in such systems is mainly driven by the interactions occurring at the interface, it is of paramount importance to have a full control of the interfacial chemical composition. Indeed, the local chemical environment directly influences the spin ordering, since often the oxidic compounds possess a different magnetic order with respect to that of the parent metallic crystals (see Table 4). Magnetic moments are ferromagnetically coupled in Fe, Co and Ni crystals, while the spin structure of the respective rocksalt monoxides is characterized by ferromagnetically coordinated cations with adjacent {111} planes coupled antiferromagnetically to each other. Conversely, Cr bcc crystals exhibit an antiferromagnetic order, while CrO_2 is a half-metallic ferromagnet.

Because of the different chemical composition of the nominally symmetric M/O and O/M heterosystems (see Section 2.1), also the resulting interfacial magnetic order is considerably different. An example can be found again in Fe/NiO (NiO/Fe) heterostructures, where either a thin antiferromagnetic FeO oxide [139] or a ferrimagnetic Fe_3O_4 [41,43] are stabilized at Fe/NiO and NiO/Fe interfaces, respectively. In both cases, the magnetic coupling

Table 4
Magnetic order and magnetic moments (m) expressed in Bohr magnetons (μ_B) for magnetic transition metals and corresponding oxide compounds.

Material	Magnetic order	m (μ_B)
Cr	Antiferromagnetic	0.59 [131]
Cr_2O_3	Antiferromagnetic	2.48 [132]
CrO_2	Ferromagnetic	2 [133]
Fe	Ferromagnetic	2.23 [134]
FeO	Antiferromagnetic	3.32 [135]
Fe_3O_4	Ferrimagnetic	5 (Fe^{3+}), 4 (Fe^{2+}) [136,137]
Co	Ferromagnetic	1.67 [134]
CoO	Antiferromagnetic	3.8 [135]
Ni	Ferromagnetic	0.59 [134]
NiO	Antiferromagnetic	1.9 [138]

between Fe and NiO is not direct, but mediated by the Fe oxide layer in between.

A widely investigated magnetic phenomenon occurring at ferromagnetic metal–antiferromagnetic oxide interfaces is the exchange bias effect. First discovered in 1956 by Meiklejohn and Bean during the study of Co particles embedded in their native antiferromagnetic oxide [140], exchange bias is a general phenomenon occurring in coupled ferromagnetic–antiferromagnetic heterostructures. When the system is cooled through the Néel temperature of the antiferromagnet, unidirectional magnetic anisotropy is induced in the ferromagnetic layer, resulting in a shift of its hysteresis loop. Various theoretical models have been proposed in order to explain the exchange bias effect, many of them involving the presence of uncompensated spins at the interface between the ferromagnet and the antiferromagnet. The atomic spin structure is greatly influenced by the chemical environment, therefore the reactions occurring at the interface are expected to directly influence the number of uncompensated spins. Moreover, since structural defects are responsible for the development of magnetically frustrated regions [141], the chemical composition can also indirectly influence the interface magnetic order through structural modifications at mesoscopic scales.

For instance, Ohldag et al. correlated the presence of uncompensated spins at the Co/NiO interface to the stabilization of an ultra-thin $CoNiO_x$ layer, formed after the Co deposition through reduction of the NiO surface [142]. Bali et al. studied the influence of interfacial Fe oxide on the magnetic properties of CoO/Fe-wedged/Ag(001) samples [47]. Upon CoO growth on Fe films of different thickness (4–16 ML), the interface is found to be characterized by the presence of a Fe oxide layer composed by Fe_2O_3 and Fe_3O_4, with the amount of the interfacial Fe–oxide decreasing with increasing Fe film thickness and saturating for Fe films above 8 ML. The authors found a correlation between the thickness of the Fe oxide layer and the difference in exchange bias field induced by magnetic or zero field cooling, assigned to the evolution of the interface roughness. Młyńczak et al. recently studied the relation between the interfacial Fe oxidation and the exchange bias in CoO/Fe samples grown on MgO [143]. Comparing samples characterized by different amounts of Fe oxides at the interface, it turned out that the shift of the hysteresis loop is related to the interface composition, being larger for the overoxidized Fe(001) substrates.

The chemical interactions occurring at the interface can induce exchange bias even in cases in which the ferromagnet is coupled with an oxide that does not display any magnetic order. Fan et al. studied the magnetic behavior of Fe/MgO, finding that FeO patches formed at the Fe/MgO interface can act as an antiferromagnetic pinning layer, inducing a pronounced exchange bias confined to the interface magnetization [144]. Moreover, the authors demonstrated also the possibility to tune the magnitude of the exchange bias by changing the interface oxygen concentration.

2.5. *Tailoring the interface structure: buffer layers*

A versatile route to tailor the properties of both M/O and O/M interfaces is to deposit a different metallic or oxide thin buffer layer between the substrate and the overlayer, obtaining the different heterostructures ($M/O_a/O_b$, $O/M_a/M_b$, $M_a/M_b/O$, and $O_a/O_b/M$) schematically displayed in Fig. 8. Buffer layers can be exploited to prevent unwanted chemical reactions at the interface or improve the interface morphology.

For what concerns $M/O_a/O_b$ heterostructures, Allegretti et al. employed an oxide buffer layer in order to control the interface chemistry, finding that a sharp boundary between a ferromagnetic metal and an antiferromagnetic oxide can be obtained by inserting a thin CoO buffer layer between a NiO (100) surface and a Co film. XPS spectra reveal that the presence of a 1–2 ML thick CoO buffer layer, covering the NiO(001) surface, prevents its reduction when a submonolayer Co film is deposited [145]. A similar strategy was followed by Masi et al. who investigated, by means of XPS and LEED, the effect of MgO buffer layers deposited on NiO prior to Fe growth [146], finding an almost complete suppression of the NiO reduction characterizing the Fe/NiO interface.

Considering $O/M_a/M_b$ interfaces, metallic buffer layers can be exploited in order to stabilize high quality O/M interfaces between a metal and its native oxide in those cases in which the respective crystal structures are markedly different in terms of lattice mismatch or crystal symmetry. For instance, rocksalt NiO possesses a large lattice mismatch with respect to fcc Ni [147], while thin Ni films grow pseudomorphic on Fe(001), i.e. with the same in-plane lattice constant of the Fe(001) surface [148–150], leading to a good lattice matching with NiO (see Table 3). The crystal structure of bulk Co is hcp, symmetry-mismatched with respect to the rocksalt structured CoO, while high quality tetragonally distorted body-centered-cubic Co films stabilized on Fe(001) [151–153] can be used as a template for obtaining epitaxial CoO layers [154,155]. Mg (whose bulk crystal structure is hcp) has been stabilized in the cubic phase on Fe(001) and then subsequently oxidized to obtain MgO [156]. Finally, a metallic buffer layer can also protect the substrate from oxidation during oxide deposition.

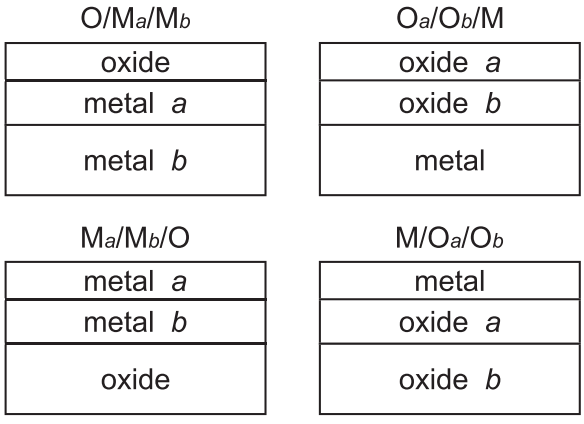

Fig. 8. Schematic representation of the three-layered structures containing a different metallic or oxide buffer layer across the M/O and O/M interface.

Following this line, it has been shown that a thin Mg buffer layer prevents substrate oxidation when MgO layers are deposited on CoFeB [157].

As for $O_a/O_b/M$ layered system, Xue et al. studied the effect of a Fe oxide buffer layers covering a Mo(110) substrate for the growth of polar NiO(111) films. Fe oxide buffer layers improve the NiO(111) growth with respect to the direct growth on the pristine Mo(110) substrate, decreasing the lattice mismatch and lowering the interfacial energy thanks to the chemical reactions occurring between NiO and the iron oxide [158]. A similar strategy, employing a FeO(111) layer grown on Mo(110), was adopted for the stabilization of ZnO(0001) films [159].

Metallic buffer layers covering oxide substrates before the deposition of a second metal ($M_a/M_b/O$) can be useful in those cases in which the top metallic layer is a noble metal, employed because of its high stability under environmental conditions. The weak adhesion between the noble metal and the oxide surface often results in the formation of a remarkable number of pinholes (see Section 2.2.2). The insertion of a reactive metal buffer layer between the oxide substrate and the overlayer can enhance the mechanical stability of the M/O interface. Comparing the morphology of Au films grown on the bare Al_2O_3(0001) surface with that obtained on Co/Al_2O_3(0001), Kamiko et al. observed the formation of highly ordered Au(111) films on the surface covered by the Co buffer layer, while a disordered film develops on the pristine Al_2O_3(0001) surface [160].

The wetting of the metallic overlayer can be enhanced also by using the $M/O_a/O_b$ heterostructure. Nozaki et al. found that inserting an Fe_2O_3 buffer layer on top of the MgO(001) surface leads to the development of flat Fe [161] (Co [162]) films with sub-nanometer thickness, whereas Fe (Co) films grown on the bare MgO substrate form a discontinuous layer due to metal islanding. A flat Fe (Co) morphology allows the establishment of a ferromagnetic long-range order since the early stages of growth, while in the Fe/MgO system the ferromagnetism sets in only at higher coverages, when the Fe clusters coalesce and a closed film is formed [163].

3. Structure and chemistry of ultra-thin oxide films on highly oxidizable substrates

A large body of literature deals with the preparation and characterization of ultra-thin oxide films on noble and quasi noble metals [3]. These films are often exploited for the study of complex chemical processes involved in heterogeneous catalysis. Phenomena like water interaction with oxide surfaces [164–167] and CO oxidation [168,169] have been deeply investigated thanks to the use of these model systems. A prerequisite to successfully rationalize the complex chemical reactions occurring at oxides surfaces relies on the possibility to obtain highly ordered films, allowing their investigation by means of scanning probe techniques [64,170] and a direct comparison with theoretical models [171]. Comparatively, less progress have been made in the characterization of ultra-thin oxides supported by highly reactive metallic substrates. With the term "highly reactive" we refer to metals for which a stable oxide structure is formed for oxygen exposures performed in UHV conditions (up to 10^{-6} mbar).

Such a lack of experimental investigations is partly related to the additional experimental issues encountered when one tries to stabilize an oxide on a highly oxidizable substrates. As a matter of fact, exposure to oxygen can produce severe structural modifications on the substrate, often inducing a roughening of the surface and in turn preventing the development of smooth structures [172]. For this reason, particular care has to be paid for the preparation of well-ordered oxides on such substrates.

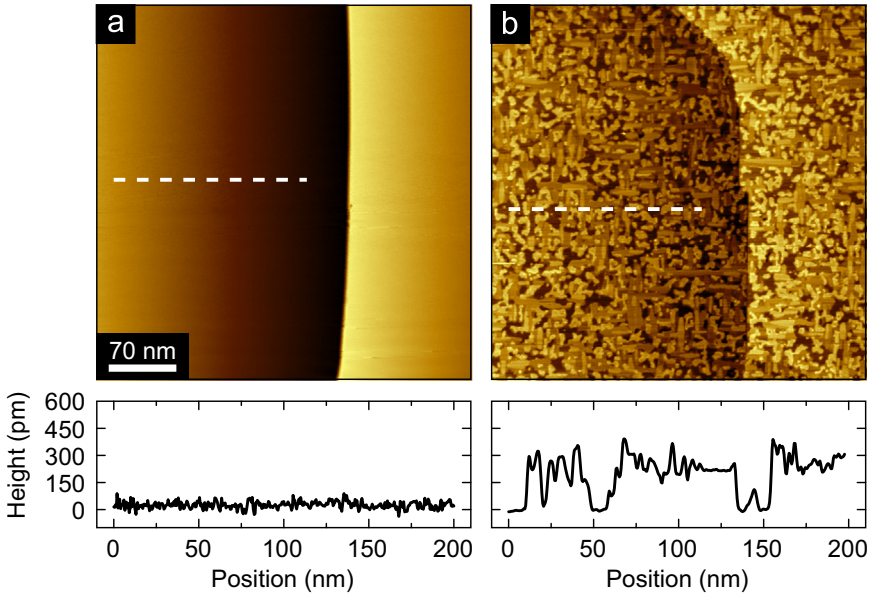

Fig. 9. Oxygen-induced roughening of the Fe(001)-$p(1 \times 1)$O surface. (a) STM topographic image of the Fe(001)-$p(1 \times 1)$O [see Section 4.1]. (b) Morphology obtained after dosing 50 L of O_2 and annealing at 200 °C in UHV.

Fig. 9 exemplifies the surface structural modifications induced on the Fe(001)-$p(1 \times 1)$O surface by oxygen exposure (see Section 4.1). While the Fe(001)-$p(1 \times 1)$O substrate is characterized by atomically flat terraces, after dosing 50 L of molecular oxygen Fe oxide nuclei develop, increasing considerably the surface roughness. The surface roughening, occurring during the early stages of oxygen dosing, is expected to play an important role in determining the structural quality of the heteroepitaxial ultra-thin oxide film, as indeed observed by Tekiel et al. in their systematic study of the influence of the preparation protocol on the growth of epitaxial MgO films on Fe(001) [57]. The MgO crystal quality depends on the ratio between the Mg deposition rate (r) and the oxygen partial pressure (p) employed during the reactive deposition. At low r/p values, the overexposure to oxygen causes an excessive substrate oxidation, resulting in a poorly ordered MgO film, while high r/p values induce the development of understoichiometric MgO films (see Fig. 10).

3.1. Late 3*d* transition metals substrates

In this section, oxide ultra-thin films stabilized on late 3*d* transition metals (with the exception of Fe, to which Section 4 is dedicated) are reviewed. Incidentally, such metals can be either antiferromagnetic (Cr, Mn) or ferromagnetic (Fe, Co, Ni), therefore the interaction with an oxide overlayer can have a strong influence on the interfacial magnetic properties, as highlighted in Section 2.4. Because of their high oxygen affinity, ultra-thin layers of native oxides can be stabilized on late 3*d* magnetic metals by direct exposure to oxygen at relatively low partial pressures. In this case, the crystal quality and morphological order of the oxide overlayer represent a crucial issue, since the oxide crystal structure is generally different with respect to that of the metallic substrate. In addition, when 3*d* magnetic metals are employed as substrates for heteroepitaxial growth, particular care has to be paid in the characterization of the interface chemical state, since cationic species from the substrate are likely to be included in the oxide.

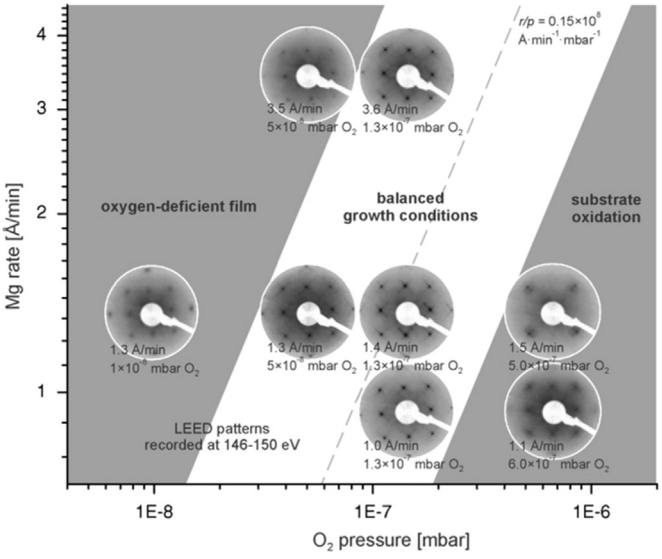

Fig. 10. LEED patterns from MgO thin films stabilized on Fe(001) as a function of oxygen partial pressure (p) and Mg deposition rate (r). The best quality films are obtained for $r/p = 0.15 \times 10^8 \text{Å} \times \text{min}^{-1} \times \text{mbar}^{-1}$. Reprinted with permission from Ref. [57]. Copyright (2013) by Elsevier.

Epitaxial Cr_2O_3 films have been stabilized on the Cr(011) surface [173–178]. Oxygen exposure in UHV conditions performed with the substrate held at relatively high temperatures (603 K) induces the layer-by-layer growth of Cr_2O_3, without any interface roughening [174]. On the other hand, oxidation of the Cr(001) surface produces a polycrystalline oxide film [179].

Oxidation of the Co(0001) surface results in the stabilization of an ultra-thin CoO(111) at low oxygen exposure and Co_3O_4 at higher exposures [180]. Generally, when Co(0001) is employed as a substrate for the deposition of heteroepitaxial oxides, the formation of a thin Co oxide interfacial layer is reported. For instance, the Co(0001) surface has been found to be a suitable substrate for the growth of corundum-structured Al_2O_3. In this case the formation of a CoO thin layer between the Al_2O_3 film and the Co substrate was reported [181]. A 3.5 Å thick Co oxide layer was found also in the interfacial region of ultra-thin chromia films grown on the Co(0001) surface [182]. Wang et al. studied the MoO_3/Co layered system, finding a reduction of the oxidation state of Mo in the interfacial region, along with the formation of Co oxide [183].

The oxidation of Ni(001) above room temperature produces crystallites with a lateral extension of 50 Å [147], while the formation of a continuous NiO(111)-like layer composed by nanosized domains is observed on Ni(111) [184]. The experimental results in the literature concerning the growth of Ni-supported oxide films generally report a very weak substrate oxidation. Ni(001) has been used as a template for the growth of Eu oxide, with a negligible oxidation of the Ni substrate [185,186]. Ni(111) has been used as template for the growth of Al_2O_3 films [187,188]. Also in this case, no remarkable oxidation of the Ni substrate was observed, although Ni-O bonds were detected at the interface. Prevot et al. suggested that the Ni-supported Al_2O_3 oxide films can be regarded as a freestanding oxide layers [189]. Ti oxide [190] and V oxide [191] have been stabilized on Ni(110). In both cases only a weak oxidation of the substrate was reported.

3.2. Refractory metals

4*d* (Nb and Mo) and 5*d* (Ta, W, Re) refractory metals are all characterized by a high melting point (above 2273 K) and a remarkable hardness. Despite the heat of formation of these oxides is comparable with that of 3*d* magnetic metals, the onset of bulk oxidation in UHV conditions is observed only at high temperatures or by employing oxidation promoters, such as rare-earths [192,193] or alkali metals [194]. The reluctance of refractory metals towards oxidation relies on the high kinetic constraints experienced by oxygen atoms during their incorporation into the growing oxide film. Nordlander et al. discussed the correlation between the stiffness of the materials

and the energy barrier for the incorporation of oxygen atoms in subsurface sites. Their findings suggest that the higher the shear modulus, the higher the potential barrier for oxygen penetration through the surface [195]. In this frame, due to their remarkable hardness, refractory metals and their oxidic compounds are expected to display high barriers for oxygen incorporation [196]. Nevertheless, high-quality layers of WO_2 were recently stabilized by high temperature oxidation of the W(110) surface [197]. A structure similar to WO_2/W(110) is found for the MoO_2 oxide layer formed upon high-temperature oxidation of the Mo(110) surface [198].

Thanks to their reluctance towards oxidation, when refractory metals are employed as substrates for the stabilization of heteroepitaxial oxides, the formation of their oxidic phase is seldom reported. The key point for the use of refractory metals substrates is the possibility to explore a large window of temperatures without problems of substrate instability or intermixing between the deposit and the substrate. Mo(001) has been employed as a support for the growth of MgO [199–201] and CaO thin films [108,109], finding in both cases that the best quality films are obtained after high temperature annealing, at about 1000 K. Either TiO_2(100) or Ti_2O_3(0001) epitaxial layers have been grown on the Mo(110) surface, depending on the film preparation method [202]. Similarly, the W(100) surface has been reported to be a good support for the growth of TiO_2(110) layers [203,204].

3.3. Alloys

Among the class of substrates reactive towards oxidation, the case of binary alloys should be mentioned as well. These are characterized by a crystal structure composed by two different metallic elements, A and B. Generally, alloys are employed since their high melting point allows high-temperature treatments, crucial to obtain ordered crystalline structures. The preferred route for obtaining an epitaxial oxide over a binary alloy substrate is typically represented by the direct oxidation of the surface. If the atomic species B possesses a larger oxygen affinity with respect to A, the oxidation will primarily induce the segregation and oxidation of B atoms, producing a BO_x layer covering the surface [205–207]. In this case the alloy should release the reactive metal slowly, so that the oxidation process takes place at a moderate rate, which constitutes a crucial prerequisite for the formation of good-quality crystalline oxide films. As an example, Pt_3Zr(0001) [208] and Pd_3Zr(0001) [209] substrates have been exploited to grow well-ordered ZrO_2 films by means of post oxidation.

The paradigmatic example of an oxide supported by an alloy substrate is represented by the binary compound NiAl, employed as a substrate for the stabilization of well-ordered Al_2O_3 films. While direct oxidation of Al surfaces produces amorphous layers [210,211], high-temperature oxidation of either NiAl(110) [212,213] or Ni_3Al(111) [214] induces the formation of high-crystal-quality Al_2O_3 films. Al_2O_3 has been stabilized also by oxidation of Cu-9 at%Al(111) [215].

Surface-confined alloys, obtained by deposition of metallic films on metallic substrates, have also been used as a template for the stabilization of ultra-thin oxide films. The oxidation of a Ti–Au alloy formed at the Au(111) surface induces the development of TiO_2 nanocrystals [216], while Co oxide develops from the oxidation of a surface-confined Co–Pt alloy grown on Pt(111) [217].

4. Ultra-thin oxides on Fe(001)

4.1. Fe(001) and Fe(001)-$p(1 \times 1)$O substrates

Fe(001) substrates are available in the form of whiskers [218–220] or bulk single crystals [220]. In addition, high quality Fe(001) surfaces can be obtained by depositing thick Fe films (thickness above 100 nm) onto a polished MgO substrate by means of MBE [221]. Such Fe(001) films display the same properties of bulk iron, but compared to Fe(001) single crystals are cheaper and much easier to clean from contaminants.

The Fe(001)-$p(1 \times 1)$O surface, characterized by a single layer of oxygen atoms adsorbed on the fourfold hollow sites of Fe(001), can be obtained by dosing molecular oxygen onto the clean Fe(001) surface and annealing the sample at high temperatures (above 700 K). Although several preparation methods can be found in the literature, mainly differing in the oxygen amount employed to saturate the clean surface (ranging from 0.6 L [222] to 30 L [223]), according to Lu et al. the final heating step annihilates any surface disorder induced by oxygen overdosing, leaving just one well-ordered layer of oxygen atoms [224].

Fig. 11 displays the effects induced by the oxidation process and high-temperature annealing on the Fe(001) mesoscopic morphology [223]. The oxygen-free Fe(001) sample is characterized by relatively small terraces (average width equal to about 30 nm) separated by monoatomic steps (with a topographic height of 143 pm). Screw dislocations arising from strain relaxation are visible on the surface. Oxygen adsorption and subsequent annealing induce a noticeable mass rearrangement over the whole surface, and the Fe(001)-$p(1 \times 1)$O reconstruction displays wide atomically flat terraces (average width equal to about 140 nm), separated by multilayer steps. The product between the step density and the mean step height before and after oxidation is the same, indicating that the mesoscopic structure of the Fe(001)-$p(1 \times 1)$O surface results from the bunching of the steps present on the pristine Fe(001) surface.

At the atomic level, oxygen atoms arrange in a highly ordered overlayer, in registry with the substrate [225–227]. The oxygen-induced enhancement of the atomic corrugation allows the achievement of atomic resolution on the Fe(001)-$p(1 \times 1)$O substrate, difficult to obtain on the clean Fe(001) surface [228,229]. The atomically resolved STM image acquired on the Fe(001)-$p(1 \times 1)$O, displayed in Fig. 12, shows that large defect-free regions are present on this surface. The oxygen atoms reside in the fourfold symmetric surface hollow sites, protruding slightly above the Fe(001) topmost layer. Since the oxygen overlayer is not coplanar with the Fe(001) surface layer, an electric dipole directed normal to the surface appears. As a consequence, the surface work

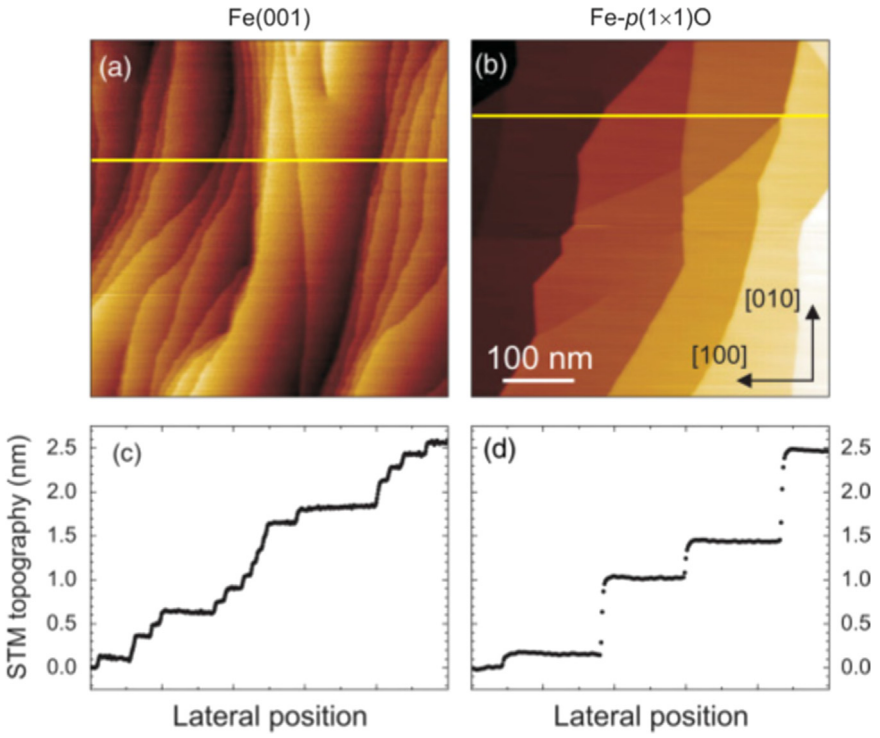

Fig. 11. (a and b) Comparison between the mesoscopic morphology of Fe(001) and Fe(001)-$p(1 \times 1)$O (image size is 500×500 nm^2). (c and d) Profiles measured along the scan lines drawn in panels (a) and (b), respectively. Reprinted with permission from Ref. [223]. Copyright (2011) by the American Physical Society.

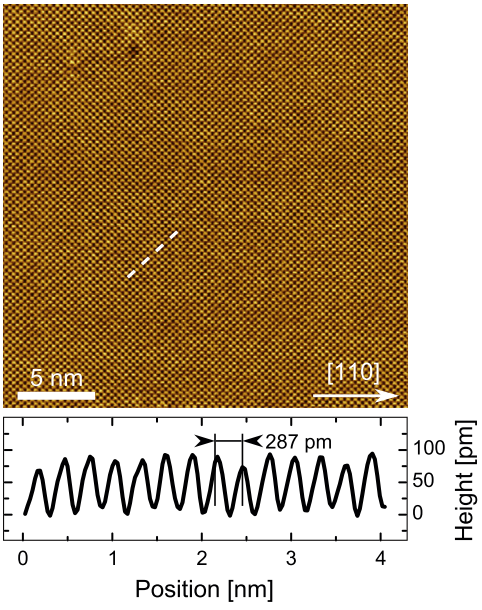

Fig. 12. Atomically resolved STM image illustrating the high degree of order at the Fe(001)-$p(1 \times 1)$O surface.

function of the oxidized sample is about 0.6–0.7 eV higher than that of the oxygen-free surface [230,231]. The oxygen overlayer also induces an outward relaxation of the topmost Fe layer, with the first Fe–Fe interlayer spacing increased with respect to the bulk value. First principles calculations performed by Chubb et al. show a 23% increase [232], while Legg et al. inferred an expansion of 7% from LEED data [233]. More recently, Parhiar et al. determined an increase of 16% by combining x-ray diffraction and *ab initio* calculations [234]. The oxygen-induced relaxation of the topmost layers has been found to enhance the surface spin-dependent effects with respect to oxygen-free Fe(001) [235]. Moreover, the surface magnetic moment oscillates during Fe homoepitaxial growth on the Fe(001)-$p(1 \times 1)$O [236,237], a phenomenon recently related to the different oxygen adsorption geometry on the islands and on the atomically flat terraces [238].

The first layer of oxygen atoms adsorbed on the Fe(001) hollow sites is often described as a chemisorbed phase, preceding the onset of bulk oxidation. However, the atomic structure of the Fe(001)-$p(1 \times 1)$O surface has been suggested to be similar to an ultra-thin rocksalt-type FeO film accommodated on the Fe(001) surface, as evidenced by the theoretical investigation of Blonski et al., where the presence of strong covalent Fe–O bonds formed by Fe-3*d*-O-2*p* hybrid orbitals, similar to those of bulk FeO, was highlighted [231]. These theoretical results are experimentally confirmed by low electron-kinetic-energy AES spectroscopy [see Fig. 13(a)], which is particularly sensitive to the local chemical environment of surface atoms. While the spectrum of the oxygen-free surface is characterized by a single peak located at about 47 eV, corresponding to the MVV transition of clean Fe(001), upon oxygen adsorption a small shoulder appears at about 38 eV. This feature is more evident in the spectra acquired by tilting the sample with respect to the emitted electron beam, indicating that such a feature is related to the surface electronic structure. The same feature is found also on Fe oxide surfaces produced by oxidation of either bulk Fe samples [239–241] or W(110)-supported Fe monolayer films exposed to oxygen

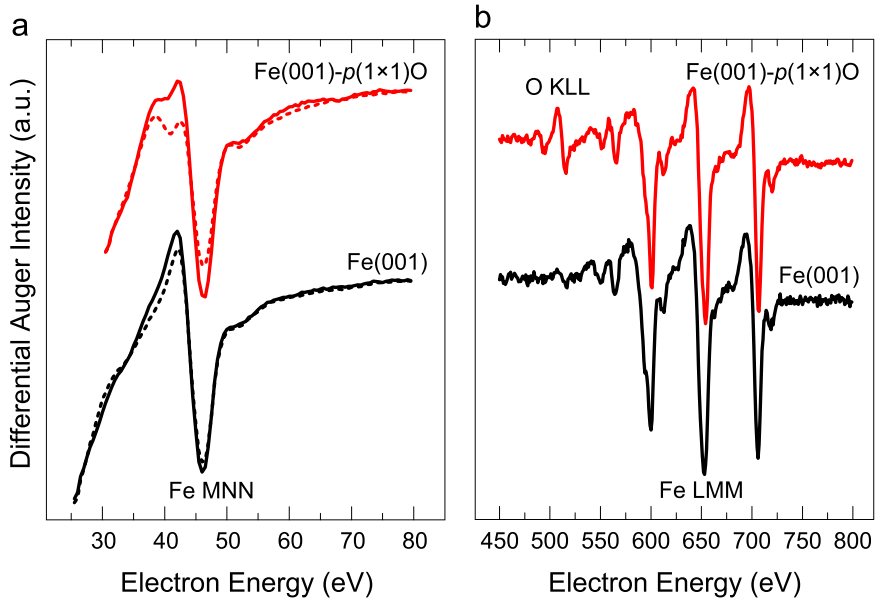

Fig. 13. Comparison between AES spectra acquired on the clean Fe(001) surface and on the oxygen passivated Fe(001)-$p(1 \times 1)$O surface. (a) Low kinetic energy region. In the spectrum corresponding to the Fe(001)-$p(1 \times 1)$O surface, a small shoulder is present at lower kinetic energies with respect to the main metallic peak, visible at 47 eV. Dashed spectra have been acquired with the sample normal tilted with respect to the incident beam current by an angle of 77°. (b) High kinetic energy region. Upon oxygen adsorption, the peaks corresponding to oxygen KLL transitions arise.

[242], indicating that the chemical bonds between Fe and O on the Fe(001)-$p(1 \times 1)$O surface are very similar to those found on the surfaces of Fe oxides. Fig. 13(b) displays the spectra acquired on the Fe(001) and Fe(001)-$p(1 \times 1)$O samples in the high kinetic energy region. Upon oxygen adsorption, the peaks related to the O KLL transitions arise, while the Fe LMM transitions are not significantly perturbed by the oxygen overlayer.

STS acquired on the Fe(001)-$p(1 \times 1)$O surface confirms that substantial modifications of the Fe(001) electronic structure are induced by the ordered oxygen overlayer. The clean Fe(001) surface is characterized by an intense surface state at 0.17 eV above E_F [243], weakly shifted by 0.04 eV to higher energies when isolated oxygen impurities are present on the surface [244]. On the other hand, in dI/dV STS data acquired on the Fe(001)-$p(1 \times 1)$O surface, displayed in the inset of Fig. 14, two peaks are located at about 1 eV above and 0.5 eV below E_F, respectively [226]. These spectroscopic features are better resolved in the spectrum reported in the main panel of Fig. 14, obtained by normalizing the STS curves to the tunneling barrier transmission coefficient [226,245,246].

A direct comparison between the measured and the computed electronic structure for the Fe(001)-$p(1 \times 1)$O surface is obtained by considering the calculated density of states integrated over a proper region of the first surface Brillouin zone [226]. Fig. 15 displays the computed density of states, evaluated in the two surface layers (Fe and O). The majority and minority components are reported in the upper and lower panels, respectively, while the dotted line corresponds to the total DOS. The minority-spin state located at 0.17 eV, characteristic of oxygen-free Fe(001) [243], is not present on the Fe(001)-$p(1 \times 1)$O surface, while a feature at 0.8 eV is detected. This is attributed to a surface resonance, because of its large amplitude in the vacuum region. This unoccupied minority surface state is in very good agreement with the measured position of the large peak at positive bias in STS data. A better agreement between experiment and theory can be obtained by considering that, because of the faster decay towards vacuum of the wave functions at large k values, the STS probing method possesses a higher sensitivity to states around the Γ point. By assuming that only 1/5 of the first surface Brillouin zone around Γ contributes to the STS signal [Fig. 15(b)], one finds that features at about 0.35 eV below E_F appear in the partial density of minority spin states, which can be readily associated to the peak detected at about -0.5 eV in the STS spectra.

In conclusion, the available experimental and theoretical data suggest to consider the Fe(001)-$p(1 \times 1)$O as a completely new phase with respect to oxygen-free Fe(001), characterized by its own structural, electronic and magnetic properties.

4.2. *Wetting layer oxides on Fe(001)*

A suitable strategy to obtain a sharp interface between a single-layer of oxide and a reactive substrate could be to exploit the oxygen adsorbed on the surface before metal deposition since, in this case, the amount of oxygen available is well defined. Preloaded oxygen on surface and subsurface sites has been employed for the preparation of two-dimensional films of vanadium, niobium, and molybdenum oxides on $Cu_3Au(100)$ [247]. An incomplete BaO_x layer was obtained by depositing Ba atoms on the O (2×1) Ni(110) surface [248]. More recently, a sharp interface between a Ni thin film and a single layer of NiO was obtained by depositing Ni onto a pre-oxidized Cu(100) surface [249], and even a ternary $Ba_xTi_2O_3$ oxide has been obtained by depositing Ba

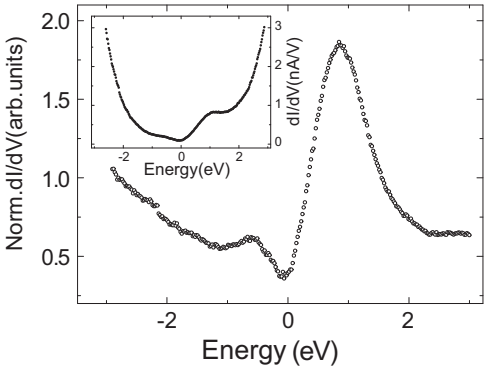

Fig. 14. Conductance spectra, normalized to the tunneling barrier transmission coefficient, acquired on the Fe(001)-$p(1 \times 1)$O surface. The inset displays the raw data. Reprinted with permission from Ref. [226]. Copyright (2009) by the American Physical Society.

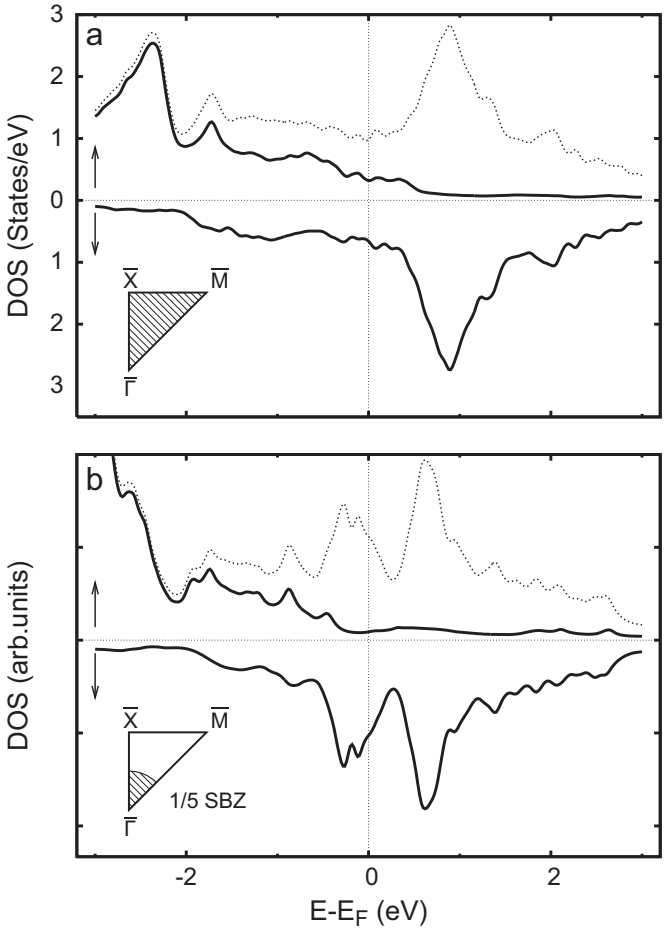

Fig. 15. (a) Computed density of Fe(001)-$p(1 \times 1)$O states in the surface region (surface and subsurface layer), integrated over the entire first surface Brillouin zone. (b) Computed density of Fe(001)-$p(1 \times 1)$O states integrated only over 1/5 of the surface Brillouin zone around Γ. Up arrow: majority-spin component; down arrow: minority-spin component; dotted line: total density of states. Reprinted with permission from Ref. [226]. Copyright (2009) by the American Physical Society.

atoms onto an ultra-thin Ti_2O_3 film supported on Au(111) [250]. The natural starting point for the growth of Fe(001) supported ultra-thin oxides is the Fe(001)-$p(1 \times 1)$O surface. A

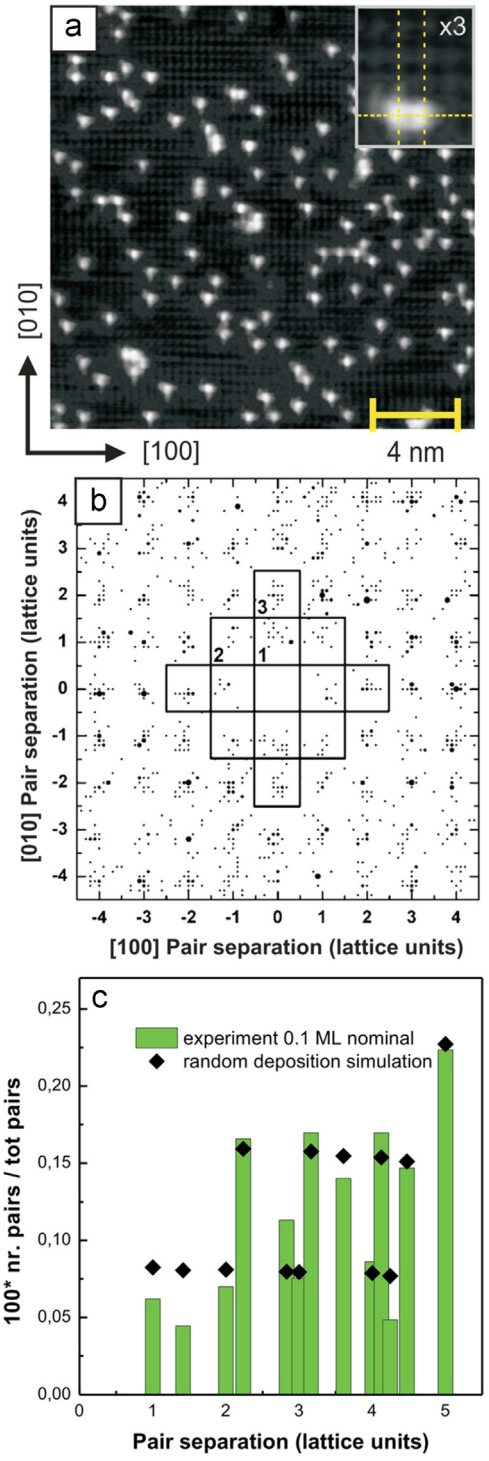

Fig. 16. (a) Atomically resolved STM image acquired after deposition of 0.1 ML Cr on the Fe(001)-$p(1 \times 1)$O substrate kept at high temperature (673 K). The inset shows a blow-up of a Cr first nearest-neighbor pair, where the alignment with the substrate lattice is indicated by the dashed lines. (b) Statistical distribution of relative Cr pair co-ordinates of the adatoms observed in panel (a). Regions corresponding to the first, second, and third nearest-neighbor separations are evidenced in the figure. (c) Comparison between the experimental results reported in panel (b), integrated over the possible directions (vertical bars), and a simulated random distribution (symbols). Reprinted with permission from Ref. [252]. Copyright (2013) by AIP Publishing LLC.

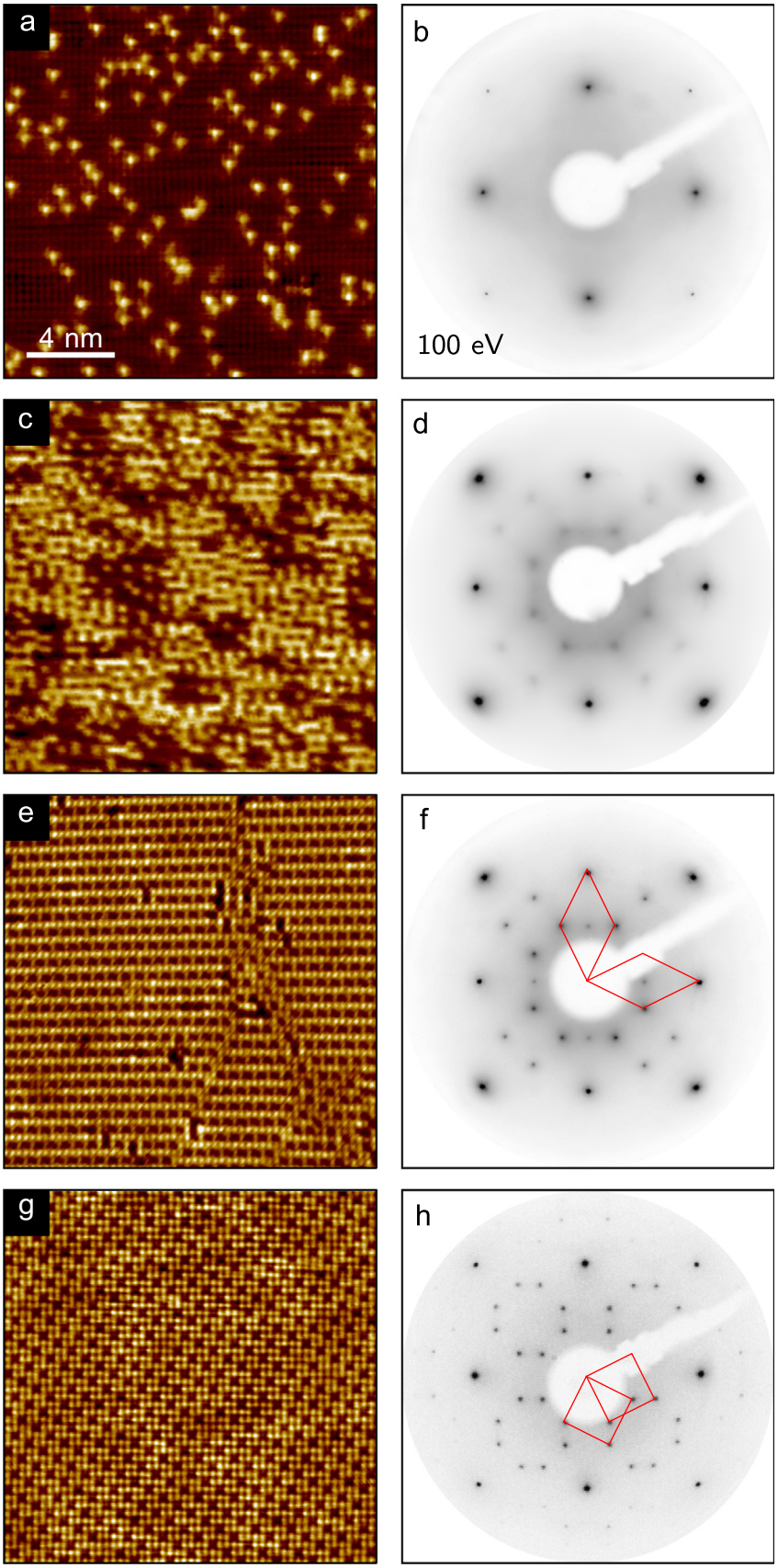

Fig. 17. High-resolution STM images acquired after deposition of (a) 0.1, (c) 0.4, (e) 0.75, and (g) 0.8 ML of Cr on Fe(001)-$p(1 \times 1)$O, respectively ($I = 5$ nA, $V = 100$ mV). In the right column the corresponding LEED patterns (electron beam energy $E = 100$ eV) are reported. The reciprocal unit cells of the two rotational domains are superimposed on panels (f) and (h). Adapted with permission from Ref. [251]. Copyright (2013) by the American Physical Society.

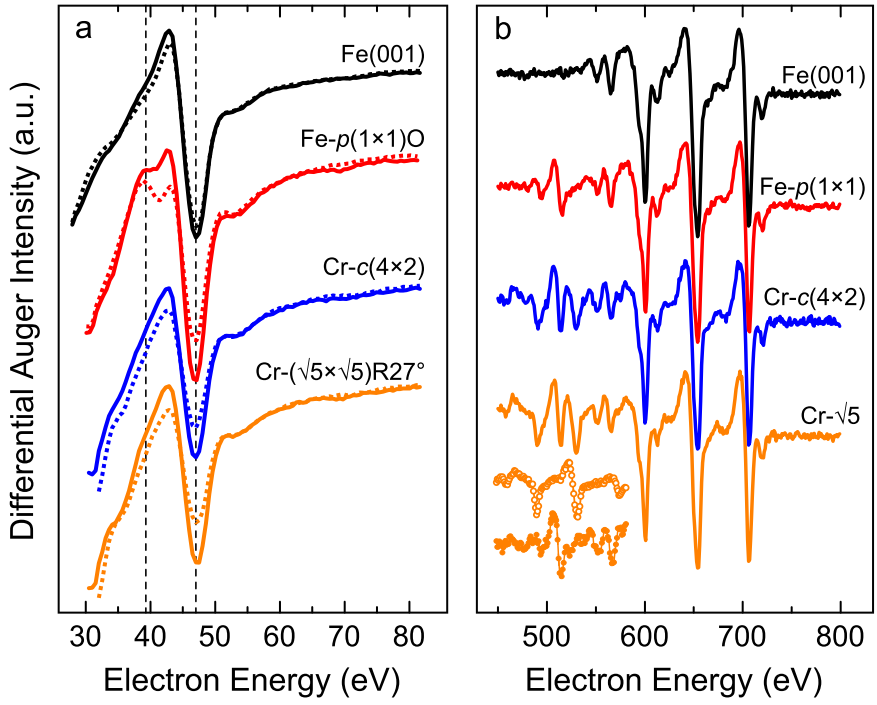

Fig. 18. (a) Variation of the Fe MNN AES lineshape at normal (continuous line) and grazing incidence (dotted line, sample normal 77° tilted with respect to the emitted beam) for the different Cr_xO_y phases observed for ultra-thin Cr/Fe(001)-$p(1 \times 1)$O films. The vertical dashed lines indicate the maximum of the feature related to Fe-O bonds (39.5 eV) and the minimum of the metallic Fe peak (47 eV). (b) Corresponding high kinetic energy region for the same samples in (a). The bottom-left part reports the spectrum of a reference Cr sample (open symbols) and the result (full symbols) obtained by subtracting the former from the AES spectrum observed on the $(\sqrt{5} \times \sqrt{5})R27^\circ$ sample. Panel (a) adapted from Ref. [251]. Copyright (2013) by the American Physical Society.

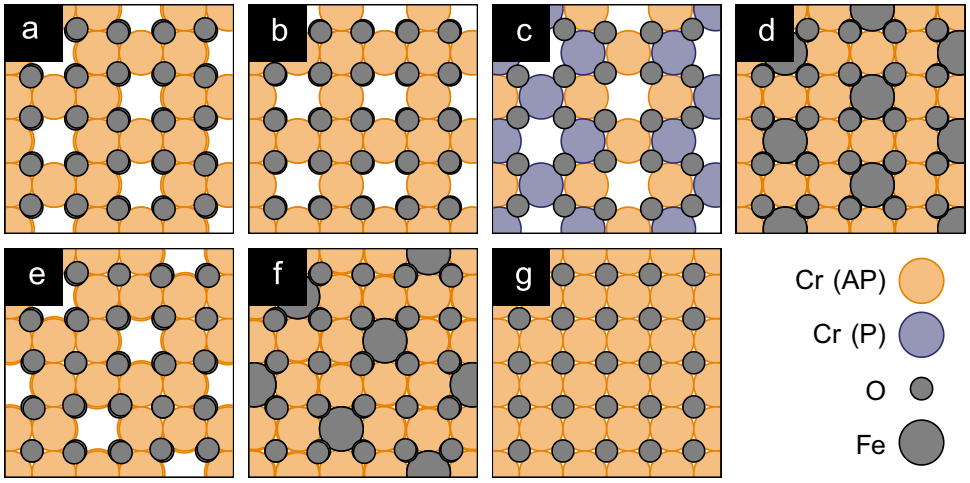

Fig. 19. Top view of structures simulated by DFT: (a) $c(4 \times 2)$ phase with metal vacancies, (b) $p(2 \times 2)$, (c) $p(4 \times 2)$, (d) $c(4 \times 2)$ with Fe atoms filling the vacancies, (e) $(\sqrt{5} \times \sqrt{5})R27^\circ$ with metal vacancies, (f) $(\sqrt{5} \times \sqrt{5})R27^\circ$ with Fe atoms filling the vacancies, and (g) $p(1 \times 1)$. Only atoms above the Fe(001) surface layer are depicted. Cr (AP)/(P) refers to atoms with magnetic moment antiparallel/parallel to the one of the Fe surfaces. Reprinted with permission from Ref. [251]. Copyright (2013) by the American Physical Society.

noteworthy case in which this strategy has been successful is that of Cr oxide single layers [251,252].

Fig. 16(a) focuses on the surface morphology of 0.1 ML Cr grown on the Fe(001)-$p(1 \times 1)$O surface, with the substrate kept at 673 K during Cr deposition. Isolated atomic-scale features, imaged as protrusions in the constant current STM image, are visible on the substrate. The observation of isolated atoms in STM measurements acquired at room temperature, where adatoms are usually highly mobile on uniform surfaces, suggests that deposited Cr atoms are embedded into the topmost substrate layer. Fig. 16(b) and (c) displays the outcome of a statistical analysis performed on the atomically resolved STM images, from which it is possible to notice that the Cr pair distribution does not significantly deviate from a random distribution. In a similar analysis performed for Cr deposition on oxygen-free Fe(001) [253], no nearest neighbor Cr adatoms were found, indicating an effective repulsion between Cr atoms, which has been attributed to the presence

Table 5
Summary of DFT energetics. The unit cell of each structure covers $N_{1\times1}$ primitive unit cells of Fe(001) and includes N_{Cr} (N_{Fe}) Cr (Fe) atoms. F indicates the formation energy per Cr atom. Refer to Fig. 19 for structural models. Reprinted with permission from Ref. [251]. Copyright (2013) by the American Physical Society.

Coverage	Structure	Periodicity	$N_{1\times1}$	N_{Cr}	N_{Fe}	F (eV)
0.75 ML	(a)	$c(4\times2)$	4	3	0	−1.12
	(b)	$p(2\times2)$	4	3	0	−1.05
	(c)[a]	$p(4\times2)$	8	6	0	−0.99
	(d)[b]	$c(4\times2)$	4	3	1	−0.70
0.80 ML	(e)	$(\sqrt{5}\times\sqrt{5})R27^\circ$	5	4	0	−1.02
	(f)[b]	$(\sqrt{5}\times\sqrt{5})R27^\circ$	5	4	1	−0.69
1.00 ML	(g)	$p(1\times1)$	1	1	0	−0.55

[a]Antiferromagnetic coupling within the Cr layer.
[b]Vacancies filled by Fe atoms.

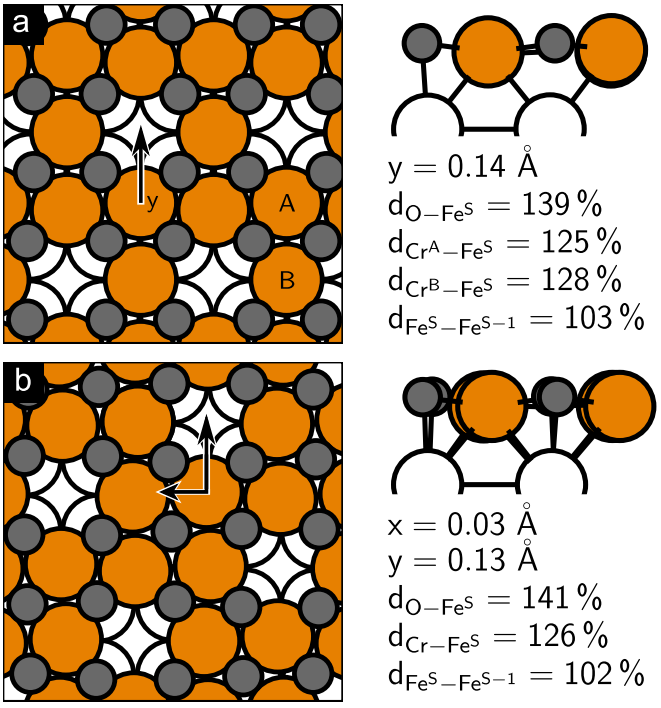

Fig. 20. Top and side views of the (a) $c(4\times2)$ and (b) $(\sqrt{5}\times\sqrt{5})R27^\circ$ superstructures. The arrows indicate the in-plane displacements (x,y) of the Cr atoms. Interlayer spacings d are given in percentages of the one in bulk iron. By Fe^S and Fe^{S-1} we indicate iron atoms in the first and the second layer, respectively. Reprinted with permission from Ref. [251]. Copyright (2013) by the American Physical Society.

of magnetic frustration [254]. This repulsive interaction between Cr atoms embedded in the Fe(001) topmost layer seems to be suppressed by the oxygen overlayer present on the Fe(001)-$p(1\times1)$O substrate.

For higher coverages the Cr atoms self-organize in highly ordered structures, as evidenced in Fig. 17. In Fig. 17(c), corresponding to a Cr coverage of 0.4 ML, the regions in which the Cr density is higher, appear to be locally ordered, as

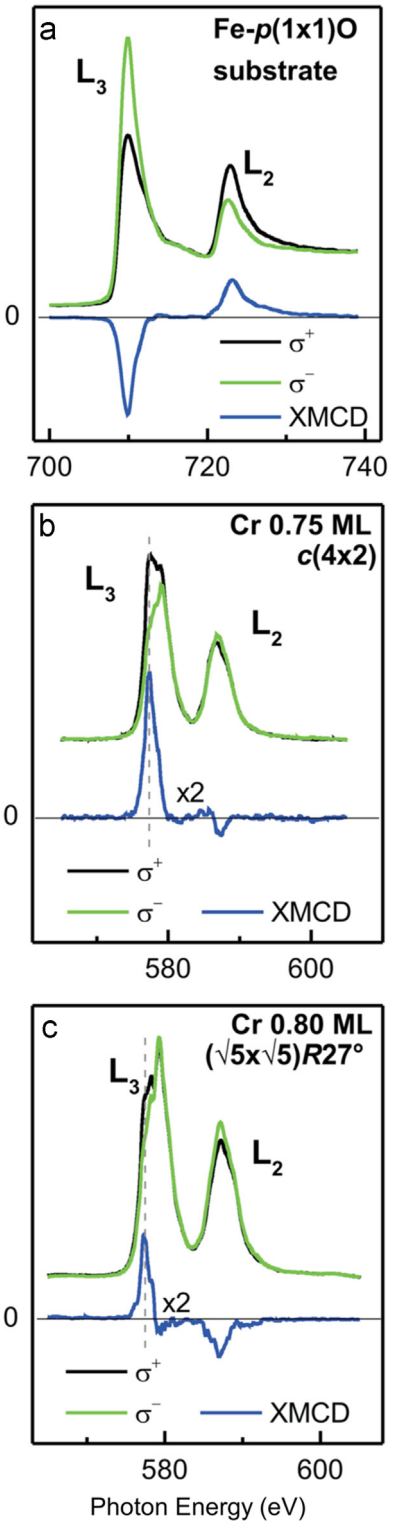

Fig. 21. XAS spectra at $L_{2,3}$ edges taken with either positive (black lines) or negative (green lines) photon helicity and XMCD spectra (blue lines) of panel (a) Fe(001)-$p(1\times1)$O substrate; panel (b) $c(4\times2)$ phase; and panel (c) $(\sqrt{5}\times\sqrt{5})R27^\circ$ phase. The dashed vertical lines indicate the position of the XMCD main peak. Adapted with permission from Ref. [252]. Copyright (2013) by AIP Publishing LLC. (For interpretation of the references to color in this figure caption, the reader is referred to the web version of this paper.)

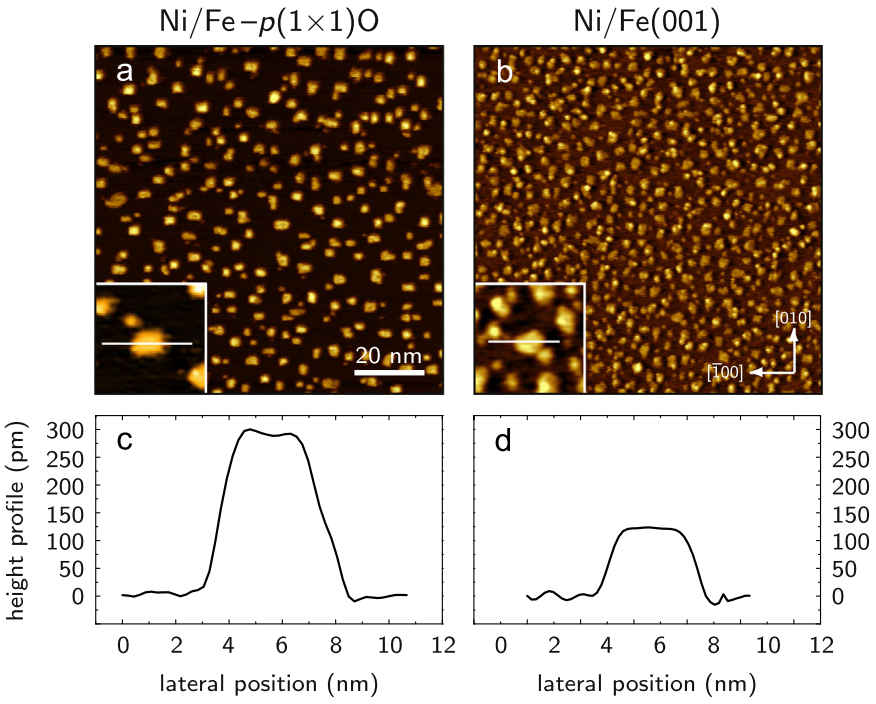

Fig. 22. STM topography after deposition of 0.35 ML of Ni on (a) Fe(001)-$p(1 \times 1)$O and (b) Fe(001). (c and d) STM profiles measured along the lines traced in panels (a) and (b), respectively. Reprinted with permission from Ref. [257]. Copyright (2012) by the American Physical Society.

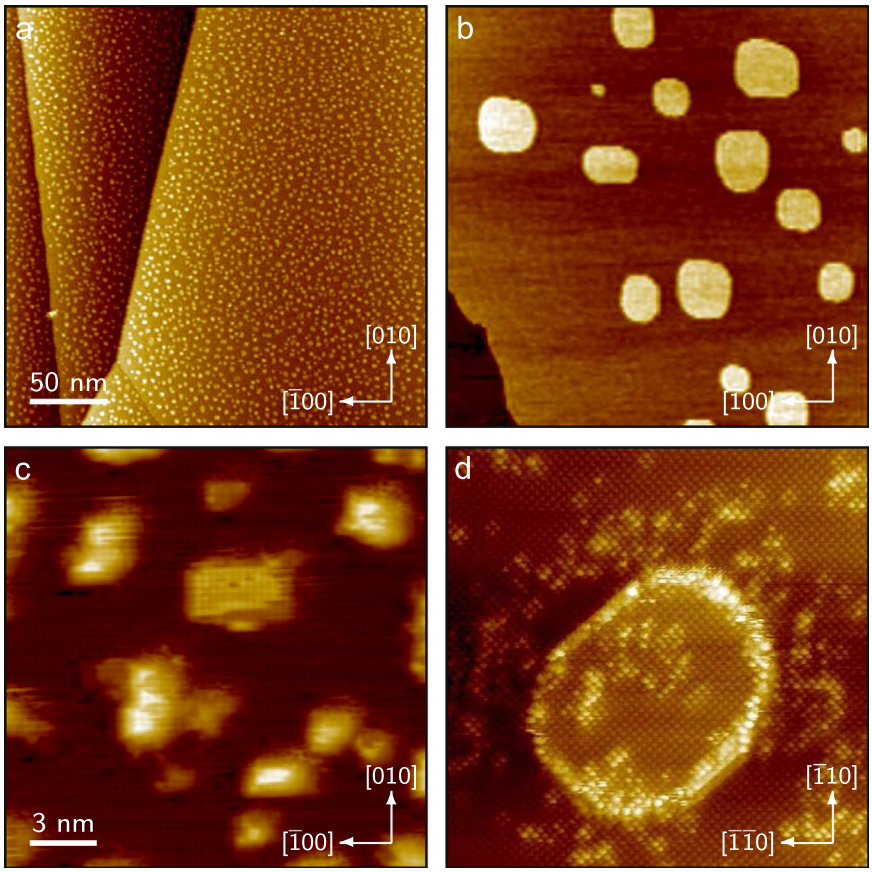

Fig. 23. STM images of 0.6 ML Ni grown on Fe(001)-$p(1 \times 1)$O. (a and c) Morphology of the as-grown sample. (b and d) Morphology after post-annealing treatment at 600 K. The islands size after the annealing increases by one order of magnitude with respect to the case before annealing. (d) Enlarged view of an island: the small bright features on the substrate and on the islands, with apparent height of 40 pm, indicate intermixing between Ni and Fe. Panels (a) and (b): 270×270 nm^2; panels (c) and (d): 19×19 nm^2. Reprinted with permission from Ref. [257]. Copyright (2012) by the American Physical Society.

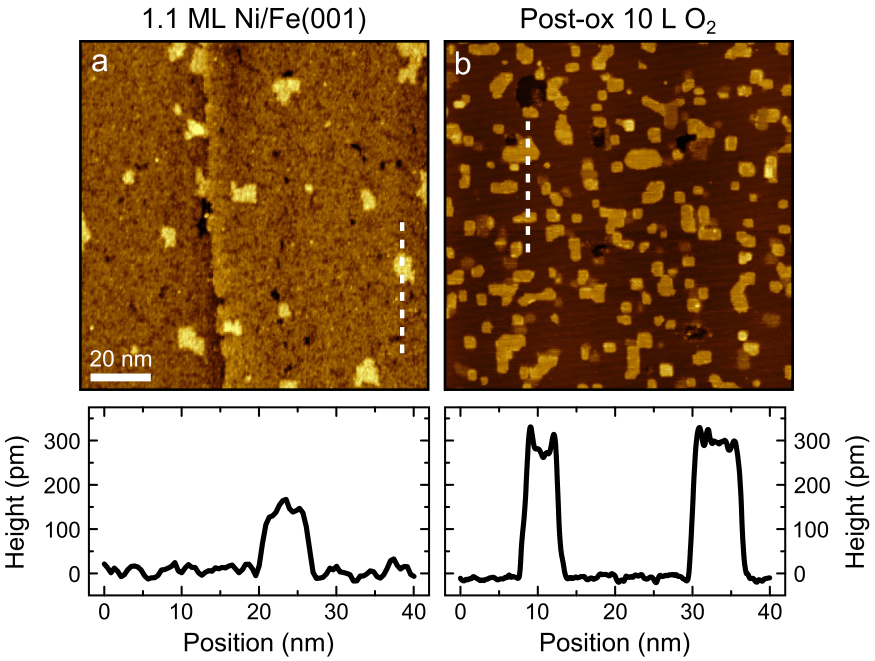

Fig. 24. Effects of the post-oxidation process (10 L of O_2 at RT and post-annealed to 470 K for 5 min) performed on a 1.1 ML-thick Ni film grown at 370 K on the oxygen-free Fe(001). Panels (a) and (b) display the surface topography before and after the post-oxidation treatment, respectively. Line profiles along the corresponding dashed white lines are reported at the bottom of each panel. Panel (a) $V=100$ mV, $I=100$ pA; panel (b) $V=1$ V, $I=300$ pA.

also testified by the faint $c(4 \times 2)$ superstructure visible in the LEED pattern of Fig. 17(d). At a coverage of 0.75 ML, the substrate is completely covered by an atomically flat wetting layer characterized by a $c(4 \times 2)$ periodicity, arising from an ordered array of dark holes with a rhombic primitive cell, well-visible in the STM image and LEED pattern reported in Fig. 17(e) and (f), respectively [251]. Increasing the coverage up to 0.8 ML leads to a large-scale reorganization of the overlayer, resulting in a transition toward a $(\sqrt{5} \times \sqrt{5})R27^{\circ}$ phase, displayed in the real and reciprocal space in Fig. 17(g) and (h), respectively.

Further insights into the Cr/Fe(001)-$p(1 \times 1)$O surface and interface chemistry can be acquired from AES spectroscopy. Fig. 18(a) and (b) shows low and high kinetic energy AES spectra, respectively. The spectrum measured on Fe(001)-$p(1 \times 1)$O differs from that of oxygen-free Fe(001) by the presence of a shoulder located at lower kinetic energy with respect to the metallic peak located at 47 eV, readily associated to the presence Fe–O bonds (see Section 4.1). After Cr deposition, the shoulder disappears, indicating that the Fe–O bonds are broken. However, the peak related to O KLL transitions is still visible in the high kinetic energy region, revealing that oxygen atoms are still present on the surface layer. By combining these pieces of informations it is possible to deduce that the Fe–O bonds are replaced by Cr–O bonds [251].

Further insight concerning the wetting-layer Cr oxides come from theoretical analysis, based on DFT simulations performed with the generalized gradient approximation for the exchange and correlation functional as proposed by Perdew, Burke, and Ernzerhof (GGA-PBE) [255]. Fig. 19 presents some structural models based on the O–Cr–Fe(001) stacking suggested by AES spectra. Cr atoms are located in the hollow sites of the Fe(001) surface, originally occupied by oxygen atoms. The latter are placed on Fe-atop sites, between Cr atoms and slightly above them. The corresponding formation energies per Cr atom are reported in Table 5.

For a 0.75 ML-Cr coverage, the most stable arrangement is found to be the $c(4 \times 2)$ structure, with the topmost layer composed by 75% of Cr atoms and 25% by vacancies [see Fig. 19(a)]. This is in good agreement with the observation of the $c(4 \times 2)$ superstructure in the early nucleation stages. Arranging the same amount of Cr atoms in a $p(2 \times 2)$ overlayer results in a less stable structure by 0.07 eV per Cr atom. The observed STM images and LEED patterns, displaying the $c(4 \times 2)$ superstructure, could be compatible also with the models of Fig. 19(c) and (d). In the first case, the Cr magnetic moments are supposed to be alternately parallel/antiparallel to that of Fe, resulting in a $p(2 \times 4)$ superstructure, where the net magnetization of the Cr oxide overlayer is zero. However, the strong magnetic coupling with the Fe substrate makes this magnetic configuration less convenient (by 0.13 eV per Cr atom) with respect to the one where all the Cr spins antiparallel to the Fe magnetization. In the second case, the dark holes forming the $c(4 \times 2)$ superstructure are supposed to be filled with Fe atoms. However, in this case the formation energy is highly unfavorable, with an estimated energy cost per Fe atom equal to 1.27 eV.

The $c(4 \times 2)$ phase is characterized by two inequivalent Cr atoms, denoted by Cr_A and Cr_B in Fig. 20(a), possessing three and two nearest Cr neighbors, respectively. The lower number of Cr neighbors makes the Cr_B atoms less affected by magnetic frustration, resulting in a higher magnetic moment for Cr_B (3.1 μ_B) with respect to that of Cr_A (2.9 μ_B). Lowdin population analysis reveals that Cr_A and Cr_B differ also by their net

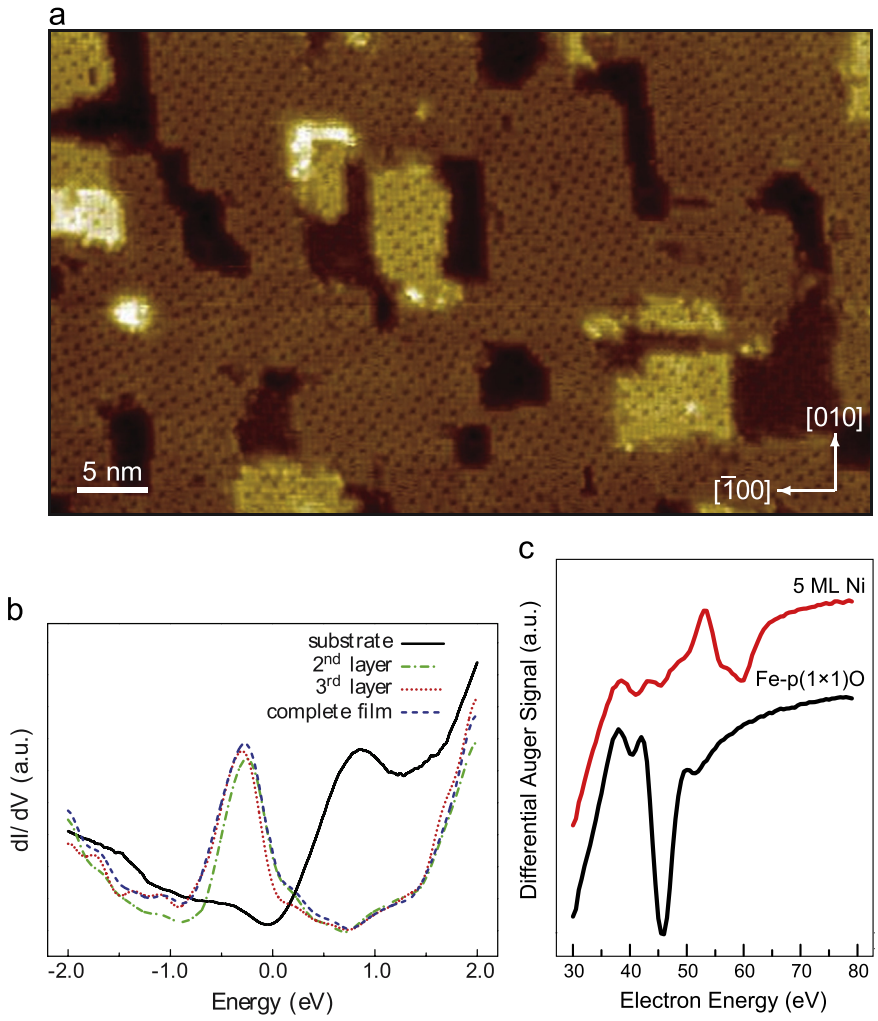

Fig. 25. (a) STM topography of a 5 ML-thick Ni film deposited on the Fe(001)-$p(1 \times 1)$O substrate. (b) STS spectra acquired on the Fe(001)-$p(1 \times 1)$O surface and on the Ni film at different Ni thickness. A strong peak is present at about 0.25 eV below E_F. (c) AES spectra acquired on Fe(001)-$p(1 \times 1)$O and 5 ML Ni/Fe(001)-$p(1 \times 1)$O. Notice the presence of the shoulder at about 38 eV, characteristic of oxidized Fe atoms. Panels (a) and (b) reprinted with permission from Ref. [257]. Copyright (2012) by the American Physical Society.

charge, which are $+1.12\,e$ and $+1.16\,e$, respectively. Electrons displaced from Cr atoms mainly move towards the oxygen atoms, which are negatively charged ($-0.62\,e$ each). A small fraction of charge also flows towards the first Fe layer ($-0.08\,e$ per Fe atom). The charge flow towards the metallic substrate induces a rumpling of the oxide film, with the oxygen sublayer at larger distances from the support than the cation one [256].

At a coverage of 0.80 ML the energetically most stable structure is $(\sqrt{5} \times \sqrt{5})R27^\circ$, with a formation energy of -1.02 eV per atom. The experimentally observed abrupt phase transition from $c(4 \times 2)$ to $(\sqrt{5} \times \sqrt{5})R27^\circ$ can be understood by comparing the formation energy of the $(\sqrt{5} \times \sqrt{5})R27^\circ$ phase with that of a mixed phase, obtained by filling 20% of the $c(4 \times 2)$ vacancy sites with Cr atoms to obtain 0.80 ML coverage. In this case 25% of the Cr atoms would form $p(1 \times 1)$ patches within the $c(4 \times 2)$ phase, yielding $F_{mix} = 0.75F(a) + 0.25F(g) = -0.98$ eV. In the $(\sqrt{5} \times \sqrt{5})R27^\circ$, all Cr atoms are equivalent, with a Lowdin charge equal to $+1.12e$ and a magnetic moment of $3.0\,\mu_B$. Similarly to the $c(4 \times 2)$ case, the occupation of vacancy sites by Fe atoms would increase significantly the formation energy by 1.34 eV per added Fe atom.

The analysis of XMCD profiles extracted from experimental XAS spectra provides information about the magnetization of the different Cr oxide phases stabilized on the Fe(001) surface [252]. Fig. 21 reports XAS spectra acquired on the Cr_xO_y layers at coverages of 0.75 ML [$c(4 \times 2)$ phase], and 0.8 ML [$(\sqrt{5} \times \sqrt{5})R27^\circ$ phase] [252]. In both spectra the overlayer dichroic signal is opposite to that of the iron substrate, confirming the theoretic predictions of Cr oxide wetting layers possessing a ferromagnetic order, antiferromagnetically coupled to the Fe(001) substrate.

Unlike the Cr_xO_y/Fe(001) case, it is not possible to stabilize a wetting NiO layer on the Fe(001) surface by depositing Ni on the Fe(001)-$p(1 \times 1)$O substrate. Fig. 22 compares the morphology resulting from Ni deposition on the Fe(001)-$p(1 \times 1)$O [panel (a)] and Fe(001) [panel (b)] surfaces, with the substrates held at 400 K

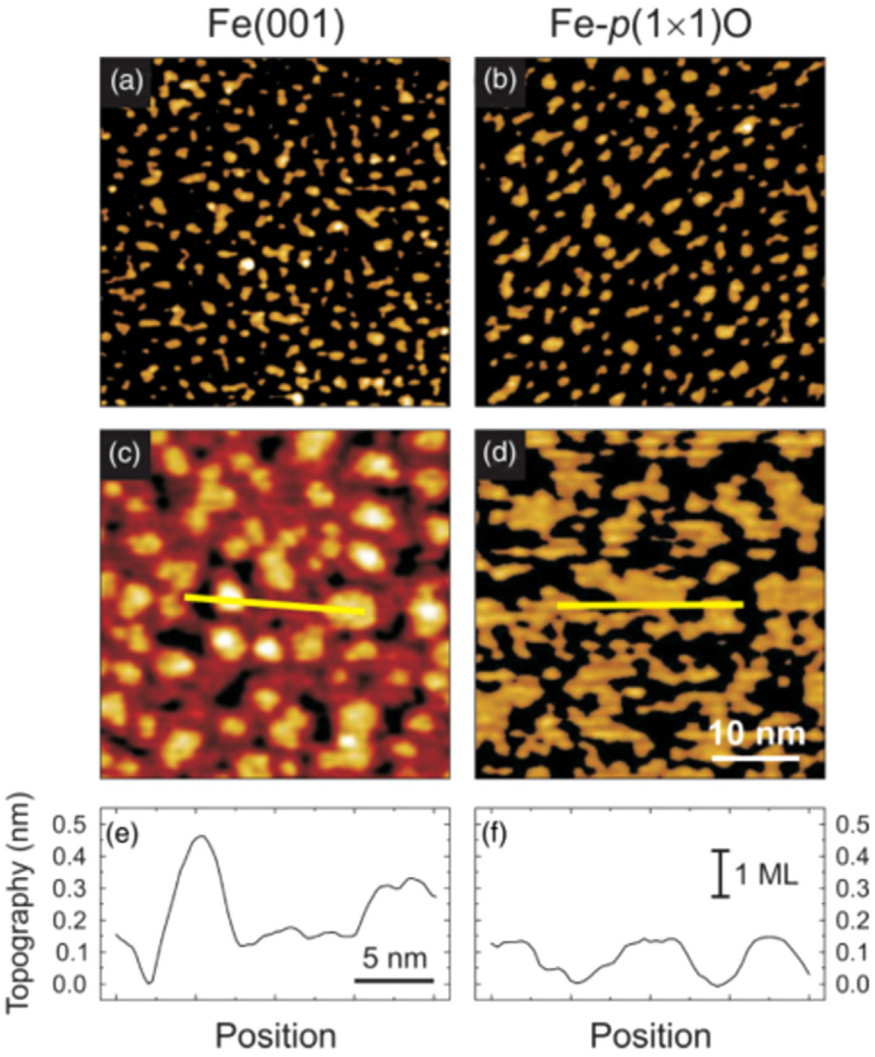

Fig. 26. STM topography after deposition of 0.25 ML of iron on (a) Fe(001) and (b) Fe(001)-$p(1 \times 1)$O. STM topography after deposition of 3.5 ML of iron on (c) Fe(001) and (d) Fe(001)-$p(1 \times 1)$O. (e, f) STM profiles measured along the lines traced in panels (c) and (d), respectively. The image size in panels (a)–(d) is 40×40 nm^2. Reprinted with permission from Ref. [223]. Copyright (2011) by the American Physical Society.

during Ni deposition [257]. The STM topographic heights acquired across a Ni island nucleated on the Fe(001)-$p(1 \times 1)$O and on the Fe(001) substrates are displayed in Fig. 22(c) and (d), respectively. While Ni deposited on clean Fe(001) surface nucleates single-layer islands (with a topographic height of about 140 pm), only bi-layer islands (with a topographic height of about 280 pm) are present when Ni is deposited on the Fe(001)-$p(1 \times 1)$O substrate, suggesting that a single layer of NiO accommodated on top of Fe(001) is not stable.

Ni deposition at higher temperature or post annealing treatments up to 550 K do not induce a flattening of the bi-layer Ni islands [257]. Instead, post annealing treatments at higher temperatures induce a drastic modifications on the surface morphology. Fig. 23 displays the effect of post annealing at 600 K, performed on a 0.6 ML Ni film deposited on the Fe(001)-$p(1 \times 1)$O surface. The morphology of the as-grown sample, displayed in Fig. 23(a) and (c), is remarkably different compared to that obtained after heating, displayed in Fig. 23(b) and (d). The heating induces the development of larger islands, characterized by an height of 140 pm, typical of single layer islands. However, a closer look at the surface reveals the presence of small atomic-scale features, characterized by an apparent height of 40 pm, distributed on both the substrate and the islands. This observation suggests that the islands are mainly composed by Fe, while the bright spots are alloyed Ni atoms.

The instability of the NiO/Fe(001) surface is confirmed by the experiment displayed in Fig. 24. In this case a single layer of Ni deposited on the oxygen-free Fe(001) is exposed to 10 L of molecular oxygen, and annealed at 470 K for few minutes. Fig. 24(a) shows the STM topography obtained after deposition of 1.1 ML of Ni on the Fe(001) substrate. Ni perfectly wets the Fe(001) surface, and few islands belonging to the second layer are visible. Fig. 24(b) displays the STM topography obtained after oxygen exposure and post annealing at 470 K. The wetting layer breaks in bi-layer islands covering approximately half of the surface, as in the case of Ni deposited directly onto the oxygen pre-covered surface.

Notice that the occurrence of bi-layer islands has been seldom reported in metal heteroepitaxy. When observed it was

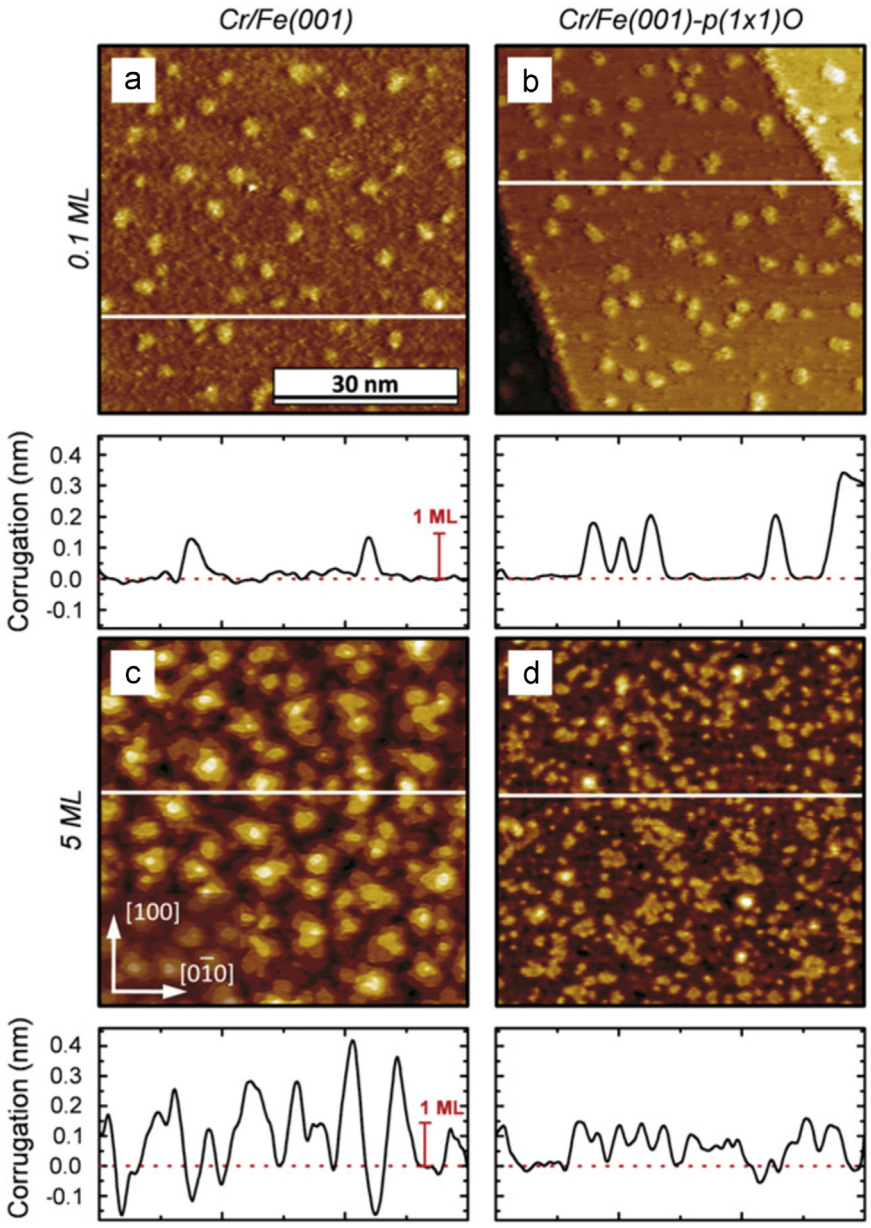

Fig. 27. Comparison of Cr nucleation on Fe(001) [panels (a) and (c)] and on Fe(001)-$p(1 \times 1)$O [panels (c) and (d)]. The substrate temperature during Cr deposition is 380 K. The Cr coverage is 0.1 ML in panels (a) and (b) and 5 ML in panels (c) and (d). Reprinted with permission from Ref. [278]. Copyright (2011) by Elsevier.

associated to the strain induced by the lattice mismatch. However, for Ni/Fe(001)-$p(1 \times 1)$O, strain does not seem to be the driving force for the nucleation of 2 ML-thick islands. The amount of oxygen present on the Fe(001)-$p(1 \times 1)$O surface is exactly what is needed to form a single layer of NiO. By allowing for a 45° rotation of the NiO fcc lattice with respect to the Fe bcc one, the misfit at the NiO(001)/Fe(001) interface is only 3%. Theoretical calculations predict for the single layer of NiO an even better matching with the Fe unit cell (Ni–Ni separation in NiO single layer is close to 2.8 Å) [258]. In this respect, the interface chemistry seems to play a fundamental role for the instability of a single layer of NiO on top of Fe(001).

Although the oxygen preloaded on the substrate does not allow for the stabilization of a single layer NiO, at higher coverages, when the Ni film completely covers the substrate, AES, STM, and STS data suggest that a single layer of a ternary oxide Ni_xFe_yO is formed at the surface. Fig. 25 displays the STM, STS and AES data acquired on a 5 ML-thick Ni film grown on Fe(001)-$p(1 \times 1)$O. AES spectra in the high kinetic energy region (not shown, see [257]) reveal that oxygen floats on top of the Ni film grown on the Fe(001)-$p(1 \times 1)$O substrate. Atomically resolved STM images, such as that displayed in Fig. 25(a), reveal the presence of a $(\sqrt{5} \times \sqrt{5})R27^\circ$ reconstruction, indicating that the overlayer is not formed by a single layer of NiO. In the low kinetic energy AES spectra of Fig. 25(c) the small shoulder characteristic of O-bound

Fe atoms is clearly visible (see Section 4.1), suggesting that the surface layer can be regarded as a Ni_xFe_yO single layer. This interpretation is also supported by the presence of a strong peak in STS spectra detected at about 0.25 eV below E_F, very similar to the resonance observed in spectra acquired on invar alloys [259].[1]

4.3. Growth of metallic buffer layers on Fe(001) and Fe(001)-p(1 × 1)O

From the discussion in the previous section, it is clear that exploiting the oxygen preloaded on the substrate prior to metal deposition could be a useful strategy to obtain a sharp interface between a metallic and an oxidic layer only if the goal is to obtain ultra-thin oxide films in the single-layer range. In order to control the chemical, structural and electronic interactions occurring at O/Fe interfaces for thicker films, a suitable strategy could consist in the insertion of a buffer layer. Here, in particular, we discuss the growth of metallic ultra-thin buffer layers on the Fe(001) surface. A suitable metallic buffer layer should possess specific characteristics, such as a good substrate wettability and a smooth surface (in other words, the growth should be layer-by-layer). The first requirement is mandatory since the presence of voids in the buffer layer would allow a direct contact between the oxidizing agent and the substrate, while the second is important since the surface roughness is likely to increase during the oxide deposition, preventing the stabilization of long-range-ordered epitaxial structures.

In this framework, understanding the atomistic mechanisms governing epitaxial growth is crucial to obtain a suitable metallic buffer layer. The thermodynamics description of epitaxy classifies the growth mode in terms of interface and surface free energies (see Section 2.2.2). However, such a description does not take into account the fact that the epitaxial growth is frequently performed in far-from-equilibrium conditions. Atoms impinging on the substrate diffuse over the surface, encountering energy barriers during their motion. The final film morphology is often determined by these kinetic constraints, especially if the substrate is kept at low temperatures (room temperature or below) during the growth of the film [260–263].

In this context, an important role is played by surfactant-assisted growth. A surfactant is a small amount of foreign atoms that, being adsorbed on the surface before film deposition, floats on top of the growing film and contributes to determining its morphology. Surfactants often switch the film growth mode from three-dimensional to two-dimensional. From the point of view of thermodynamics, surfactants change the surface and interface energy balance [264], while in the kinetic picture the surfactants action has been explained in terms of their influence on the diffusion rate of adatoms [265–267]. In this case, the growth mode is driven by the ratio between the intralayer and interlayer mass transport rates [265]. The former is related to the diffusion of atomic species over atomically flat terraces, while the latter expresses the rate at which atoms can overcome a step edge and reach either the lower or higher layer. Generally, the energy barrier at the step edge is higher than that on flat surfaces, since adatoms crossing the step edges are required to pass through low-coordination sites. If interlayer mass transport is much less efficient than intralayer mass transport, deposited atoms are likely to be trapped on top of already nucleated islands, favoring the nucleation of a new layer before lower one is completed. This typically leads to the development of a three-dimensional morphology. The presence of a surfactant overlayer can promote layer-by-layer growth by either decreasing the intralayer rate or increasing the interlayer mass transport.

This kinetic description is certainly the most appropriate one for surfactant-assisted homoepitaxial growth, since the substrate and the deposit possess the same surface free energy. In the case of Fe/Fe(001) homoepitaxy, it has been found that Fe films deposited on the oxygen-free Fe(001) substrate are characterized by a surface roughness which increases with coverage [268], while the growth on the oxygen-passivated surface is nearly layer-by-layer [269,270,223]. STM images displayed in Fig. 26(a) and (b) reveal that a sub-monolayer amount of Fe deposited on either Fe(001) or Fe(001)-$p(1 \times 1)$O features the same morphology. In both cases, single-layer islands nucleate, distributed over the surface with basically the same island density, $0.18\ nm^{-2}$ and $0.16\ nm^{-2}$ on Fe(001) and Fe(001)-$p(1 \times 1)$O, respectively [223]. Conversely, at higher coverages the surface morphology is quite different. For instance, for 3.5 ML of iron deposited on Fe(001) four layers are exposed [Fig. 26(c) and (e)], whereas, for the same coverage, iron films grown on Fe(001)-$p(1 \times 1)$O expose only two layers [Fig. 26(d) and (f)]. Oxygen floats on top of the growing Fe film and promotes the development of a smooth surface.

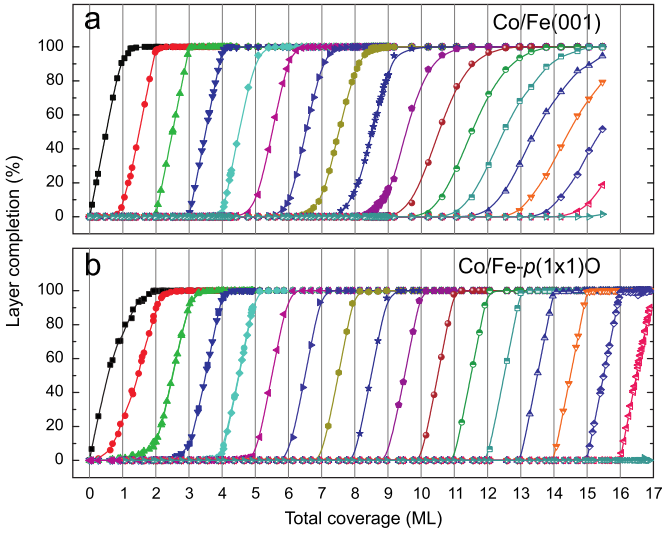

Fig. 28. Layer completion as a function of the total Co coverage on (a) oxygen-free Fe(001) and on (b) Fe(001)-$p(1 \times 1)$O. Reprinted with permission from Ref. [273]. Copyright (2015) by the American Physical Society.

[1] In ref. [257] the $(\sqrt{5} \times \sqrt{5})R27^\circ$ reconstruction observed on 5 ML Ni/Fe(001)-$p(1 \times 1)$O was tentatively related to the presence of Ni vacancies. However, the new AES data reported here suggest that the dark spots observed in STM images arise from a chemical contrast between Fe and Ni atoms.

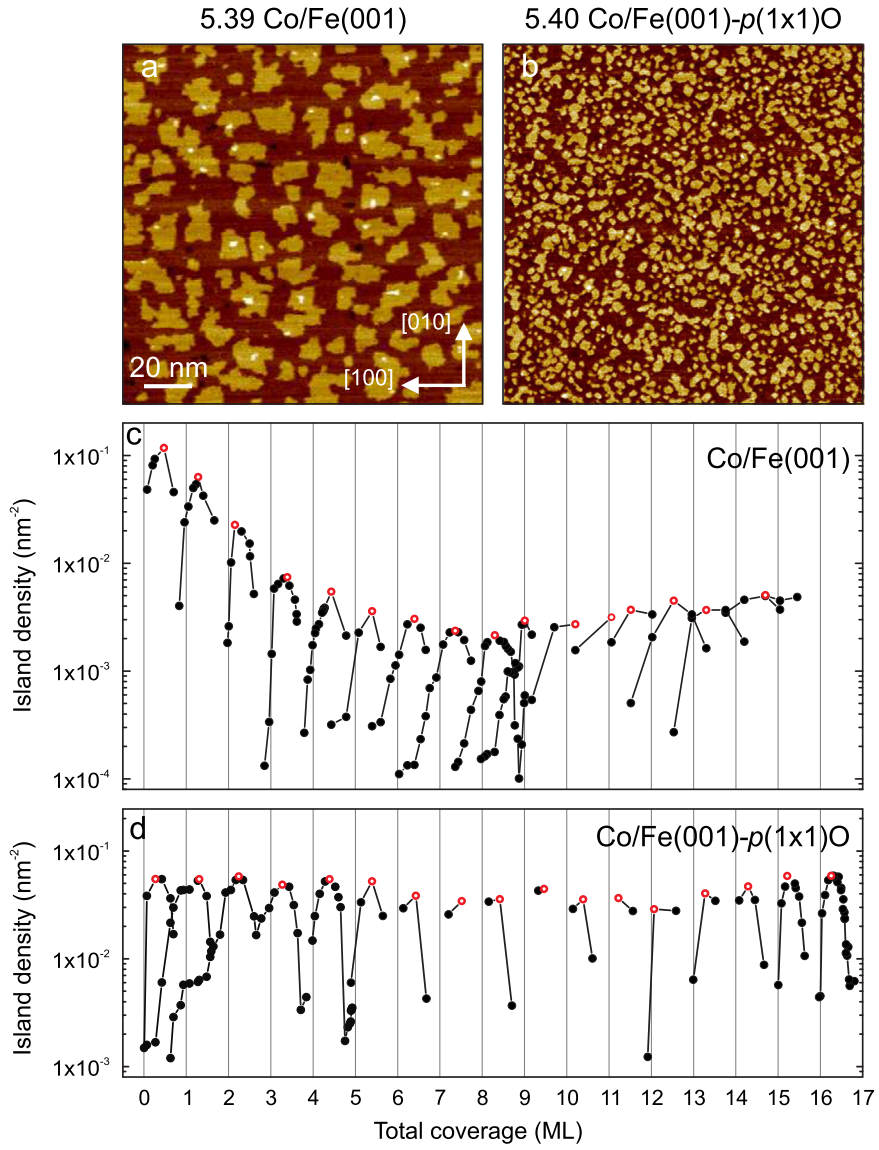

Fig. 29. (a) STM topographic image of a 5.4 ML-thick Co film grown on the oxygen-free Fe(001) surface. (b) STM topographic image of a 5.4 ML-thick Co film grown on the oxygen-passivated Fe(001)-$p(1 \times 1)$O surface. (c and d) Co island density as a function of the total coverage for Co films grown on (c) oxygen-free Fe(001) and on (d) Fe(001)-$p(1 \times 1)$O, respectively. The local maxima (hollow red dots) correspond to the saturation island density for a given layer. Reprinted with permission from Ref. [273]. Copyright (2015) by the American Physical Society. (For interpretation of the references to color in this figure caption, the reader is referred to the web version of this paper.)

In order to understand the surfactant action of oxygen we recall that, according to the classical nucleation theory [260], the island density is directly related to the atomic diffusion rate over the surface (intra-layer mass transport). Generally, the nucleation of large islands distributed with a low density over the surface indicates a high diffusion rate of atomic species, while the nucleation of a high density of small islands is observed in the case of low diffusion rates. Since the islands density is nearly the same for sub-monolayer deposition on both the oxygen-free and oxygen-passivated surface, the oxygen surfactant action in Fe homoepitaxy can be understood as a consequence of an oxygen-induced lowering of the energy barrier for *interlayer* mass transport [223]. Notice that the invariance of island density on the oxygen-free and oxygen-passivated surfaces represents a far-from-trivial observation, since the presence of surfactant atoms has been found to have a direct impact on the *intralayer* mass transport in a considerable number of cases, typically by enhancing the nucleation rate [271,272,265,273].

The oxygen surfactant action is found to be effective also for the growth of heteroepitaxial films, as demonstrated for instance in the case of oxygen-assisted growth of Mn on Fe [274], Fe, Co and Ni on Cu [275–277]. Fig. 27 shows an example of oxygen-assisted heteroepitaxial growth of Cr films deposited on the Fe(001) surface [278]. Similar to the case of Fe/Fe(001) homoepitaxy, the density of Cr islands nucleating during the early stages of growth on the Fe(001) [Fig. 27(a)] and Fe(001)-$p(1 \times 1)$O [Fig. 27(b)] surfaces is about the same, suggesting a negligible effect of the oxygen overlayer on the intralayer mass transport of Cr atoms. At higher

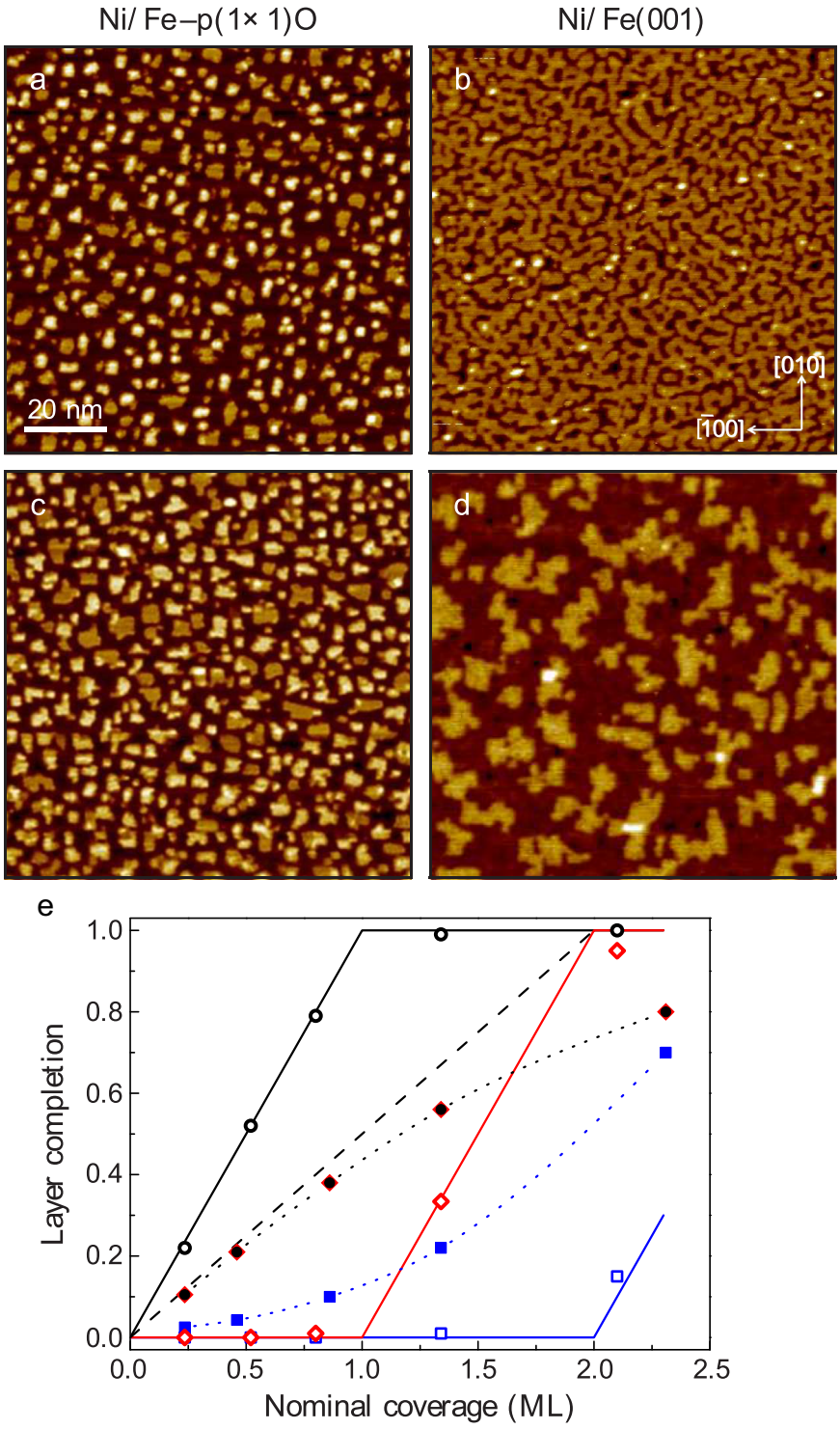

Fig. 30. STM topography after deposition of (a) 0.85 or (c) 1.35 ML of Ni on Fe(001)-$p(1 \times 1)$O, and (b) 0.85 or (d) 1.35 ML of Ni on Fe(001). (e) Layer completion fraction vs. the number of equivalent monolayers of deposited Ni. The first layer filling is indicated by black circles, the second by red diamonds, and the third layer by blue squares. Full (open) symbols are used for Ni growth on the Fe(001)-$p(1 \times 1)$O [Fe(001)] surface. The trend of both an ideal layer-by-layer growth (full lines) and an ideal two layers-by-two layers growth (dashed line) are also reported for comparison. Dotted lines: guide for the eye. Reprinted with permission from Ref. [257]. Copyright (2012) by the American Physical Society. (For interpretation of the references to color in this figure caption, the reader is referred to the web version of this paper.)

coverages, the oxygen overlayer, floating on top of the Cr film, promotes the development of a two-dimensional morphology [see Fig. 27(d)], while Cr deposited on the Fe(001) surface develops a rough surface [see Fig. 27(c)].

Another example of the influence that a ultra-thin surfactant oxide layer can have on the morphology of heteroepitaxial growth of thin metal layer is provided by the different morphologies exhibited by Co films grown on either the oxygen-free Fe

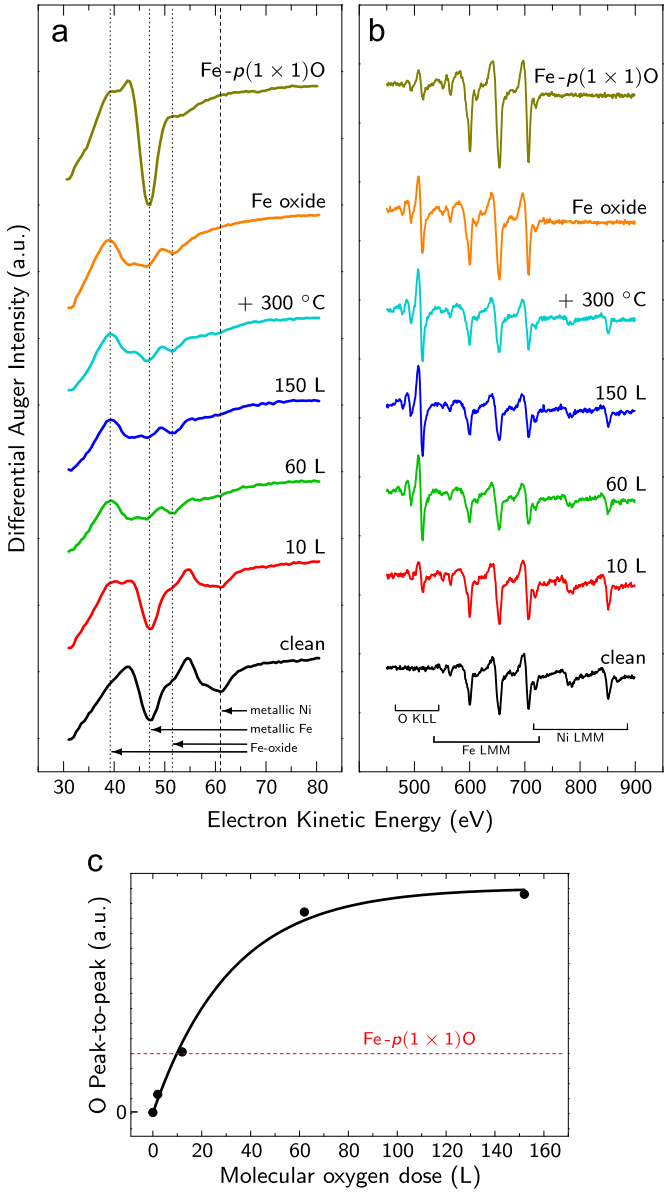

Fig. 31. AES spectra acquired after the oxidation of a 4 ML-thick Ni film deposited on Fe(001). (a) Ni and Fe MNN AES lineshape evolution for increasing oxygen exposure. After each oxygen dosing the sample was annealed for 5 min at 473 K. The reference spectra collected on the Fe(001)-$p(1 \times 1)$O surface and on a Fe(001) sample exposed to 50 L of oxygen are displayed in the upper part of panels (a) and (b). (b) AES spectra acquired in the high-kinetic region on the same samples of panel (a). (c) Oxygen KLL peak-to-peak intensity as a function of the oxygen dose. The intensity measured on the Fe(001)-$p(1 \times 1)$O surface (single layer of oxygen) is indicated by the horizontal dashed red line. Reprinted with permission from Ref. [279]. Copyright (2014) by Elsevier. (For interpretation of the references to color in this figure caption, the reader is referred to the web version of this paper.)

(001) and the oxygen-saturated Fe(001)-$p(1 \times 1)$O surface. In the latter case, AES spectroscopy confirms that O atoms keep floating on the Co film surface during deposition [273]. Constant-current STM images reveal that the Co growth on the oxygen-free surface proceeds in a layer-by-layer mode up to about 9 ML [see Fig. 28(a)], after which such a growth mode is destabilized by plastic deformations induced by the relaxation of the strain accumulated in the film [153]. Conversely, when Co is deposited on the Fe(001)-$p(1 \times 1)$O, a wetting layer is completed only after a coverage of 2 ML, then a nearly perfect layer-by-layer growth is initiated. This proceeds much further with respect to the former case, extending at least up to 17 ML [see Fig. 28(b)].

Further hints about the role of the oxygen overlayer in determining the structural properties of Co/Fe(001) or Co/Fe-$p(1 \times 1)$O are provided by the analysis of the island density as a function of coverage [see Fig. 29]. A Co atom landing on the substrate diffuses over the surface, until it encounters another diffusing atom and forms a dimer that anchors to the substrate, nucleating an island. At higher coverages, the number of nucleated islands per unit area increases up to a critical value. Further deposition of material induces the growth of already present islands, which start merging together. In this way, the density of islands on the layer reaches a maximum (known as "saturation island density"), until a complete wetting layer covers the substrate. The same scenario then repeats for the subsequent layers. In the case of deposition onto oxygen-free Fe(001), the saturation island density drastically decreases, by almost two orders of magnitude, for increasing Co coverages. Conversely, when Co is evaporated onto Fe(001)-$p(1 \times 1)$O, the saturation island density is not affected by the Co film thickness across the 0–17 ML coverage range.

DFT calculations suggest that the remarkable decrease of the saturation island density on a Co/Fe(001) film is due to an enhancement of atomic diffusion driven by the increasing capability of the film to accommodate large deformations as the thickness approaches the limit at which a structural transition occurs [153]. In the case of Co/Fe(001)-$p(1 \times 1)$O, the presence of the oxide overlayer completely change the diffusion mechanisms of Co adatoms, leading to a thickness-independent diffusion coefficient [273].

An interesting case in which the oxygen overlayer changes the growth mode in the opposite direction, i.e. inducing a three-dimensional morphology when the growth on the oxygen free-surface proceeds in the layer-by-layer mode, has been found in the early stages of Ni growth on Fe(001)-$p(1 \times 1)$O [257]. As already discussed in Section 4.2, the Ni growth on the oxygen-passivated surface starts by the nucleation of bi-layer islands, while single layer islands nucleate over the oxygen-free surface. Fig. 30 focuses on thicker Ni films than those shown in Fig. 24, deposited on either Fe(001)-$p(1 \times 1)$O [panels (a) and (c)] or Fe(001) [panels (b) and (d)]. The layer completion graph, displayed in Fig. 30(e), shows that, when Ni is deposited on Fe(001)-$p(1 \times 1)$O, the third layer develops well-before the completion of the first two, resulting in a three-dimensional growth. On the other hand, a nearly perfect layer-

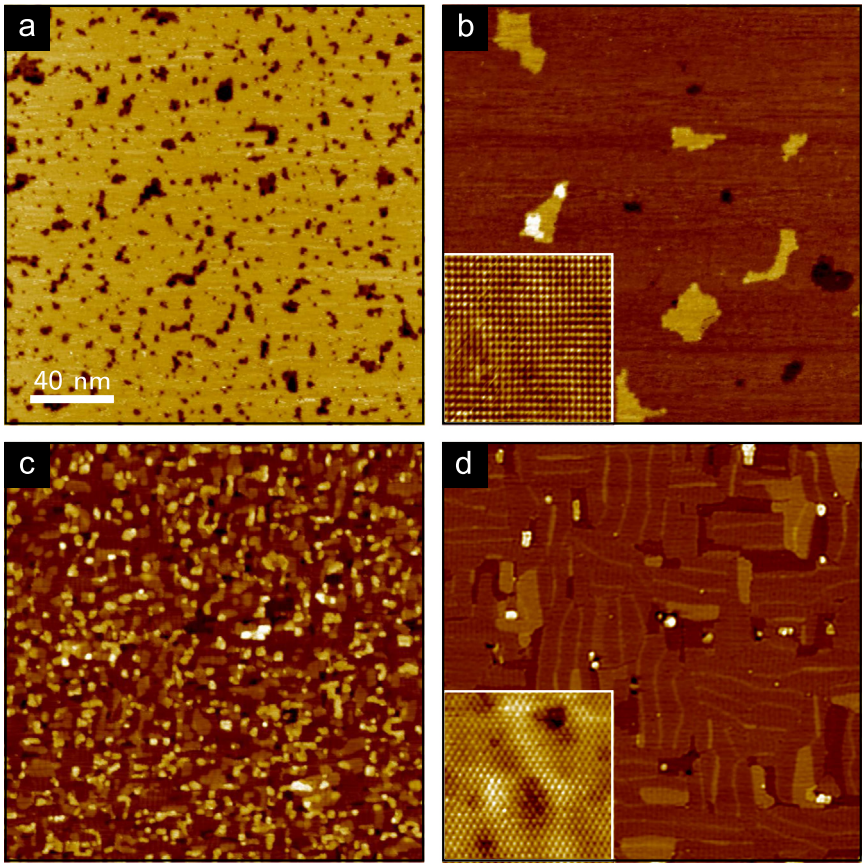

Fig. 32. STM topography of (a) the pristine 4 ML Ni/Fe(001) surface; (b) the same film after exposure to 10 L of O_2 and annealing at 473 K; (c) the sample of panel (b) dosed with 150 L of O_2 and annealed at 473 K; (d) the sample of panel (c) annealed at 573 K in UHV conditions. Reprinted with permission from Ref. [279]. Copyright (2014) by Elsevier.

by-layer growth is observed in the case of Ni deposited on the oxygen-free surface.

4.4. Oxidation of metallic buffer layers on Fe(001)

In this section we discuss the effects of oxygen-exposure on metallic buffer layers deposited on Fe(001). Important phenomena that need to be accounted for to understand these heterostructures include oxygen-induced segregation of atomic species from the substrate to the surface, surface roughening, and interfacial intermixing. In particular, the possibility of stabilizing an oxide by post-deposition oxidation of a metal on Fe(001) is an issue that bears many points in common with the wetting behavior of ultra-thin oxides on Fe(001) (see Section 4.2). For instance, while a sharp NiO/Fe(001) interface cannot be obtained by either post-oxidation of an Ni films deposited on Fe(001) or by exploiting the preloaded oxygen on Fe(001)-$p(1 \times 1)$O, chemically stable Cr ultra-thin oxides on Fe(001) can be obtained by following both strategies [279,280].

A Ni buffer layer grown on the Fe(001) surface is not effective in protecting the substrate from oxidation, since oxygen exposure induces the segregation of Fe atoms towards the surface, where their oxidation takes place. Fig. 31 reports the evolution of AES spectra acquired on 4 ML Ni/Fe(001) treated with cycles of room

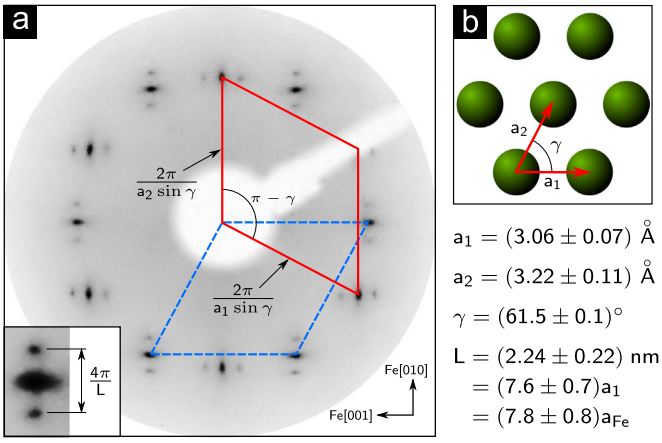

Fig. 33. (a) LEED pattern (primary energy = 100 eV) of the Ni/Fe sample dosed with 150 L of oxygen and annealed at 573 K. Two orthogonal rotational quasi-hexagonal domains are visible. The reciprocal unit cells are drawn in red (solid line) and blue (dashed line). A blow-up of one of the spots is reported in the inset, where the contrast has been artificially enhanced to increase the visibility of the mutually orthogonal elongation and spot splitting. The relevant parameters extracted from the pattern to obtain the real-space atomic unit cell (main panel) and the supercell periodicity (inset) are indicated. (b) Real space model atomic Bravais lattice for the quasi-hexagonal overlayer as obtained from the LEED pattern in (a). The numerical values of the parameters are also reported. Reprinted with permission from Ref. [279]. Copyright (2014) by Elsevier. (For interpretation of the references to color in this figure caption, the reader is referred to the web version of this paper.)

temperature oxygen exposure and annealing in UHV. The freshly deposited ultra-thin Ni films are exposed to an increasing dose of molecular oxygen at room-temperature [oxygen partial pressure during the oxidation from 10^{-9} mbar for the lowest exposure and 10^{-7} mbar for the highest one (150 L)], and subsequently annealed in UHV at 473 K for 5 min. Before the oxidation treatment, the low-energy AES spectrum [Fig. 31(a)] of the as-grown sample is characterized by the presence of two main peaks located at 47 eV and 61 eV, related to metallic Fe and Ni, respectively. Upon a 10 L oxygen exposure, a shoulder appears at lower kinetic energy with respect to the metallic Fe peak. Such a shoulder is analogous to the one present on the Fe(001)-$p(1 \times 1)$O surface (see Section 4.1), suggesting the formation of O–Fe bonds. Increasing the oxygen exposure up to 60 L clearly enhances the intensity of the peaks associated with O-bound Fe atoms, while the Ni peak almost disappears. Further increase of the oxygen exposure up to 150 L and the final annealing at 573 K in UHV do not significantly change the shape and the intensity of the measured peaks. In the high kinetic energy region [Fig. 31(b)], in which the mean free path of electrons is longer, i.e. AES spectra are less surface sensitive, it is possible to notice that the Ni peak intensity does not vanish, indicating that some Ni is present underneath the Fe oxide film.

STM topographies corresponding to each oxidation step are displayed in Fig. 32. Before oxidation, Ni films display an atomically smooth surface [Fig. 32(a)], with mainly two layers exposed, as expected for a layer-by-layer growth. Upon exposure to 10 L of molecular oxygen, the surface retains a flat morphology [Fig. 32(b)]. Thanks to the oxygen-induced increase of the atomic corrugation, atomic resolution is achieved, showing a lattice with square symmetry and in-plane periodicity equal to that of the Fe(001)-$p(1 \times 1)$O surface (2.87 Å). However, based on AES spectra, this surface atomic layer is expected to be Fe oxide. Increasing the oxygen exposure to 60 L promotes surface roughening [Fig. 32(c)]. Annealing the sample at 573 K in UHV conditions induces the development of large atomically flat terraces, visible in Fig. 32(d). Moreover, the atomically resolved image displayed in the inset of Fig. 32(d) reveals that the unit cell switches from the square symmetry characterizing the early stages of oxidation to the hexagonal one.

Such hexagonal arrangement of surface atoms is also visible in the LEED pattern of Fig. 33(a), revealing the presence of two orthogonal domains, aligned along the main crystallographic directions of the Fe(001) surface. The analysis of the LEED pattern provides the structural model of Fig. 33(b). The direct-space basis vectors are about 3.06 Å and 3.22 Å long, rotated by an angle of $(61.5 \pm 0.1)^{\circ}$. Being the nearest-neighbor spacing between atoms in the FeO(111) surface equal to $a_{FeO} = 3.04$ Å [281], this analysis suggests that the overlayer consists of a FeO(111) distorted film.

The film surface appears to be modulated, as revealed by the splitting of the LEED diffraction spots as well as by STM images reported in Fig. 34. Two mutually orthogonal modulations are visible, the first one largely variable from about 7 to 15 nm [see

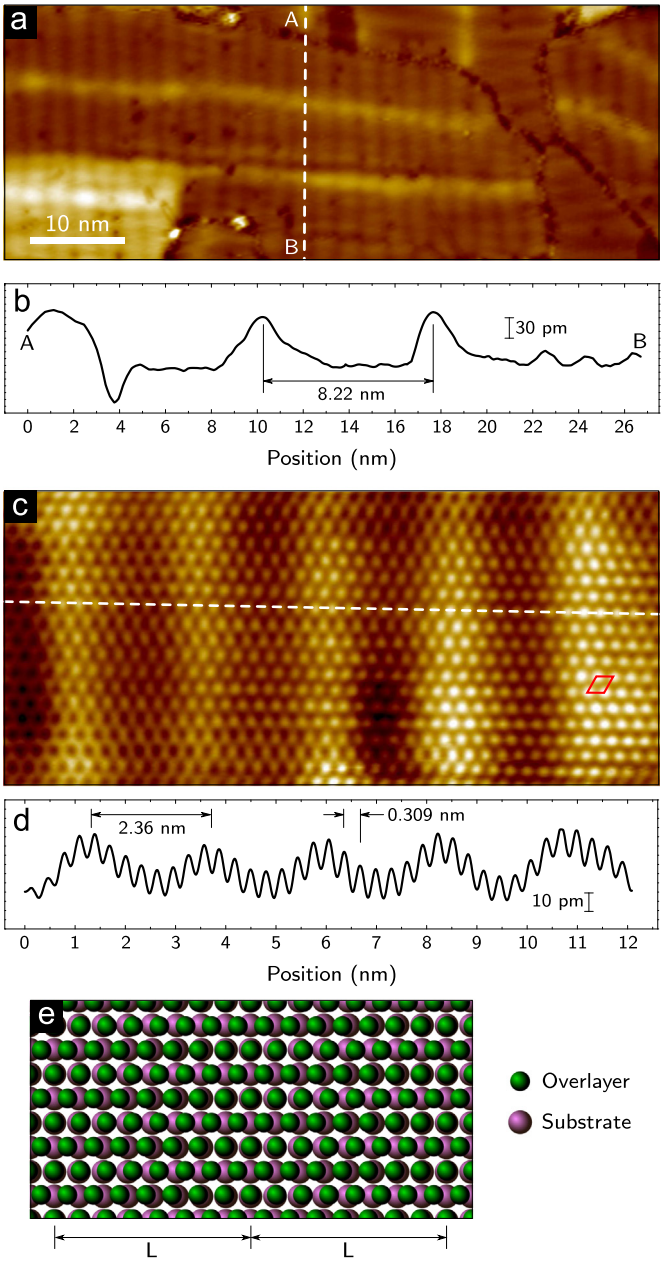

Fig. 34. 4 ML Ni/Fe(001) surface dosed with 150 L of oxygen and heated at 573 K. (a) Large scale STM topography ($I = 1$ nA, $V = 1$ V) showing several rotational domains characterized by the mutually orthogonal surface undulations. (b) Topographic profile acquired along the dashed white line in (a). The peak-to-peak distance between the maxima of the longer modulation visible in (a) is indicated. (c) Atomically resolved STM topography ($I = 5$ nA, $V = 0.1$ V) of one of the rotational domains, showing the detail of the short-period modulation. The distorted hexagonal atomic unit cell is indicated in red on the right. (d) Height profile along the dashed white line in (c). The modulation periodicity (L) and the $\mathbf{a}_1$-unit vector length are indicated (refer to Fig. 33 for the notation). (e) Result of the superposition of the distorted hexagonal lattice (green; unit vectors and relative orientation as measured from the LEED pattern in Fig. 33) and a square lattice (violet) with the same spatial periodicity of Fe(001). The short-period modulation results from the quasi-coincidence of the two lattices along the $\mathbf{a}_1$ direction. Reprinted with permission from Ref. [279]. Copyright (2014) by Elsevier. (For interpretation of the references to color in this figure caption, the reader is referred to the web version of this paper.)

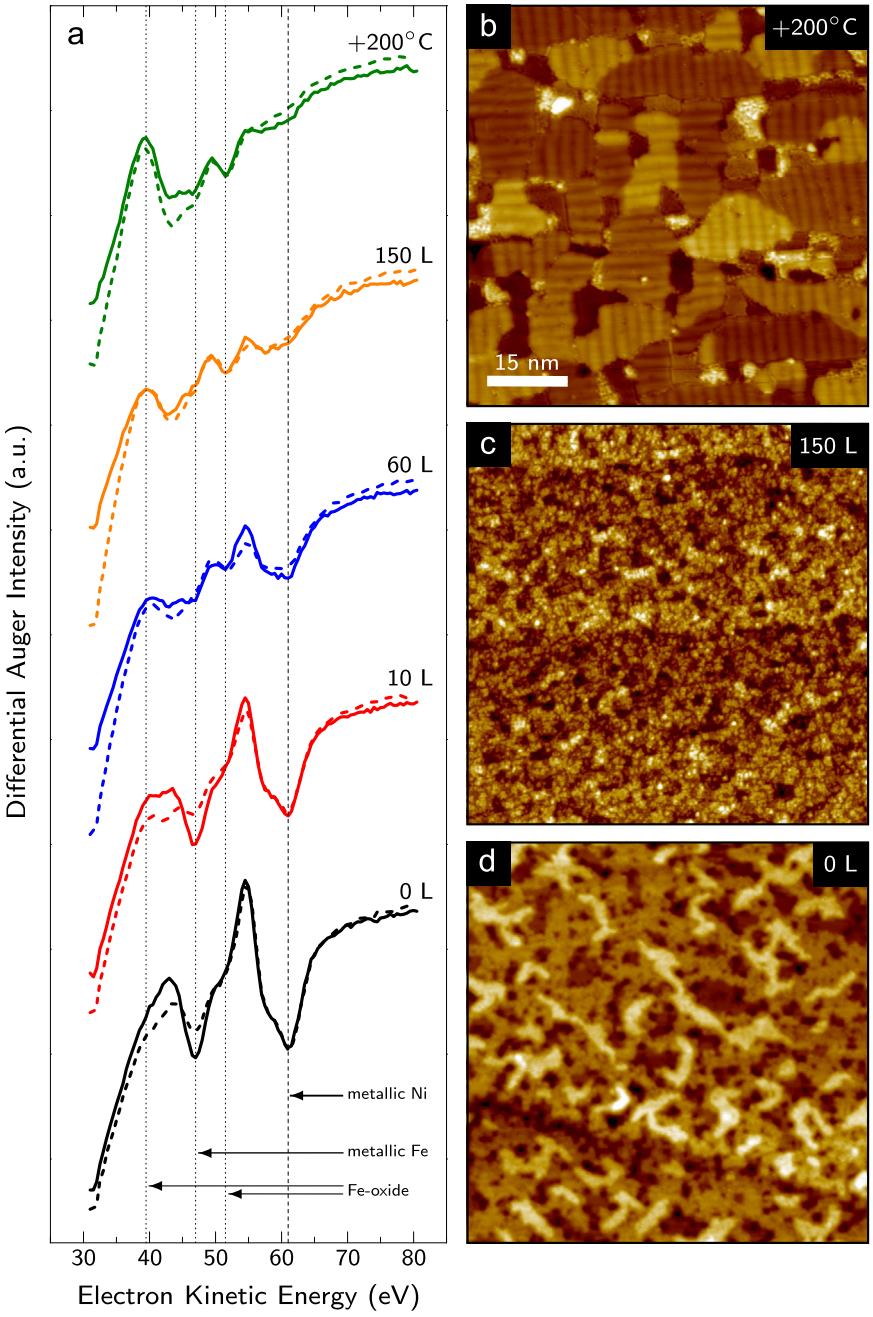

Fig. 35. (a) Low kinetic energy Auger spectra for the 5 ML-thick Ni/Fe(001) sample at different oxygen exposures. No post-annealing treatment was performed until the highest dose of 150 L was reached. The topmost spectrum refers to the final sample (150 L oxygen) after a mild-temperature annealing. Solid and dashed curves refer to spectra acquired at normal and grazing (sample normal 77° tilted with respect to the incident electron beam) emissions, respectively. The position of relevant Ni (dashed) and Fe (dotted) transitions is marked by vertical lines. (b–d) STM images for the sample at a selection of the preparation steps. Namely (d) pristine Ni/Fe(001), (c) 150 L and (b) 150 L + annealing at 473 K. Reprinted with permission from Ref. [279]. Copyright (2014) by Elsevier.

Fig. 34(a) and (b)] and a second one with a shorter period of 2.36 nm [see Fig. 34(c) and (d)]. These two mesoscopic-range periodic modulations arise from the superposition of the surface hexagonal lattice with the square lattice of the Fe(001) surface, resulting in the quasi-coincidence superlattice displayed in Fig. 34(e).

The oxygen-induced Fe segregation is observed also when oxygen is dosed on the Ni/Fe(001) sample without any intermediate annealing step. Fig. 35 displays the AES spectra [panel (a)] and the STM morphology [panel (b)] resulting from the oxidation of a 5 ML Ni/Fe(001) sample, where the annealing step was performed only on the sample dosed with the highest amount of oxygen (150 L). The Fe oxide peak appears after oxygen exposure, being more pronounced for spectra acquired at grazing incidence [dashed spectra in Fig. 35(a)], an observation suggesting that Fe oxidation takes place in the surface region. The final annealing step increases the amount of the superficial Fe oxide, in line with previous works [42].

STM topography acquired on the 5 ML Ni/Fe(001) system before oxygen exposure [Fig. 35(d)] reveals that the film

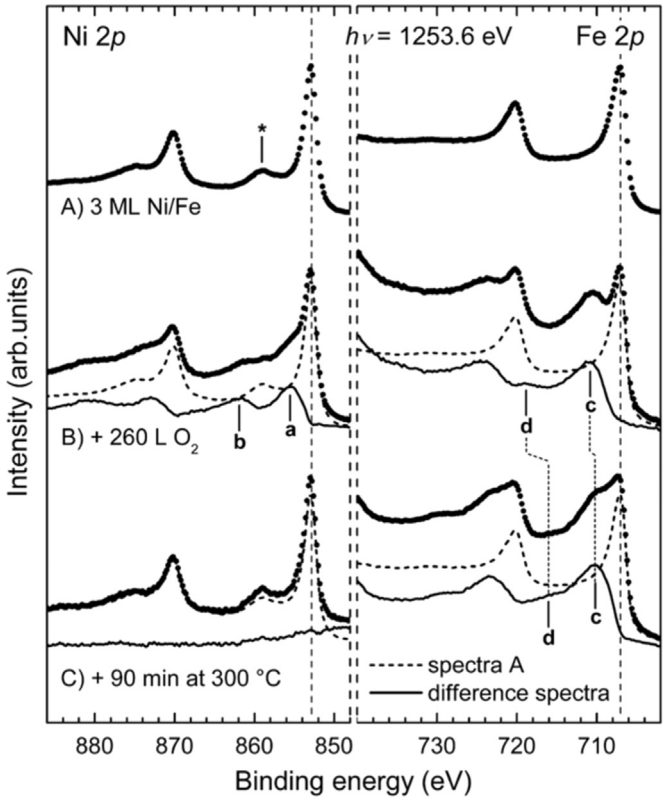

Fig. 36. XPS scans of the Ni 2*p* and Fe 2*p* regions of a 3 ML Ni/Fe(001) sample. (A) as-grown, (B) exposed to 260 L of O_2 at room temperature and (C) annealed at 573 K for 90 min in UHV. All spectra have been acquired at grazing emission (photoelectrons are emitted with an angle of 60° with respect to the surface normal) with Mg Kα radiation. Continuous lines are difference spectra obtained by subtracting the A spectra (dashed lines in spectra B and C) from the experimental data. All spectra have been normalized to the intensity of the as-grown component. Reprinted with permission from Ref. [280]. Copyright (2014) by IOP Publishing.

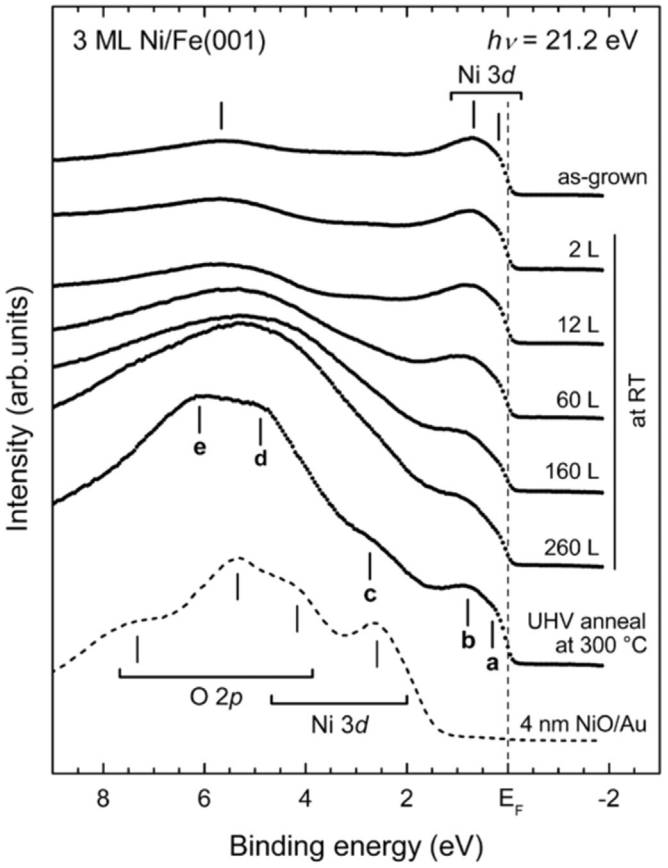

Fig. 37. UPS valence band of 3 ML Ni/Fe(001). Starting from the top: spectra acquired on the as-grown sample, on the oxidized surface at increasing oxygen dose and after an annealing in UHV at 300°C. Features at about 0.3 eV (a), 0.8 eV (b), 2.7 eV (c), 4.9 eV (d) and 6.0 eV (e) are highlighted in the last spectrum. The spectrum acquired on the NiO reference sample is shown with a dashed line. Adapted with permission from Ref. [280]. Copyright (2014) by IOP Publishing.

morphology is slightly rougher with respect to the 4 ML Ni/Fe (001) sample. The roughness keeps increasing upon oxygen exposure at room temperature, as visible in the STM image acquired after dosing the sample with 150 L of O_2 [Fig. 35(b)]. Interestingly, the final annealing step again drives the development of the modulated FeO(111) film [Fig. 35(c)], suggesting that this phase is particularly stable, irrespective of the preparation procedure.

Further insights in the Ni/Fe(001) oxidation mechanisms come from XPS and UPS [280]. In this case the oxidation is performed by exposing a 3 ML Ni/Fe(001) sample to O_2. Fig. 36 displays the XPS spectra acquired in the Fe 2*p* and Ni 2*p* regions. The analysis of the evolution of the Fe 2*p* and Ni 2*p* lineshapes upon room-temperature oxidation of Ni/Fe(001) confirms the development of Fe oxides on the surface layer, but also reveals the presence on Ni^{2+} ions (see spectra B of Fig. 36). Spectra C of Fig. 36, acquired after annealing the film in UHV, reveal that the thermal treatment completely reduces the Ni ions, increasing the amount of oxidized Fe. The evolution of the lineshape in UPS spectra upon oxidation is shown in Fig. 37. It is possible to notice that the UPS spectra acquired after the oxidation of the Ni/Fe(001) sample significantly differ from those of a NiO/Au reference sample [282], confirming that the Ni oxidation is negligible. Furthermore, the spectral features a–e visible after UHV annealing strongly resemble those observed in photoemission from the (111) face of FeO [283,284].

The presented results point towards the impossibility of obtaining an atomically sharp NiO/Fe(001) interface. This conclusion can be rationalized from the one hand by considering the competition for oxidation between the Ni film and the more oxidizable Fe(001) substrate (see Table 1), on the other hand with the general oxidation reluctance of Ni films supported by a metallic substrate [285].

The observation of a non-reconstructed FeO(111) surface on top of the Ni/Fe(001) square substrate deserves some further discussion for two reasons. In the first place, because of the quasi-hexagonal symmetry of the bcc (110) surface, FeO(111)-like films generally form upon oxidation of the Fe(011) surface [286,287] or by reactive growth of Fe oxide on Fe(011) [288]. Conversely, the formation of the FeO(111) film on the Ni/Fe (001) substrate results in a symmetry-mismatched interface between the hexagonal oxide layer and the square substrate lattice. Generally, the stabilization of (111)-oriented rocksalt oxides on square substrates is associated with a large mismatch between the oxide overlayer and the substrate, as in the case of

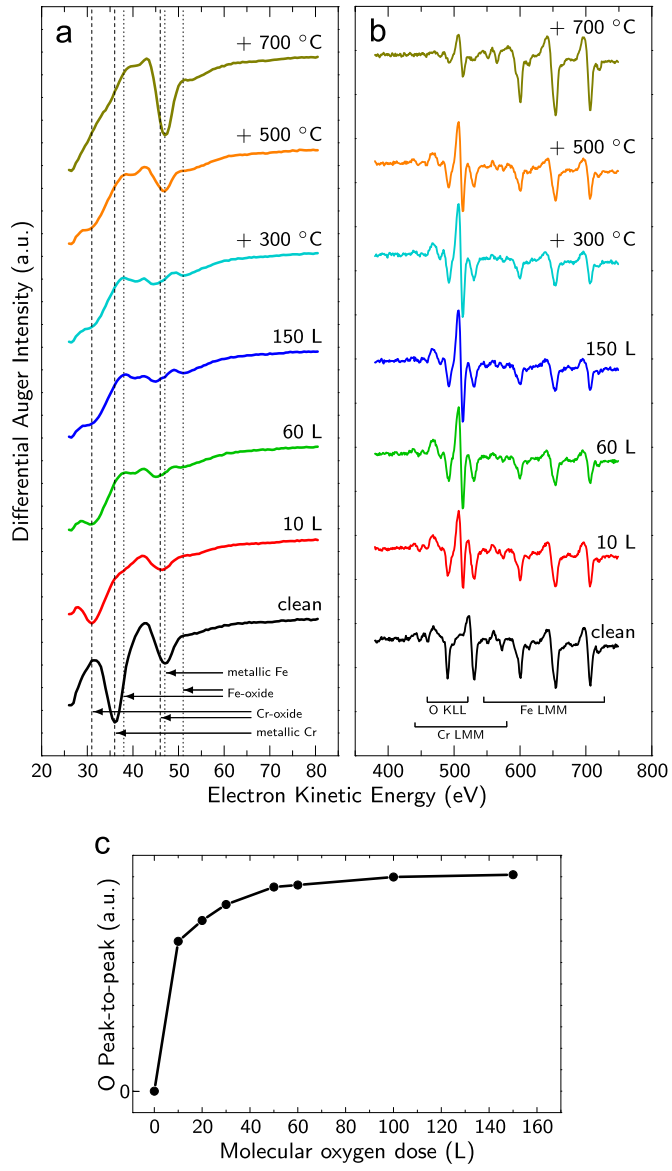

Fig. 38. (a) Low kinetic energy Auger spectra for a Cr/Fe(001) sample at different oxygen exposures and after post-annealing treatments. The position of relevant metallic and oxide features for both Cr (dashed) and Fe (dotted) is indicated. (b) High kinetic energy Auger spectra corresponding to samples in (a), where the position of Fe and Cr LMM and O KLL transitions is highlighted. (c) Evolution of the oxygen peak-to-peak intensity as a function of the oxygen dose. Reprinted with permission from Ref. [279]. Copyright (2014) by Elsevier.

MnO on Rh(100) [289] or CoO on Ir(001) [290]. In addition, the (111) surfaces of bulk rocksalt oxides are unstable because of the development of a dipole moment perpendicular to the surface,[2] due to the alternation of atomic planes formed by oppositely charged ions [293,294]. These two circumstances would conspire to rather induce the preferential stabilization of a FeO(001) surface, which is charge-compensated and possesses a small lattice mismatch with respect to Fe(001). Further theoretical insights is therefore needed to rationalize the mechanisms driving the stabilization of the observed FeO (111)-like film.

A completely different oxidation path is observed in the case of Fe(001)-supported Cr ultra-thin films [279,280]. In this case Fe segregation and oxidation is not observed during the early stages of oxygen exposure. Auger spectra acquired after oxidation and post-annealing treatments on 4 ML Cr/Fe(001) samples are displayed in Fig. 38, where panels (a) and (b) refer to the low and high kinetic energy regions, respectively. In the oxygen-free sample, the peaks arising from metallic Fe (47 eV) and metallic Cr (36 eV) are visible [see Fig. 38(a)]. After exposure to 10 L of O_2 and post-annealing treatment, the feature associated to metallic Cr is no longer visible, substituted by a peak at 31 eV, related to the presence of Cr oxide. Importantly, no features related to Fe oxide are present at this stage. Upon increasing the oxygen dose up to 150 L, the characteristic shoulder of O-bound Fe appears in the spectrum. UHV annealing at increasing temperatures leads to the dissolution of the Cr oxide film, as visible in the upper spectra of Fig. 38(a) and (b). Notice that the oxygen uptake for the Cr/Fe(001) system, displayed in Fig. 38(c), is steeper than that observed in the case of Ni/Fe(001) oxidation [see Fig. 31(c)].

Despite Cr oxide overlayers can be stabilized on top of Fe(001), the resulting morphology is particularly rough, making their investigation at the atomic scale difficult. The acquired STM topography reveals that the surface roughness increases after the oxidation step [see Fig. 39(b) and (c) for 10 L and 150 L of oxygen exposure, respectively]. Annealing treatments up to 673 K do not significantly affect the sample morphology. On the other hand, annealing in UHV at 773 K induces the formation of holes in the Cr oxide film [Fig. 39(d)]. The STS data of Fig. 39(e) show that a conductivity gap is present on the remaining film, while the electronic structure of the holes is different and strongly resembles the one characteristic of Fe(001)-$p(1 \times 1)$O (see Section 4.1).

The chemical stability of the Cr oxide/Fe(001) interface is confirmed also by XPS. In this case, 3 ML-thick Cr films were grown using the Fe(001)-$p(1 \times 1)$O surface as a substrate, i.e. the sample before oxidation (to which spectra A in Fig. 40 refer) already has a single layer of oxygen on top [278]. A room-temperature oxidation (spectra B of Fig. 40) partially oxidizes the Cr film, leaving however the Fe(001) substrate in a metallic state. The interface is stable even after annealing at 300 °C in UHV, as demonstrated by spectra C of Fig. 40, where the Fe 2p peaks do not present any feature related to Fe oxide species. On the other hand, the contribution from the metallic Cr layer is slightly attenuated, likely because of a partial interdiffusion of Cr atoms into the Fe(001) substrate bulk occurring after the annealing treatments. In order to completely convert the Cr film into Cr oxide, the oxidation must be performed at high temperatures. Spectra D of Fig. 40, acquired after further exposure to 10 L of O_2 at 300 °C, reveal that the Cr film is completely oxidized. The Fe 2p lineshape displays a component characteristic of Fe^{2+} species, indicating

[2] It should be mentioned that only the (111) bulk termination of rocksalt oxides is rigorously unstable, while in the two-dimensional limit additional charge- and polarity-compensation mechanisms become operative, see for instance [291,292].

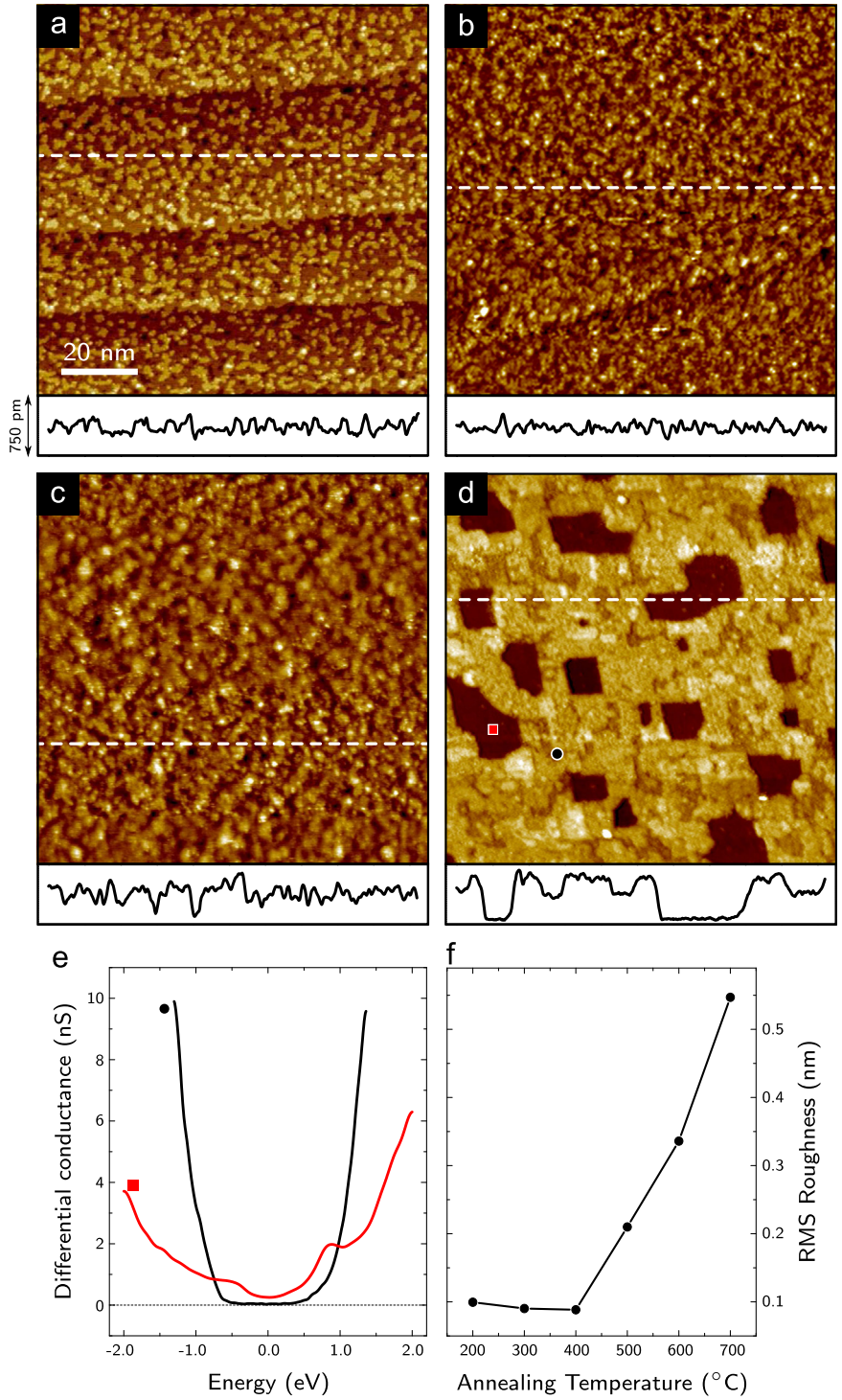

Fig. 39. STM topography of a Cr/Fe(001) sample after oxidation and annealing. (a) As-grown Cr film, (b) 10 and (c) 150 L oxygen exposure, (d) 150 L + annealing at 773 K. Height profiles along the corresponding dashed white lines are reported at the bottom of each panel. Vertical scale is 750 pm. (e) STS spectra acquired at correspondence with the holes (red square) and on the Cr film (black circle) in (d). (f) Root mean square (RMS) roughness of the sample measured on 200×200 nm^2 STM images as a function of the thermal treatments. Reprinted with permission from Ref. [279]. Copyright (2014) by Elsevier. (For interpretation of the references to color in this figure caption, the reader is referred to the web version of this paper.)

Fe(001) substrate oxidation. However, at variance with the Ni/Fe(001) system, for the Cr/Fe(001)-$p(1 \times 1)$O sample Fe oxidation starts only after the complete oxidation of the Cr film, suggesting the feasibility of obtaining a sharp Cr-oxide/Fe(001) interface by a proper choice of temperature and oxygen dosing.

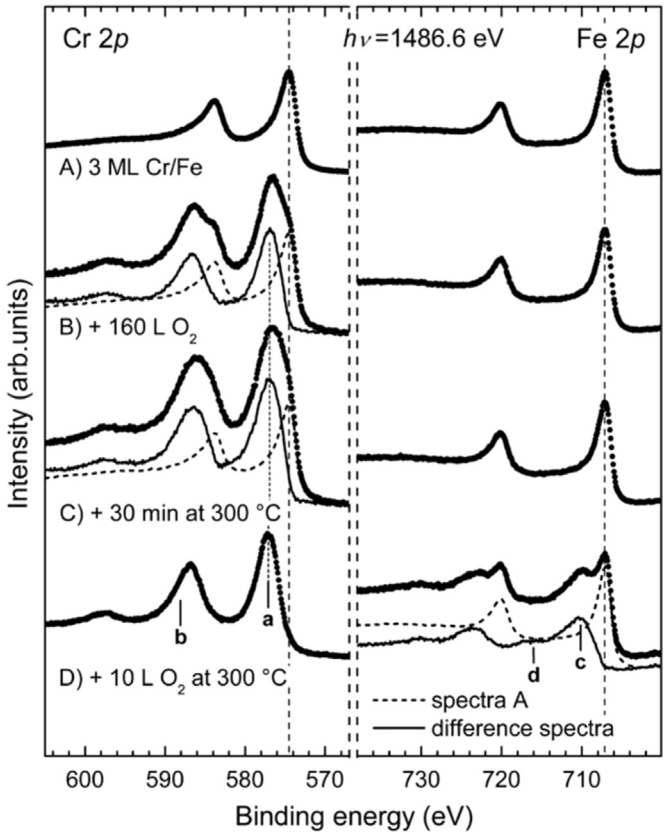

Fig. 40. XPS scans of the Fe 2*p* and Cr 2*p* regions of 3 ML Cr/Fe(001)-$p(1 \times 1)$ O. (A) As grown, (B) dosed with 160 L of O_2 at room temperature, (C) annealed at 573 K for 90 min in UHV and (D) exposed to 10 L of O_2 at 573 K. Continuous lines are difference spectra obtained by subtracting the A spectra (dashed lines in spectra from B to C) from the experimental data. Reprinted with permission from Ref. [280]. Copyright (2014) by IOP Publishing.

5. Conclusions

The presented experimental results reveal, on one hand, the extreme complexity of the metal-oxide interfaces, and on the other hand, the dramatic effects that even moderate compositional modifications of the interface can induce on the overall structural, electronic and magnetic properties of such heterostructures. The possibility to tune the properties of a material relies to a large extent on the experimental ability to control the structure and chemistry of the metal–oxide interface at the atomic level. Model systems as those presented here are fundamental for the rationalization of the processes occurring in layered O/M and M/O systems and allow for a direct correlation between their properties and interface composition. Such an approach has been and still is extensively applied on oxide ultra-thin films supported by inert metals, but can be also extended to investigate oxide films supported on highly reactive substrates, despite the additional experimental drawbacks encountered in the stabilization of well-ordered structures. In this respect, we have provided a survey of the information that can be obtained about the complex mechanisms driving the interface formation between a reactive metal and an oxide, with particular attention dedicated to the prototypical case of ultra-thin oxides grown of Fe(001). We are confident that, thanks to the extreme importance of metal–oxide interfaces, their investigation will still be in the focus of fundamental research for the next years, providing important insights for future technological applications.

Acknowledgments

The authors would like to thank all the colleagues and friends, whom they had the opportunity to work and discuss with during their activity concerning this work. Among these, a special mention goes to (in alphabetical order) S. Achilli, G. Berti, C. E. Bottani, C. S. Casari, F. Donati, G. Fratesi, D. Giannotti, A. Li Bassi, M. Passoni, and M. I. Trioni.

This work was partially supported by the Italian Ministry of University and Research trough the FIRB project RBAP115AYN. Financial support was provided also by GEMINI (FP7-FET-OPEN X-TRACK No. 2013-0623). Computational resources were made available in part by CINECA (application code HP10C3YWUA). A. Picone would like to dedicate this work to Alice, who hopefully will live in a wonderland, who already made the world a wonderful place.

References

[1] H.-J. Freund, S. Shaikhutdinov, N. Nilius, Top. Catal. 57 (10–13) (2014) 822–832, http://dx.doi.org/10.1007/s11244-014-0276-6.

[2] X. Guo, Q. Fu, Y. Ning, M. Wei, M. Li, S. Zhang, Z. Jiang, X. Bao, J. Am. Chem. Soc. 134 (30) (2012) 12350–12353, http://dx.doi.org/10.1021/ja3038883.

[3] S. Surnev, A. Fortunelli, F.P. Netzer, Chem. Rev. 113 (6) (2013) 4314–4372, http://dx.doi.org/10.1021/cr300307n URL ⟨http://pubs.acs.org/doi/abs/10.1021/cr300307n⟩.

[4] G. Pacchioni, L. Skuja, D.L. Griscom (Eds.), Defects in SiO_2 and Related Dielectrics: Science and Technology, Kluwer, Dordrecht, 2000, 2012. http://dx.doi.org/10.1007/978-94-010-0944-7.

[5] C. Cagli, F. Nardi, B. Harteneck, Z. Tan, Y. Zhang, D. Ielmini, Small 7 (20) (2011) 2899–2905, http://dx.doi.org/10.1002/smll.201101157.

[6] V. Skumryev, S. Stoyanov, Y. Zhang, G. Hadjipanayis, D. Givord, J. Nogués, Nature 423 (2003) 850–853, http://dx.doi.org/10.1038/nature01687 URL ⟨http://www.nature.com/nature/journal/v423/n6942/full/nature01687.html⟩.

[7] S. Valeri, G. Pacchioni (Eds.), Oxide Ultrathin Films, Wiley-VCH Verlag GmbH & Co. KGaA, Weinheim, 2011 Chapter 6, URL ⟨http://eu.wiley.com/WileyCDA/WileyTitle/productCd-352733016X.html⟩.

[8] R. Gupta, N. Birbilis, Corros. Sci. 92 (2015) 1–15, http://dx.doi.org/10.1016/j.corsci.2014.11.041 URL ⟨http://www.sciencedirect.com/science/article/pii/S0010938X14005629⟩.

[9] A. Stoneham, P. Tasker, J. Phys. 49 (C-5) (1988) 99–113, http://dx.doi.org/10.1051/jphyscol:1988508.

[10] F.H. Stott, Rep. Prog. Phys. 50 (7) (1987) 861 URL ⟨http://stacks.iop.org/0034-4885/50/i=7/a=002⟩.

[11] J. Wu, D. Carlton, J.S. Park, Y. Meng, E. Arenholz, A. Doran, A. T. Young, A. Scholl, C. Hwang, H.W. Zhao, J. Bokor, Z.Q. Qiu, Nat. Phys. 7 (4) (2011) 303, http://dx.doi.org/10.1038/NPHYS1891.

[12] M. Finazzi, L. Duò, F. Ciccacci, Surf. Sci. Rep. 64 (4) (2009) 139–167 http://dx.doi.org/10.1016/j.surfrep.2008.12.003.

[13] G. Pacchioni, H. Freund, Chem. Rev. 113 (6) (2013) 4035–4072 http://dx.doi.org/10.1021/cr3002017.

[14] G. Radaelli, D. Petti, M. Cantoni, C. Rinaldi, R. Bertacco, J. Appl. Phys. 115 (17), (2014). http://dx.doi.org/10.1063/1.4870915, URL ⟨http://scitation.aip.org/content/aip/journal/jap/115/17/10.1063/1.4870915⟩.

[15] J. Mathon, A. Umerski, Phys. Rev. B 63 (2001) 220403, http://dx.doi.org/ 10.1103/PhysRevB.63.220403 URL ⟨http://link.aps.org/doi/10.1103/Phys RevB.63.220403⟩.
[16] S. Yuasa, T. Nagahama, A. Fukushima, Y. Suzuki, K. Ando, Nat. Mater. 3 (2004) 868–871, http://dx.doi.org/10.1038/nmat1257.
[17] S.A. Chambers, Surf. Sci. Rep. 39 (5–6) (2000) 105–180, http://dx.doi.org/ 10.1016/S0167-5729(00)00005-4 URL ⟨http://www.sciencedirect.com/science/article/pii/S0167572900000054⟩.
[18] C.T. Campbell, Surf. Sci. Rep. 27 (1–3) (1997) 1–111, http://dx.doi.org/ 10.1016/S0167-5729(96)00011-8 URL ⟨http://www.sciencedirect.com/science/article/pii/S0167572996000118⟩.
[19] Q. Fu, T. Wagner, Surf. Sci. Rep. 62 (11) (2007) 431–498 http://dx.doi.org/10.1016/j.surfrep.2007.07.001 URL ⟨http://www.sciencedirect.com/science/article/pii/S0167572907000635⟩.
[20] S. Schintke, S. Messerli, M. Pivetta, F. Patthey, L. Libioulle, M. Stengel, A. De Vita, W.-D. Schneider, Phys. Rev. Lett. 87 (2001) 276801 http://dx.doi.org/10.1103/PhysRevLett.87.276801 URL ⟨http://link.aps.org/doi/10.1103/PhysRevLett.87.276801⟩.
[21] S. Schintke, W.-D. Schneider, J. Phys.: Condens. Matter 16 (4) (2004) R49 URL ⟨http://stacks.iop.org/0953-8984/16/i=4/a=R02⟩.
[22] D.R. Lide (Ed.), CRC Handbook of Chemistry and Physics, CRC Press, Boca Raton, 2010.
[23] J.A. Dean (Ed.), Lange's Handbook of Chemistry, McGraw-Hill, Inc., Knoxville, 1998.
[24] G. Pacchioni, Phys. Chem. Chem. Phys. 15 (2013) 1737–1757 http://dx.doi.org/10.1039/C2CP43731G.
[25] M.T. Greiner, L. Chai, M.G. Helander, W.-M. Tang, Z.-H. Lu, Adv. Funct. Mater. 23 (2) (2013) 215–226, http://dx.doi.org/10.1002/adfm.201200993.
[26] A. Calloni, A. Ferrari, A. Brambilla, F. Ciccacci, L. Duò, Thin Solid Films 520 (11) (2012) 3922–3926, http://dx.doi.org/10.1016/j.tsf.2012. 01.045 URL ⟨http://www.sciencedirect.com/science/article/pii/S004060901 2000831⟩.
[27] Z. Li, Z. Zhang, Y.K. Kim, R.S. Smith, F. Netzer, B.D. Kay, R. Rousseau, Z. Dohnálek, J. Phys. Chem. C 115 (13) (2011) 5773–5783, http://dx.doi.org/10.1021/jp1108976.
[28] R. de Masi, D. Reinicke, F. Müller, P. Steiner, S. Hüfner, Surf. Sci. 515 (2–3) (2002) 523–537, http://dx.doi.org/10.1016/S0039-6028(02)01970-2 URL ⟨http://www.sciencedirect.com/science/article/pii/S0039602802019702⟩.
[29] S. Benedetti, P. Torelli, P. Luches, A. Rota, S. Valeri, Surf. Sci. 600 (18) (2006) 4251–4255, http://dx.doi.org/10.1016/j.susc.2006.01.152 URL ⟨http://www.sciencedirect.com/science/article/pii/S0039602806005577⟩.
[30] P. Luches, F. Pagliuca, S. Valeri, F. Illas, G. Preda, G. Pacchioni, J. Phys. Chem. C 116 (1) (2012) 1122–1132, http://dx.doi.org/10.1021/jp210241c.
[31] J. Schoiswohl, M. Sock, S. Eck, S. Surnev, M.G. Ramsey, F.P. Netzer, G. Kresse, Phys. Rev. B 69 (2004) 155403, http://dx.doi.org/10.1103/PhysRevB.69.155403 URL ⟨http://link.aps.org/doi/10.1103/PhysRevB.69.155403⟩.
[32] J. Schoiswohl, S. Surnev, M. Sock, S. Eck, M.G. Ramsey, F.P. Netzer, G. Kresse, Phys. Rev. B 71 (2005) 165437, http://dx.doi.org/10.1103/PhysRevB.71.165437 URL ⟨http://link.aps.org/doi/10.1103/PhysRevB.71.165437⟩.
[33] A.S. Walton, J. Fester, M. Bajdich, M.A. Arman, J. Osiecki, J. Knudsen, A. Vojvodic, J.V. Lauritsen, ACS Nano 9 (3) (2015) 2445–2453, http://dx.doi.org/10.1021/acsnano.5b00158.
[34] T.J. Regan, H. Ohldag, C. Stamm, F. Nolting, J. Lüning, J. Stöhr, R.L. White, Phys. Rev. B 64 (2001) 214422, http://dx.doi.org/10.1103/PhysRev B.64.214422 URL ⟨http://link.aps.org/doi/10.1103/PhysRevB.64.214422⟩.
[35] S. Benedetti, P. Luches, M. Liberati, S. Valeri, Surf. Sci. 572 (23) (2004) L348–L354, http://dx.doi.org/10.1016/j.susc.2004.09.025 URL ⟨http://www.sciencedirect.com/science/article/pii/S0039602804012440⟩.
[36] P. Luches, M. Liberati, S. Valeri, Surf. Sci. 532–535 (0) (2003) 409–414, http://dx.doi.org/10.1016/S0039-6028(03)00119-5 URL ⟨http://www.sciencedirect.com/science/article/pii/S0039602803001195⟩.
[37] P. Luches, V. Bellini, S. Colonna, L. Di Giustino, F. Manghi, S. Valeri, F. Boscherini, Phys. Rev. Lett. 96 (2006) 106106, http://dx.doi.org/10.1103/PhysRevLett.96.106106 URL ⟨http://link.aps.org/doi/10.1103/PhysRevLett.96.106106⟩.
[38] N. Srivastava, P.C. Srivastava, J. Appl. Phys. 111 (12) (2012) 123909, http://dx.doi.org/10.1063/1.4729857 URL ⟨http://scitation.aip.org/content/aip/journal/jap/111/12/10.1063/1.4729857⟩.
[39] N. Srivastava, T. Shripathi, P. Srivastava, J. Electron Spectrosc. Relat. Phenom. 191 (0) (2013) 20–26, http://dx.doi.org/10.1016/j.elspec.2013.09.003 URL ⟨http://www.sciencedirect.com/science/article/pii/S0368204813001461⟩.
[40] V. Bellini, L. Di Giustino, F. Manghi, Phys. Rev. B 76 (2007) 214432, http://dx.doi.org/10.1103/PhysRevB.76.214432 URL ⟨http://link.aps.org/doi/10.1103/PhysRevB.76.214432⟩.
[41] M. Finazzi, A. Brambilla, L. Duò, G. Ghiringhelli, M. Portalupi, F. Ciccacci, M. Zacchigna, M. Zangrando, Phys. Rev. B 70 (2004) 235420, http://dx.doi.org/10.1103/PhysRevB.70.235420 URL ⟨http://link.aps.org/doi/10.1103/PhysRevB.70.235420⟩.
[42] L. Duò, M. Portalupi, M. Marcon, R. Bertacco, F. Ciccacci, Surf. Sci. 518 (3)(2002) 234–242, http:/dx.doi.org/10.1016/S0039-6028(02)02194-5 URL ⟨http://www.sciencedirect.com/science/article/pii/S0039602802021945⟩.
[43] E. Młyńczak, P. Luches, S. Valeri, J. Korecki, J. Appl. Phys. 113 (23) (2013) 234315, http://dx.doi.org/10.1063/1.4811528 URL ⟨http://scitation.aip.org/content/aip/journal/jap/113/23/10.1063/1.4811528⟩.
[44] R. Abrudan, J. Miguel, M. Bernien, C. Tieg, M. Piantek, J. Kirschner, W. Kuch, Phys. Rev. B 77 (2008) 014411, http://dx.doi.org/10.1103/PhysRevB.77.014411 URL ⟨http://link.aps.org/doi/10.1103/PhysRevB.77.014411⟩.
[45] E. Młyńczak, B. Matlak, A. Kozioł-Rachwał, J. Gurgul, N. Spiridis, J. Korecki, Phys. Rev. B 88 (2013) 085442, http://dx.doi.org/10.1103/PhysRevB.88.085442 URL ⟨http://link.aps.org/doi/10.1103/PhysRevB.88.085442⟩.
[46] A. Brambilla, P. Sessi, M. Cantoni, L. Duò, M. Finazzi, F. Ciccacci, Thin Solid Films 516 (21) (2008) 7519–7524, http://dx.doi.org/10.1016/j.tsf.2008.04.058 URL ⟨http://www.sciencedirect.com/science/article/pii/S0040609008004525⟩.
[47] R. Bali, M.M. Soares, A.Y. Ramos, H.C.N. Tolentino, F. Yildiz, C. Boudot, O. Proux, M. De Santis, M. Przybylski, J. Kirschner, Appl. Phys. Lett. 100 (13) (2012) 132403, http://dx.doi.org/10.1063/1.3695158 URL ⟨http://scitation.aip.org/content/aip/journal/apl/100/13/10.1063/1.3695158⟩.
[48] A. Brambilla, A. Calloni, G. Berti, G. Bussetti, L. Duò, F. Ciccacci, J. Phys. Chem. C 117 (18) (2013) 9229–9236, http://dx.doi.org/10.1021/jp400159j.
[49] U. Diebold, Surf. Sci. Rep. 48 (58) (2003) 53–229, http://dx.doi.org/10.1016/S0167-5729(02)00100-0 URL ⟨http://www.sciencedirect.com/science/article/pii/S0167572902001000⟩.
[50] P. Luches, S. Benedetti, M. Liberati, F. Boscherini, I. Pronin, S. Valeri, Surf. Sci. 583 (23) (2005) 191–198, http://dx.doi.org/10.1016/j.susc.2005.03.038 URL ⟨http://www.sciencedirect.com/science/article/pii/S0039602805003171⟩.
[51] G. Sharma, A. Gupta, P. Rajput, Rüffer, J. Phys. D: Appl. Phys. 47 (34) (2014) 345305 URL ⟨http://stacks.iop.org/0022-3727/47/i=34/a=345305⟩.
[52] J. Balogh, I. Dézsi, C. Fetzer, J. Korecki, A. Kozioł-Rachwał, E. Młyńczak, A. Nakanishi, Phys. Rev. B 87 (2013) 174415, http://dx.doi.org/10.1103/PhysRevB.87.174415 URL ⟨http://link.aps.org/doi/10.1103/PhysRevB.87.174415⟩.
[53] S.R. Spurgeon, J.D. Sloppy, R. Tao, R.F. Klie, S.E. Lofland, J. K. Baldwin, A. Misra, M.L. Taheri, J. Appl. Phys. 112 (1) (2012) 013905, http://dx.doi.org/10.1063/1.4730630 URL ⟨http://scitation.aip.org/content/aip/journal/jap/112/1/10.1063/1.4730630⟩.
[54] E. Młyńczak, K. Freindl, N. Spiridis, J. Korecki, J. Appl. Phys. 113 (2) (2013) 024320, http://dx.doi.org/10.1063/1.4775707 URL ⟨http://scitation.aip.org/content/aip/journal/jap/113/2/10.1063/1.4775707⟩.
[55] A. Cattoni, D. Petti, S. Brivio, M. Cantoni, R. Bertacco, F. Ciccacci, Phys. Rev. B 80 (2009) 104437, http://dx.doi.org/10.1103/PhysRevB.80.104437 URL ⟨http://link.aps.org/doi/10.1103/PhysRevB.80.104437⟩.

[56] L. Plucinski, Y. Zhao, B. Sinkovic, E. Vescovo, Phys. Rev. B 75 (2007) 214411, http://dx.doi.org/10.1103/PhysRevB.75.214411 URL ⟨http://link.aps.org/doi/10.1103/PhysRevB.75.214411⟩.
[57] A. Tekiel, S. Fostner, J. Topple, Y. Miyahara, P. Grütter, Appl. Surf. Sci. 273 (2013) 247–252, http://dx.doi.org/10.1016/j.apsusc.2013.02.024 URL ⟨http://www.sciencedirect.com/science/article/pii/S0169433213003322⟩.
[58] H.L. Meyerheim, R. Popescu, N. Jedrecy, M. Vedpathak, M. Sauvage-Simkin, R. Pinchaux, B. Heinrich, J. Kirschner, Phys. Rev. B 65 (2002) 144433, http://dx.doi.org/10.1103/PhysRevB.65.144433 URL ⟨http://link.aps.org/doi/10.1103/PhysRevB.65.144433⟩.
[59] T. Bertrams, H. Neddermeyer, J. Vac. Sci. Technol. B 14 (2) (1996) 1141–1144, http://dx.doi.org/10.1116/1.588416 URL ⟨http://scitation.aip.org/content/avs/journal/jvstb/14/2/10.1116/1.588416⟩.
[60] I. Sebastian, T. Bertrams, K. Meinel, H. Neddermeyer, Faraday Discuss. 114 (1999) 129–140, http://dx.doi.org/10.1039/A903416A.
[61] M. Caffio, A. Atrei, B. Cortigiani, G. Rovida, J. Phys.: Condens. Matter 18 (8) (2006) 2379 URL ⟨http://stacks.iop.org/0953-8984/18/i=8/a=003⟩.
[62] A. Dhaka, D. Sander, H.L. Meyerheim, K. Mohseni, E. Soyka, J. Kirschner, W.A. Adeagbo, G. Fischer, A. Ernst, W. Hergert, Phys. Rev. B 84 (2011) 195441, http://dx.doi.org/10.1103/PhysRevB.84.195441 URL ⟨http://link.aps.org/doi/10.1103/PhysRevB.84.195441⟩.
[63] W. Steurer, F. Allegretti, S. Surnev, G. Barcaro, L. Sementa, F. Negreiros, A. Fortunelli, F.P. Netzer, Phys. Rev. B 84 (2011) 115446, http://dx.doi.org/10.1103/PhysRevB.84.115446 URL ⟨http://link.aps.org/doi/10.1103/PhysRevB.84.115446⟩.
[64] W. Steurer, S. Surnev, A. Fortunelli, F.P. Netzer, Surf. Sci. 606 (910) (2012) 803–807, http://dx.doi.org/10.1016/j.susc.2012.01.012 URL ⟨http://www.sciencedirect.com/science/article/pii/S0039602812000283⟩.
[65] S.H. Phark, Y.J. Chang, T.W. Noh, J.-S. Kim, Phys. Rev. B 80 (2009) 035426, http://dx.doi.org/10.1103/PhysRevB.80.035426 URL ⟨http://link.aps.org/doi/10.1103/PhysRevB.80.035426⟩.
[66] A. Ouvrard, J. Niebauer, A. Ghalgaoui, C. Barth, C.R. Henry, B. Bourguignon, J. Phys. Chem. C 115 (16) (2011) 8034–8041, http://dx.doi.org/10.1021/jp1095823.
[67] S. Baumann, I.G. Rau, S. Loth, C.P. Lutz, A.J. Heinrich, ACS Nano 8 (2) (2014) 1739–1744, http://dx.doi.org/10.1021/nn4061034.
[68] L.R. Merte, M. Shipilin, S. Ataran, S. Blomberg, C. Zhang, A. Mikkelsen, J. Gustafson, E. Lundgren, J. Phys. Chem. C 119 (5) (2015) 2572–2582, http://dx.doi.org/10.1021/jp511496w.
[69] N.A. Khan, C. Matranga, Surf. Sci. 602 (4) (2008) 932–942, http://dx.doi.org/10.1016/j.susc.2007.12.027 URL ⟨http://www.sciencedirect.com/science/article/pii/S0039602807012216⟩.
[70] M. Li, E.I. Altman, J. Phys. Chem. C 118 (24) (2014) 12706–12716, http://dx.doi.org/10.1021/jp411375w.
[71] L.-Y. Ma, A. Picone, M. Wagner, S. Surnev, G. Barcaro, A. Fortunelli, F.P. Netzer, J. Phys. Chem. C 117 (36) (2013) 18464–18474, http://dx.doi.org/10.1021/jp4052424.
[72] M. Sambi, R. Sensolo, G. Rizzi, M. Petukhov, G. Granozzi, Surf. Sci. 537 (13) (2003) 36–54, http://dx.doi.org/10.1016/S0039-6028(03)00641-1 URL ⟨http://www.sciencedirect.com/science/article/pii/S0039602803006411⟩.
[73] F. Li, F. Allegretti, S. Surnev, F. Netzer, Y. Zhang, W.-B. Zhang, K. Reuter, Surf. Sci. 604 (1920) (2010) 1813–1819, http://dx.doi.org/10.1016/j.susc.2010.07.012 URL ⟨http://www.sciencedirect.com/science/article/pii/S0039602810002980⟩.
[74] B. Herd, M. Knapp, H. Over, J. Phys. Chem. C 116 (46) (2012) 24649–24660, http://dx.doi.org/10.1021/jp3085155.
[75] J. Gustafson, A. Resta, A. Mikkelsen, R. Westerström, J.N. Andersen, E. Lundgren, J. Weissenrieder, M. Schmid, P. Varga, N. Kasper, X. Torrelles, S. Ferrer, F. Mittendorfer, G. Kresse, Phys. Rev. B 74 (2006) 035401, http://dx.doi.org/10.1103/PhysRevB.74.035401 URL ⟨http://link.aps.org/doi/10.1103/PhysRevB.74.035401⟩.
[76] F. Li, F. Allegretti, S. Surnev, F.P. Netzer, Surf. Sci. 604 (1718) (2010) L43–L47, http://dx.doi.org/10.1016/j.susc.2010.05.017 URL ⟨http://www.sciencedirect.com/science/article/pii/S0039602810002190⟩.
[77] C. Franchini, F. Li, S. Surnev, R. Podloucky, F. Allegretti, F.P. Netzer, J. Phys.: Condens. Matter 24 (4) (2012) 042001 URL ⟨http://stacks.iop.org/0953-8984/24/i=4/a=042001⟩.
[78] J. Pal, M. Smerieri, E. Celasco, L. Savio, L. Vattuone, M. Rocca, Phys. Rev. Lett. 112 (2014) 126102, http://dx.doi.org/10.1103/PhysRevLett.112.126102 URL ⟨http://link.aps.org/doi/10.1103/PhysRevLett.112.126102⟩.
[79] J. Pal, M. Smerieri, E. Celasco, L. Savio, L. Vattuone, R. Ferrando, S. Tosoni, L. Giordano, G. Pacchioni, M. Rocca, J. Phys. Chem. C 118 (45) (2014) 26091–26102, http://dx.doi.org/10.1021/jp507718n URL ⟨http://dx.doi.org/10.1021/jp507718n⟩.
[80] I. Palacio, M. Monti, J.F. Marco, K.F. McCarty, J. de la Figuera, J. Phys.: Condens. Matter 25 (48) (2013) 484001 URL ⟨http://stacks.iop.org/0953-8984/25/i=48/a=484001⟩.
[81] L. Vitos, A. Ruban, H. Skriver, J. Kollar, Surf. Sci. 411 (12) (1998) 186–202, http://dx.doi.org/10.1016/S0039-6028(98)00363-X URL ⟨http://www.sciencedirect.com/science/article/pii/S003960289800363X⟩.
[82] B.S. Youmbi, F. Calvayrac, Surf. Sci. 621 (2014) 1–6 http://dx.doi.org/10.1016/j.susc.2013.10.012 URL ⟨http://www.sciencedirect.com/science/article/pii/S0039602813003087⟩.
[83] D. Santos-Carballal, A. Roldan, R. Grau-Crespo, N.H. de Leeuw, Phys. Chem. Chem. Phys. 16 (2014) 21082–21097, http://dx.doi.org/10.1039/C4CP00529E.
[84] S.R. Lu, R. Yu, J. Zhu, Phys. Rev. B 87 (2013) 165436 http://dx.doi.org/10.1103/PhysRevB.87.165436 URL ⟨http://link.aps.org/doi/10.1103/PhysRevB.87.165436⟩.
[85] D. Wolf, Phys. Rev. Lett. 68 (1992) 3315–3318, http://dx.doi.org/10.1103/PhysRevLett.68.3315 URL ⟨http://link.aps.org/doi/ 10.1103/PhysRevLett.68.3315⟩.
[86] W. Mackrodt, Phys. Chem. Miner. 15 (3) (1988) 228–237, http://dx.doi.org/10.1007/BF00307511.
[87] C. Rehbein, N.M. Harrison, A. Wander, Phys. Rev. B 54 (1996) 14066–14070, http://dx.doi.org/10.1103/PhysRevB.54.14066 URL ⟨http://link.aps.org/doi/10.1103/PhysRevB.54.14066⟩.
[88] S.A. Chambers, T. Droubay, D.R. Jennison, T.R. Mattsson, Science 297 (5582) (2002) 827–831, http://dx.doi.org/10.1126/science.1073404 URL ⟨http://www.sciencemag.org/content/297/5582/827.abstract⟩.
[89] J.F. Sanz, N.C. Hernández, Phys. Rev. Lett. 94 (2005) 016104, http://dx.doi.org/10.1103/PhysRevLett.94.016104 URL ⟨http://link.aps.org/doi/10.1103/PhysRevLett.94.016104⟩.
[90] Q. Fu, T. Wagner, Surf. Sci 505 (2002) 39–48, http://dx.doi.org/10.1016/S0039-6028(02)01392-4 URL ⟨http://www.sciencedirect.com/science/article/pii/S0039602802013924⟩.
[91] X. Shao, N. Nilius, H.-J. Freund, Phys. Rev. B 85 (2012) 115444, http://dx.doi.org/10.1103/PhysRevB.85.115444 URL ⟨http://link.aps.org/doi/10.1103/PhysRevB.85.115444⟩.
[92] D. Ricci, A. Bongiorno, G. Pacchioni, U. Landman, Phys. Rev. Lett. 97 (2006) 036106, http://dx.doi.org/10.1103/PhysRevLett.97.036106 URL ⟨http://link.aps.org/doi/10.1103/PhysRevLett.97.036106⟩.
[93] M. Sterrer, T. Risse, M. Heyde, H.-P. Rust, H.-J. Freund, Phys. Rev. Lett. 98 (2007) 206103, http://dx.doi.org/10.1103/PhysRevLett.98.206103 URL ⟨http://link.aps.org/doi/10.1103/PhysRevLett.98.206103⟩.
[94] W. Jauch, M. Reehuis, H.J. Bleif, F. Kubanek, P. Pattison, Phys. Rev. B 64 (2001) 052102, http://dx.doi.org/10.1103/PhysRevB.64.052102.
[95] W.L. Smith, A.D. Hobson, Acta Crystallogr. Sect. B 29 (2) (1973) 362–363, http://dx.doi.org/10.1107/S0567740873002505 URL ⟨http://dx.doi.org/10.1107/S0567740873002505⟩.
[96] L.C. Bartel, B. Morosin, Phys. Rev. B 3 (1971) 1039–1043, http://dx.doi.org/10.1103/PhysRevB.3.1039.
[97] P. Kaercher, S. Speziale, L. Miyagi, W. Kanitpanyacharoen, H.-R. Wenk, Phys. Chem. Miner. 39 (8) (2012) 613–626, http://dx.doi.org/ 10.1007/s00269-012-0516-x.
[98] E. Nazarenko, J.E. Lorenzo, Y. Joly, J.L. Hodeau, D. Mannix, C. Marin, Phys. Rev. Lett. 97 (2006) 056403, http://dx.doi.org/10.1103/PhysRevLett.97.056403.
[99] K. Doll, M. Dolg, H. Stoll, Phys. Rev. B 54 (1996) 13529–13535 http://dx.doi.org/10.1103/PhysRevB.54.13529 URL ⟨http://link.aps.org/doi/10.1103/PhysRevB.54.13529⟩.
[100] F.W. Lytle, J. Appl. Phys. 35 (7) (1964) 2212–2215, http://dx.doi.org/10.1063/1.1702820.

[101] G. Renaud, P. Guénard, A. Barbier, Phys. Rev. B 58 (1998) 7310–7318, http://dx.doi.org/10.1103/PhysRevB.58.7310 URL ⟨http://link.aps.org/doi/10.1103/PhysRevB.58.7310⟩.
[102] P. Torelli, E. Soares, G. Renaud, S. Valeri, X. Guo, P. Luches, Surf. Sci. 601 (13) (2007) 2651–2655, http://dx.doi.org/10.1016/j.susc.2006.11.063 URL ⟨http://www.sciencedirect.com/science/article/pii/S0039602806012532⟩.
[103] S. Benedetti, P. Torelli, S. Valeri, H.M. Benia, N. Nilius, G. Renaud, Phys. Rev. B 78 (2008) 195411, http://dx.doi.org/10.1103/PhysRevB.78.195411 URL ⟨http://link.aps.org/doi/10.1103/PhysRevB.78.195411⟩.
[104] F.P. Netzer, Surf. Rev. Lett. 09 (03n04) (2002) 1553–1563 http://dx.doi.org/10.1142/S0218625X02003950 URL ⟨http://www.worldscientific.com/doi/abs/10.1142/S0218625X02003950⟩.
[105] S. Agnoli, M. Sambi, G. Granozzi, A. Atrei, M. Caffio, G. Rovida, Surf. Sci. 576 (13) (2005) 1–8, http://dx.doi.org/10.1016/j.susc.2004.11.032 URL ⟨http://www.sciencedirect.com/science/article/pii/S003960280401516X⟩.
[106] C. Franchini, R. Podloucky, F. Allegretti, F. Li, G. Parteder, S. Surnev, F.P. Netzer, Phys. Rev. B 79 (2009) 035420, http://dx.doi.org/10.1103/PhysRevB.79.035420 URL ⟨http://link.aps.org/doi/10.1103/PhysRevB.79.035420⟩.
[107] F. Allegretti, G. Parteder, L. Gragnaniello, S. Surnev, F. Netzer, A. Barolo, S. Agnoli, G. Granozzi, C. Franchini, R. Podloucky, Surf. Sci. 604 (56) (2010) 529–534, http://dx.doi.org/10.1016/j.susc.2009.12.018 URL ⟨http://www.sciencedirect.com/science/article/pii/S003960280900795X⟩.
[108] X. Shao, P. Myrach, N. Nilius, H.-J. Freund, J. Phys. Chem. C 115 (17) (2011) 8784–8789, http://dx.doi.org/10.1021/jp201852x.
[109] X. Shao, N. Nilius, P. Myrach, H.-J. Freund, U. Martinez, S. Prada, L. Giordano, G. Pacchioni, Phys. Rev. B 83 (2011) 245407, http://dx.doi.org/10.1103/PhysRevB.83.245407 URL ⟨http://link.aps.org/doi/10.1103/PhysRevB.83.245407⟩.
[110] S. Shaikhutdinov, M. Ritter, W. Weiss, Phys. Rev. B 62 (2000) 7535–7541, http://dx.doi.org/10.1103/PhysRevB.62.7535 URL ⟨http://link.aps.org/doi/10.1103/PhysRevB.62.7535⟩.
[111] D. Bruns, I. Kiesel, S. Jentsch, S. Lindemann, C. Otte, T. Schemme, T. Kuschel, J. Wollschlger, J. Phys.: Condens. Matter 26 (31) (2014) 315001 URL ⟨http://stacks.iop.org/0953-8984/26/i=31/a=315001⟩. K.
[112] Biedermann, M. Gubo, L. Hammer, K. Heinz, J. Phys.: Condens. Matter 21 (18) (2009) 185003 URL ⟨http://stacks.iop.org/0953-8984/21/i=18/a=185003⟩.
[113] C. Tröppner, T. Schmitt, M. Reuschl, L. Hammer, M.A. Schneider, F. Mittendorfer, J. Redinger, R. Podloucky, M. Weinert, Phys. Rev. B 86 (2012) 235407, http://dx.doi.org/10.1103/PhysRevB.86.235407 URL ⟨http://link.aps.org/doi/10.1103/PhysRevB.86.235407⟩.
[114] F. Li, G. Parteder, F. Allegretti, C. Franchini, R. Podloucky, S. Surnev, F.P. Netzer, J. Phys.: Condens. Matter 21 (13) (2009) 134008 URL ⟨http://stacks.iop.org/0953-8984/21/i=13/a=134008⟩. Y.
[115] Pan, S. Benedetti, N. Nilius, H.-J. Freund, Phys. Rev. B 84 (2011) 075456, http://dx.doi.org/10.1103/PhysRevB.84.075456 URL ⟨http://link.aps.org/doi/10.1103/PhysRevB.84.075456⟩.
[116] M. Gubo, C. Ebensperger, W. Meyer, L. Hammer, K. Heinz, F. Mittendorfer, J. Redinger, Phys. Rev. Lett. 108 (2012) 066101, http://dx.doi.org/10.1103/PhysRevLett.108.066101 URL ⟨http://link.aps.org/doi/10.1103/PhysRevLett.108.066101⟩.
[117] E.M. Davis, K. Zhang, Y. Cui, H. Kuhlenbeck, S. Shaikhutdinov, H.-J. Freund, Surf. Sci. 636 (2015) 42–46, http://dx.doi.org/10.1016/j.susc.2015.02.004 URL ⟨http://www.sciencedirect.com/science/article/pii/S0039602815000394⟩.
[118] N. Spiridis, J. Barbasz, Z. Łodziana, J. Korecki, Phys. Rev. B 74 (2006) 155423, http://dx.doi.org/10.1103/PhysRevB.74.155423 URL ⟨http://link.aps.org/doi/10.1103/PhysRevB.74.155423⟩.
[119] R.T. Tung, Appl. Phys. Rev. 1 (1) (2014) 011304, http://dx.doi.org/10.1063/1.4858400 URL ⟨http://scitation.aip.org/content/aip/journal/apr2/1/1/10.1063/1.4858400⟩.
[120] H. Stöcker, M. Zschornak, J. Seibt, F. Hanzig, S. Wintz, B. Abendroth,
J. Kortus, D. Meyer, Appl. Phys. A 100 (2) (2010) 437–445, http://dx.doi.org/10.1007/s00339-010-5848-0 URL ⟨http://dx.doi.org/10. 1007/s00339-010-5848-0⟩.
[121] S.A. Chambers, M. Gu, P.V. Sushko, H. Yang, C. Wang, N. D. Browning, Adv. Mater. 25 (29) (2013) 4001–4005, http://dx.doi.org/10.1002/adma.201301030 URL ⟨http://dx.doi.org/10. 1002/adma.201301030⟩.
[122] C. Capan, G.Y. Sun, M.E. Bowden, S.A. Chambers, Appl. Phys. Lett. 100 (5) (2012) 052106, http://dx.doi.org/10.1063/1.3680608 URL ⟨http://scitation.aip.org/content/aip/journal/apl/100/5/10.1063/1.3680608⟩.
[123] C. Lenser, A. Köhl, M. Patt, C.M. Schneider, R. Waser, R. Dittmann, Phys. Rev. B 90 (2014) 115312, http://dx.doi.org/10.1103/PhysRevB.90.115312 URL ⟨http://link.aps.org/doi/10.1103/PhysRevB.90.115312⟩.
[124] T. Jaouen, G. Jézéquel, G. Delhaye, B. Lépine, P. Turban, P. Schieffer, Appl. Phys. Lett. 97 (23) (2010) 232104, http://dx.doi.org/10.1063/1.3525159 URL ⟨http://scitation.aip.org/content/aip/journal/apl/97/23/10.1063/1.3525159⟩.
[125] T. Jaouen, G. Jézéquel, G. Delhaye, B. Lépine, P. Turban, P. Schieffer, Appl. Phys. Lett. 100 (2) (2012) 022103, http://dx.doi.org/10.1063/1.3675859 URL ⟨http://scitation.aip.org/content/aip/journal/apl/100/2/10.1063/1.3675859⟩.
[126] T. Jaouen, P. Aebi, S. Tricot, G. Delhaye, B. Lépine, D. Sébilleau, G. Jézéquel, P. Schieffer, Phys. Rev. B 90 (2014) 125433, http://dx.doi.org/10.1103/PhysRevB.90.125433 URL ⟨http://link.aps.org/doi/10.1103/PhysRevB.90.125433⟩.
[127] M. Yoshitake, S. Nemšák, T. Skála, N. Tsud, T. Kim, V. Matolín, K. C. Prince, Surf. Sci. 604 (2324) (2010) 2150–2156, http://dx.doi.org/10.1016/j.susc.2010.09.007 URL ⟨http://www.sciencedirect.com/science/article/pii/S0039602810003833⟩.
[128] M. Yoshitake, W. Song, J. Libra, K. Mašek, F. Šutara, V. Matolín, K. C. Prince, J. Appl. Phys. 103 (3) (2008) 033707, http://dx.doi.org/10.1063/1.2837116 URL ⟨http://scitation.aip.org/content/aip/journal/jap/103/3/10.1063/1.2837116⟩.
[129] A. Morosov, A. Sigov, Phys. Solid State 54 (2) (2012) 219–242, http://dx.doi.org/10.1134/S1063783412020187 URL ⟨http://dx.doi.org/10.1134/S1063783412020187⟩.
[130] J. Velev, P. Dowben, E. Tsymbal, S. Jenkins, A. Caruso, Surf. Sci. Rep. 63 (9) (2008) 400–425, http://dx.doi.org/10.1016/j.surfrep.2008.06.002 URL ⟨http://www.sciencedirect.com/science/article/pii/S0167572908000514⟩.
[131] E. Fawcett, Rev. Mod. Phys. 60 (1988) 209–283, http://dx.doi.org/ 10.1103/RevModPhys.60.209 URL ⟨http://link.aps.org/doi/10.1103/Rev ModPhys.60.209⟩.
[132] P.J. Brown, J.B. Forsyth, E. Lelivre-Berna, F. Tasset, J. Phys.: Condens. Matter 14 (8) (2002) 1957 URL ⟨http://stacks.iop.org/0953-8984/14/i=8/a=323⟩.
[133] D.J. Huang, H.-T. Jeng, C.F. Chang, G.Y. Guo, J. Chen, W.P. Wu, S. C. Chung, S.G. Shyu, C.C. Wu, H.-J. Lin, C.T. Chen, Phys. Rev. B 66 (2002) 174440, http://dx.doi.org/10.1103/PhysRevB.66.174440 URL ⟨http://link.aps.org/doi/10.1103/PhysRevB.66.174440⟩.
[134] O. Eriksson, A.M. Boring, R.C. Albers, G.W. Fernando, B.R. Cooper, Phys. Rev. B 45 (1992) 2868–2875, http://dx.doi.org/10.1103/PhysRevB.45.2868 URL ⟨http://link.aps.org/doi/10.1103/PhysRevB.45.2868⟩.
[135] W.L. Roth, Phys. Rev. 110 (1958) 1333–1341, http://dx.doi.org/10.1103/PhysRev.110.1333 URL ⟨http://link.aps.org/doi/10.1103/PhysRev.110.1333⟩.
[136] Z. Zhang, S. Satpathy, Phys. Rev. B 44 (1991) 13319–13331, http://dx.doi.org/10.1103/PhysRevB.44.13319 URL ⟨http://link.aps.org/doi/ 10.1103/PhysRevB.44.13319⟩.
[137] D.J. Huang, C.F. Chang, H.-T. Jeng, G.Y. Guo, H.-J. Lin, W.B. Wu, H. C. Ku, A. Fujimori, Y. Takahashi, C.T. Chen, Phys. Rev. Lett. 93 (2004) 077204, http://dx.doi.org/10.1103/PhysRevLett.93.077204 URL ⟨http://link.aps.org/doi/10.1103/PhysRevLett.93.077204⟩.
[138] A.K. Cheetham, D.A.O. Hope, Phys. Rev. B 27 (1983) 6964–6967, http://dx.doi.org/10.1103/PhysRevB.27.6964 URL ⟨http://link.aps.org/doi/10.1103/PhysRevB.27.6964⟩.
[139] P. Luches, L. Pasquini, S. Benedetti, V. Bellini, S. Valeri, F. Manghi, R. Rüffer, F. Boscherini, Phys. Rev. B 83 (2011) 094413, http://dx.doi.org/10.1103/PhysRevB.83.094413 URL ⟨http://link.aps.org/doi/10.1103/PhysRevB.83.094413⟩.
[140] W.H. Meiklejohn, C.P. Bean, Phys. Rev. 102 (1956) 1413–1414, http://dx.doi.org/10.1103/PhysRev.102.1413 URL ⟨http://link.aps.org/doi/10.1103/PhysRev.102.1413⟩.

[141] M. Finazzi, Phys. Rev. B 69 (2004) 064405, http://dx.doi.org/10.1103/PhysRevB.69.064405 URL ⟨http://link.aps.org/doi/10.1103/PhysRevB.69.064405⟩.
[142] H. Ohldag, T.J. Regan, J. Stöhr, A. Scholl, F. Nolting, J. Lüning, C. Stamm, S. Anders, R.L. White, Phys. Rev. Lett. 87 (2001) 247201, http://dx.doi.org/10.1103/PhysRevLett.87.247201 URL ⟨http://link.aps.org/doi/10.1103/PhysRevLett.87.247201⟩.
[143] E. Mlyńczak, J. Gurgul, J. Przewoźnik, D. Wilgocka-Ślzak, K. Freindl, N. Spiridis, J. Korecki, Appl. Surf. Sci. 304 (2014) 86–90, http://dx.doi.org/10.1016/j.apsusc.2014.01.167 URL ⟨http://www.sciencedirect.com/science/article/pii/S0169433214002190⟩.
[144] Y. Fan, K.J. Smith, G. Luepke, A.T. Hanbicki, R. Goswami, C.H. Li, H. B. Zhao, B.T. Jonker, Nat. Nanotechnol. 8 (6) (2013) 438–444, http://dx.doi.org/10.1038/NNANO.2013.94.
[145] F. Allegretti, G. Parteder, M. Ramsey, S. Surnev, F. Netzer, Surf. Sci. 601 (14) (2007) L73–L76, http://dx.doi.org/10.1016/j.susc.2007.05.008 URL ⟨http://www.sciencedirect.com/science/article/pii/S0039602807005560⟩.
[146] R. de Masi, D. Reinicke, F. Müller, P. Steiner, S. Hüfner, Surf. Sci. 516 (12) (2002) L515–L521, http://dx.doi.org/10.1016/S0039-6028(02)01906-4 URL ⟨http://www.sciencedirect.com/science/article/pii/S0039602802019064⟩.
[147] M. Bäumer, D. Cappus, H. Kuhlenbeck, H.-J. Freund, G. Wilhelmi, A. Brodde, H. Neddermeyer, Surf. Sci. 253 (13) (1991) 116–128, http://dx.doi.org/10.1016/0039-6028(91)90585-G URL ⟨http://www.sciencedirect.com/science/article/pii/003960289190585G⟩.
[148] G. Bussetti, M. Riva, A. Picone, A. Brambilla, L. Duò, M. Finazzi, F. Ciccacci, New J. Phys. 14 (5) (2012) 053048 URL ⟨http://stacks.iop.org/1367-2630/14/i=5/a=053048⟩.
[149] A.V. Mijiritskii, P.J.M. Smulders, V.Y. Chumanov, O.C. Rogojanu, M. A. James, D.O. Boerma, Phys. Rev. B 58 (1998) 8960–8966, http://dx.doi.org/10.1103/PhysRevB.58.8960 URL ⟨http://link.aps.org/doi/10.1103/PhysRevB.58.8960⟩.
[150] G. Bussetti, M. Riva, A. Picone, A. Brambilla, L. Duò, F. Ciccacci, M. Finazzi, Nanosci. Nanotechnol. Lett. 4 (11) (2012) 1092–1095, http://dx.doi.org/10.1166/nnl.2012.1463.
[151] S.K. Kim, C. Petersen, F. Jona, P.M. Marcus, Phys. Rev. B 54 (1996) 2184–2190, http://dx.doi.org/10.1103/PhysRevB.54.2184 URL ⟨http://link.aps.org/doi/10.1103/PhysRevB.54.2184⟩.
[152] L. Duò, R. Bertacco, G. Isella, F. Ciccacci, M. Richter, Phys. Rev. B 61 (2000) 15294–15301, http://dx.doi.org/10.1103/PhysRevB.61.15294 URL ⟨http://link.aps.org/doi/10.1103/PhysRevB.61.15294⟩.
[153] A. Picone, M. Riva, G. Fratesi, A. Brambilla, G. Bussetti, M. Finazzi, L. Duò, F. Ciccacci, Phys. Rev. Lett. 113 (2014) 046102, http://dx.doi.org/10.1103/PhysRevLett.113.046102 URL ⟨http://link.aps.org/doi/10.1103/PhysRevLett.113.046102⟩.
[154] S. Valeri, A. Borghi, G. Gazzadi, A. di Bona, Surf. Sci. 423 (23) (1999) 346–356.
[155] G. Gazzadi, A. Borghi, A. di Bona, S. Valeri, Surf. Sci. 402–404 (1998) 632–635, http://dx.doi.org/10.1016/S0039-6028(97)00920-5 URL ⟨http://www.sciencedirect.com/science/article/pii/S0039602897009205⟩.
[156] O. Dugerjav, H. Kim, J.M. Seo, AIP Adv. 1 (3) (2011) 032156, http://dx.doi.org/10.1063/1.3642601 URL ⟨http://scitation.aip.org/content/aip/journal/adva/1/3/10.1063/1.3642601⟩.
[157] J.C. Read, P.G. Mather, R.A. Buhrman, Appl. Phys. Lett. 90 (13) (2007) 132503, http://dx.doi.org/10.1063/1.2717091 URL ⟨http://scitation.aip.org/content/aip/journal/apl/90/13/10.1063/1.2717091⟩.
[158] M. Xue, Q. Guo, J. Alloys Compd. 598 (2014) 224–229, http://dx.doi.org/10.1016/j.jallcom.2014.02.023 URL ⟨http://www.sciencedirect.com/science/article/pii/S092583881400351X⟩.
[159] M. Xue, Q. Guo, K. Wu, J. Guo, J. Cryst. Growth 311 (15) (2009) 3918–3923, http://dx.doi.org/10.1016/j.jcrysgro.2009.06.001 URL ⟨http://www.sciencedirect.com/science/article/pii/S0022024809005776⟩.
[160] M. Kamiko, R. Yamamoto, J. Cryst. Growth 293 (1) (2006) 216–222, http://dx.doi.org/10.1016/j.jcrysgro.2006.05.009 URL ⟨http://www.sciencedirect.com/science/article/pii/S0022024806004933⟩.
[161] T. Nozaki, T. Ohkubo, Y. Shiota, H. Kubota, A. Fukushima, K. Hono, Y. Suzuki, S. Yuasa, Appl. Phys. Express 6 (11) (2013) 113004 URL ⟨http://stacks.iop.org/1882-0786/6/i=11/a=113004⟩.
[162] T. Nozaki, H. Kubota, A. Fukushima, S. Yuasa, Appl. Phys. Lett. 106 (2) (2015) 022405, http://dx.doi.org/10.1063/1.4905927 URL ⟨http://scitation.aip.org/content/aip/journal/apl/106/2/10.1063/1.4905927⟩.
[163] P. Torelli, S. Benedetti, P. Luches, L. Gragnaniello, J. Fujii, S. Valeri, Phys. Rev. B 79 (2009) 035408, http://dx.doi.org/10.1103/PhysRevB.79.035408 URL ⟨http://link.aps.org/doi/10.1103/PhysRevB.79.035408⟩.
[164] S. Altieri, S.F. Contri, S. Valeri, Phys. Rev. B 76 (2007) 205413, http://dx.doi.org/10.1103/PhysRevB.76.205413 URL ⟨http://link.aps.org/doi/10.1103/PhysRevB.76.205413⟩.
[165] J. Jung, H.-J. Shin, Y. Kim, M. Kawai, Phys. Rev. B 82 (2010) 085413, http://dx.doi.org/10.1103/PhysRevB.82.085413 URL ⟨http://link.aps.org/doi/10.1103/PhysRevB.82.085413⟩.
[166] L. Savio, E. Celasco, L. Vattuone, M. Rocca, J. Phys. Chem. B 108 (23) (2004) 7771–7778, http://dx.doi.org/10.1021/jp0360873.
[167] L. Savio, E. Celasco, L. Vattuone, M. Rocca, J. Chem. Phys. 119 (23) (2003) 12053–12056, http://dx.doi.org/10.1063/1.1633751 URL ⟨http://scitation.aip.org/content/aip/journal/jcp/119/23/10.1063/1.1633751⟩.
[168] Y.-N. Sun, Z.-H. Qin, M. Lewandowski, E. Carrasco, M. Sterrer, S. Shaikhutdinov, H.-J. Freund, J. Catal. 266 (2) (2009) 359–368, http://dx.doi.org/10.1016/j.jcat.2009.07.002 URL ⟨http://www.sciencedirect.com/science/article/pii/S0021951709002255⟩.
[169] F. Ringleb, Y. Fujimori, M.A. Brown, W.E. Kaden, F. Calaza, H. Kuhlenbeck, M. Sterrer, H.-J. Freund, Catal. Today 240, Part B (2015) 206–213, http://dx.doi.org/10.1016/j.cattod.2014.04.025, URL ⟨http://www.sciencedirect.com/science/article/pii/S0920586114003514⟩.
[170] N. Nilius, Surf. Sci. Rep. 64 (12) (2009) 595–659, http://dx.doi.org/10.1016/j.surfrep.2009.07.004 URL ⟨http://www.sciencedirect.com/science/article/pii/S0167572909000491⟩.
[171] M. Sierka, Prog. Surf. Sci. 85 (912) (2010) 398–434 http://dx.doi.org/10.1016/j.progsurf.2010.07.004 URL ⟨http://www.sciencedirect.com/science/article/pii/S0079681610000237⟩.
[172] A. Brambilla, A. Picone, M. Finazzi, L. Duò, F. Ciccacci, Surf. Sci. 605 (12) (2011) 95–100, http://dx.doi.org/10.1016/j.susc.2010.10.005 URL ⟨http://www.sciencedirect.com/science/article/pii/S0039602810004024⟩.
[173] S. Ekelund, C. Leygraf, Surf. Sci. 40 (1) (1973) 179–199, http://dx.doi.org/10.1016/0039-6028(73)90061-7 URL ⟨http://www.sciencedirect.com/science/article/pii/0039602873900617⟩.
[174] A. Stierle, P. Bdeker, H. Zabel, Surf. Sci. 327 (12) (1995) 9–16, http://dx.doi.org/10.1016/0039-6028(94)00830-2 URL ⟨http://www.sciencedirect.com/science/article/pii/0039602894008302⟩.
[175] M. Müller, H. Oechsner, Surf. Sci. 387 (13) (1997) 269–278, http://dx.doi.org/10.1016/S0039-6028(97)00363-4 URL ⟨http://www.sciencedirect.com/science/article/pii/S0039602897003634⟩.
[176] A. Stierle, T. Koll, H. Zabel, Phys. Rev. B 58 (1998) 5062–5069, http://dx.doi.org/10.1103/PhysRevB.58.5062 URL ⟨http://link.aps.org/doi/10.1103/PhysRevB.58.5062⟩.
[177] V. Maurice, S. Cadot, P. Marcus, Surf. Sci. 458 (13) (2000) 195–215, http://dx.doi.org/10.1016/S0039-6028(00)00439-8 URL ⟨http://www.sciencedirect.com/science/article/pii/S0039602800004398⟩.
[178] H. Hagiwara, S. Koya, M. Wilde, M. Matsumoto, T. Okano, K. Fukutani, Surf. Sci. 600 (16) (2006) 3252–3257, http://dx.doi.org/10.1016/j.susc.2006.06.013 URL ⟨http://www.sciencedirect.com/science/article/pii/S0039602806007023⟩.
[179] P. Michel, C. Jardin, Surf. Sci. 36 (2) (1973) 478–487, http://dx.doi.org/10.1016/0039-6028(73)90396-8 URL ⟨http://www.sciencedirect.com/science/article/pii/0039602873903968⟩.
[180] M. Bridge, R. Lambert, Surf. Sci. 82 (2) (1979) 413–424, http://dx.doi.org/10.1016/0039-6028(79)90199-7 URL ⟨http://www.sciencedirect.com/science/article/pii/0039602879901997⟩.
[181] S. Nemšák, T. Skála, M. Yoshitake, K.C. Prince, V. Matolín, J. Phys.: Condens. Matter 25 (9) (2013) 095004 URL ⟨http://stacks.iop.org/0953-8984/25/i=9/a=095004⟩.
[182] X. Chen, H. Kazi, Y. Cao, B. Dong, F.L. Pasquale, J.A.C. Santana, S. Cao, M. Street, R. Welch, C. Binek, A. Enders, J.A. Kelber, P. Dowben, Mater. Chem. Phys. 149–150 (2015) 113–123, http://dx.doi.org/10.1016/j.matchemphys.2014.09.053 URL ⟨http://www.sciencedirect.com/science/article/pii/S025405841400635X⟩.

[183] Y.-Z. Wang, M. Yang, D.-C. QI, S. Chen, W. Chen, A.T.S. Wee, X.-Y. Gao, J. Chem. Phys. 134 (3) (2011) 034706 10.1063/1.3546034 URL ⟨http://scitation.aip.org/content/aip/journal/jcp/134/3/10.1063/1.3546034⟩.
[184] J.I. Flege, A. Meyer, J. Falta, E.E. Krasovskii, Phys. Rev. B 84 (2011) 115441, http://dx.doi.org/10.1103/PhysRevB.84.115441 URL ⟨http://link.aps.org/doi/10.1103/PhysRevB.84.115441⟩.
[185] D.F. Forster, J. Klinkhammer, C. Busse, S.G. Altendorf, T. Michely, Z. Hu, Y.-Y. Chin, L.H. Tjeng, J. Coraux, D. Bourgault, Phys. Rev. B 83 (2011) 045424, http://dx.doi.org/10.1103/PhysRevB.83.045424 URL ⟨http://link.aps.org/doi/10.1103/PhysRevB.83.045424⟩.
[186] D.F. Förster, J. Klinkhammer, T. Michely, Surf. Sci. 606 (1314) (2012) 1019–1028, http://dx.doi.org/10.1016/j.susc.2012.02.021 URL ⟨http://www.sciencedirect.com/science/article/pii/S0039602812000726⟩.
[187] S.L. Pévédic, D. Schmaus, C. Cohen, Surf. Sci. 602 (1) (2008) 67–76, http://dx.doi.org/10.1016/j.susc.2007.09.050 URL ⟨http://www.sciencedirect.com/science/article/pii/S0039602807009752⟩.
[188] S. Nemsak, T. Skala, M. Yoshitake, N. Tsud, T. Kim, S. Yagyu, V. Matolin, Surf. Interface Anal. 42 (10–11) (2010) 1581–1584 http://dx.doi.org/10.1002/sia.3582.
[189] G. Prévot, S. Le Moal, R. Bernard, B. Croset, R. Lazzari, D. Schmaus, Phys. Rev. B 85 (2012) 205450, http://dx.doi.org/10.1103/PhysRevB.85.205450 URL ⟨http://link.aps.org/doi/10.1103/PhysRevB.85.205450⟩.
[190] A.C. Papageorgiou, G. Cabailh, Q. Chen, A. Resta, E. Lundgren, J. N. Andersen, G. Thornton, J. Phys. Chem. C 111 (21) (2007) 7704–7710, http://dx.doi.org/10.1021/jp067802m.
[191] K. Kishi, K. Fujiwara, J. Electron Spectrosc. Relat. Phenom. 85 (12) (1997) 123–134, http://dx.doi.org/10.1016/S0368-2048(96)03093-9 URL ⟨http://www.sciencedirect.com/science/article/pii/S0368204896030939⟩.
[192] R.I.R. Blyth, C. Searle, N.P. Tucker, S.D. Barrett, Phys. Rev. B 70 (2004) 045402, http://dx.doi.org/10.1103/PhysRevB.70.045402 URL ⟨http://link.aps.org/doi/10.1103/PhysRevB.70.045402⟩.
[193] C. Gu, C.G. Olson, D.W. Lynch, Phys. Rev. B 48 (1993) 12178–12182, http://dx.doi.org/10.1103/PhysRevB.48.12178 URL ⟨http://link.aps.org/doi/10.1103/PhysRevB.48.12178⟩.
[194] D. Riffe, G. Wertheim, Surf. Sci. 399 (23) (1998) 248–263 http://dx.doi.org/10.1016/S0039-6028(97)00824-8 URL ⟨http://www.sciencedirect.com/science/article/pii/S0039602897008248⟩.
[195] P. Nordlander, M. Ronay, Phys. Rev. B 36 (1987) 4982–4989, http://dx.doi.org/10.1103/PhysRevB.36.4982 URL ⟨http://link.aps.org/doi/10.1103/PhysRevB.36.4982⟩.
[196] M. Ronay, P. Nordlander, Phys. Rev. B 35 (1987) 9403–9406 http://dx.doi.org/10.1103/PhysRevB.35.9403 URL ⟨http://link.aps.org/doi/10.1103/PhysRevB.35.9403⟩.
[197] K. Radican, S. Bozhko, S.-R. Vadapoo, S. Ulucan, H.-C. Wu, A. McCoy, I. Shvets, Surf. Sci. 604 (1920) (2010) 1548–1551, http://dx.doi.org/10.1016/j.susc.2010.05.016 URL ⟨http://www.sciencedirect.com/science/article/pii/S0039602810002189⟩.
[198] K. Radican, N. Berdunov, G. Manai, I.V. Shvets, Phys. Rev. B 75 (2007) 155434, http://dx.doi.org/10.1103/PhysRevB.75.155434 URL ⟨http://link.aps.org/doi/10.1103/PhysRevB.75.155434⟩.
[199] M. Gallagher, M. Fyfield, J. Cowin, S. Joyce, Surf. Sci. 339 (3) (1995) L909–L913, http://dx.doi.org/10.1016/0039-6028(95)80056-5 URL ⟨http://www.sciencedirect.com/science/article/pii/0039602895800565⟩.
[200] M. Gallagher, M. Fyfield, L. Bumm, J. Cowin, S. Joyce, Thin Solid Films 445 (1) (2003) 90–95, http://dx.doi.org/10.1016/j.tsf.2003.09.016 URL ⟨http://www.sciencedirect.com/science/article/pii/S0040609003012872⟩.
[201] H. Benia, P. Myrach, N. Nilius, H.-J. Freund, Surf. Sci. 604 (34) (2010) 435–441, http://dx.doi.org/10.1016/j.susc.2009.12.011 URL ⟨http://www.sciencedirect.com/science/article/pii/S0039602809007754⟩.
[202] Q. Guo, W. Oh, D. Goodman, Surf. Sci. 437 (12) (1999) 49–60, http://dx.doi.org/10.1016/S0039-6028(99)00678-0 URL ⟨http://www.sciencedirect.com/science/article/pii/S0039602899006780⟩.
[203] C.L. Pang, D.C. Grinter, J. Matharu, G. Thornton, J. Phys. Chem. C 117 (48) (2013) 25622–25627, http://dx.doi.org/10.1021/jp409948u.
[204] J. Matharu, G. Cabailh, G. Thornton, Surf. Sci. 616 (2013) 198–205, http://dx.doi.org/10.1016/j.susc.2013.05.020 URL ⟨http://www.sciencedirect.com/science/article/pii/S0039602813001726⟩.
[205] Y. Law, T. Dintzer, S. Zafeiratos, Appl. Surf. Sci. 258 (4) (2011) 1480–1487, http://dx.doi.org/10.1016/j.apsusc.2011.09.111 URL ⟨http://www.sciencedirect.com/science/article/pii/S0169433211015145⟩.
[206] A.M. Silva, C. Achete, R.B. Capaz, Chem. Phys. 410 (2013) 99–102, http://dx.doi.org/10.1016/j.chemphys.2012.11.004 URL ⟨http://www.sciencedirect.com/science/article/pii/S0301010412004326⟩.
[207] S. Zafeiratos, S. Piccinin, D. Teschner, Catal. Sci. Technol. 2 (2012) 1787–1801, http://dx.doi.org/10.1039/C2CY00487A.
[208] M. Antlanger, W. Mayr-Schmölzer, J.C.V. Pavelec, F. Mittendorfer, J. Redinger, P. Varga, U. Diebold, M. Schmid, Phys. Rev. B 86 (2012) 035451, http://dx.doi.org/10.1103/PhysRevB.86.035451 URL ⟨http://link.aps.org/doi/10.1103/PhysRevB.86.035451⟩.
[209] J.I.J. Choi, W. Mayr-Schmölzer, F. Mittendorfer, J. Redinger, U. Diebold, M. Schmid, J. Phys.: Condens. Matter 26 (22) (2014) 225003 URL ⟨http://stacks.iop.org/0953-8984/26/i=22/a=225003⟩. D.
[210] Flötotto, Z. Wang, E. Mittemeijer, Surf. Sci. 633 (2015) 1–7, http://dx.doi.org/10.1016/j.susc.2014.11.008 URL ⟨http://www.sciencedirect.com/science/article/pii/S0039602814003161⟩.
[211] J. Crowell, J. Chen, J.Y. Jr., Surf. Sci. 165(1)(1986) 37–64, http://dx.doi.org/10.1016/0039-6028(86)90663-1,URL ⟨http://www.sciencedirect.com/science/article/pii/0039602886906631⟩.
[212] R. Jaeger, H. Kuhlenbeck, H.-J. Freund, M. Wuttig, W. Hoffmann, R. Franchy, H. Ibach, Surf. Sci. 259 (3) (1991) 235–252, http://dx.doi.org/10.1016/0039-6028(91)90555-7 URL ⟨http://www.sciencedirect.com/science/article/pii/0039602891905557⟩.
[213] G. Kresse, M. Schmid, E. Napetschnig, M. Shishkin, L. Köhler, P. Varga, Science 308 (5727) (2005) 1440–1442, http://dx.doi.org/10.1126/science.1107783 URL ⟨http://www.sciencemag.org/content/308/5727/1440.abstract⟩.
[214] A. Rosenhahn, J. Schneider, J. Kandler, C. Becker, K. Wandelt, Surf. Sci. 433–435 (1999) 705–710, http://dx.doi.org/10.1016/S0039-6028(99)00126-0 URL ⟨http://www.sciencedirect.com/science/article/pii/S0039602899001260⟩.
[215] M. Yoshitake, S. Bera, Y. Yamauchi, Surf. Interface Anal. 35 (10) (2003) 824–828, http://dx.doi.org/10.1002/sia.1610.
[216] D.V. Potapenko, R.M. Osgood, Nano Letters 9 (6) (2009) 2378–2383, http://dx.doi.org/10.1021/nl900904s.
[217] M. De Santis, A. Buchsbaum, P. Varga, M. Schmid, Phys. Rev. B 84 (2011) 125430, http://dx.doi.org/10.1103/PhysRevB.84.125430 URL ⟨http://link.aps.org/doi/10.1103/PhysRevB.84.125430⟩.
[218] J.A. Stroscio, D.T. Pierce, R.A. Dragoset, Phys. Rev. Lett. 70 (1993) 3615–3618, http://dx.doi.org/10.1103/PhysRevLett.70.3615 URL ⟨http://link.aps.org/doi/10.1103/PhysRevLett.70.3615⟩.
[219] D. Pierce, J. Unguris, R. Celotta, M. Stiles, J. Magn. Magn. Mater. 200 (13) (1999) 290–321, http://dx.doi.org/10.1016/S0304-8853(99)00319-4 URL ⟨http://www.sciencedirect.com/science/article/pii/S0304885399003194⟩.
[220] M. Klaua, D. Ullmann, J. Barthel, W. Wulfhekel, J. Kirschner, R. Urban, T.L. Monchesky, A. Enders, J.F. Cochran, B. Heinrich, Phys. Rev. B 64 (2001) 134411, http://dx.doi.org/10.1103/PhysRevB.64.134411 URL ⟨http://link.aps.org/doi/10.1103/PhysRevB.64.134411⟩.
[221] R. Bertacco, S. De Rossi, F. Ciccacci, J. Vac. Sci. Technol. A 16 (4), (1998).
[222] F. Bonell, A.M. Bataille, S. Andrieu, C. Tiusan, B. Kierren, G. Lengaigne, D. Lacour, Eur. Phys. J. Appl. Phys. 43 (3) (2008) 357–361, http://dx.doi.org/10.1051/epjap:2008100.
[223] A. Picone, A. Brambilla, A. Calloni, L. Duò, M. Finazzi, F. Ciccacci, Phys. Rev. B 83 (2011) 235402, http://dx.doi.org/10.1103/PhysRevB.83.235402 URL ⟨http://link.aps.org/doi/10.1103/PhysRevB.83.235402⟩.
[224] J.-P. Lu, M.R. Albert, S.L. Bernasek, D.J. Dwyer, Surf. Sci. 215 (3) (1989) 348–362, http://dx.doi.org/10.1016/0039-6028(89)90265-3 URL ⟨http://www.sciencedirect.com/science/article/pii/0039602889902653⟩.
[225] A. Tange, C.L. Gao, B.Y. Yavorsky, I.V. Maznichenko, C. Etz, A. Ernst, W. Hergert, I. Mertig, W. Wulfhekel, J. Kirschner, Phys. Rev. B 81 (2010) 195410, http://dx.doi.org/10.1103/PhysRevB.81.195410 URL ⟨http://link.aps.org/doi/10.1103/PhysRevB.81.195410⟩.
[226] F. Donati, P. Sessi, S. Achilli, A. Li Bassi, M. Passoni, C.S. Casari, C. E. Bottani, A. Brambilla, A. Picone, M. Finazzi, L. Duò, M.I. Trioni,

F. Ciccacci, Phys. Rev. B 79 (2009) 195430, http://dx.doi.org/10.1103/PhysRevB.79.195430 URL ⟨http://link.aps.org/doi/10.1103/PhysRevB.79.195430⟩.
[227] A. Picone, G. Fratesi, A. Brambilla, P. Sessi, F. Donati, S. Achilli, L. Maini, M.I. Trioni, C.S. Casari, M. Passoni, A. Li Bassi, M. Finazzi, L. Duò, F. Ciccacci, Phys. Rev. B 81 (2010) 115450, http://dx.doi.org/10.1103/PhysRevB.81.115450 URL ⟨http://link.aps.org/doi/10.1103/PhysRevB.81.115450⟩.
[228] W. Hofer, J. Redinger, A. Biedermann, P. Varga, Surf. Sci 466 (13) (2000) L795–L801, http://dx.doi.org/10.1016/S0039-6028(00)00821-9 URL ⟨http://www.sciencedirect.com/science/article/pii/S0039602800008219⟩.
[229] J.A. Stroscio, D.T. Pierce, J. Vac. Sci. Technol. B 12 (3), (1994).
[230] H.W. Hugosson, W. Cao, S. Seetharaman, A. Delin, J. Phys. Chem. C 117 (12) (2013) 6161–6171, http://dx.doi.org/10.1021/jp3102496.
[231] P. Błoński, A. Kiejna, J. Hafner, Surf. Sci. 590 (1) (2005) 88–100, http://dx.doi.org/10.1016/j.susc.2005.06.011 URL ⟨http://www.sciencedirect.com/science/article/pii/S0039602805006539⟩.
[232] S.R. Chubb, W.E. Pickett, Phys. Rev. Lett. 58 (1987) 1248–1251, http://dx.doi.org/10.1103/PhysRevLett.58.1248 URL ⟨http://link.aps.org/doi/10.1103/PhysRevLett.58.1248⟩.
[233] K.O. Legg, F. Jona, D.W. Jepsen, P.M. Marcus, Phys. Rev. B 16 (1977) 5271–5276, http://dx.doi.org/10.1103/PhysRevB.16.5271 URL ⟨http://link.aps.org/doi/10.1103/PhysRevB.16.5271⟩.
[234] S.S. Parihar, H.L. Meyerheim, K. Mohseni, S. Ostanin, A. Ernst, N. Jedrecy, R. Felici, J. Kirschner, Phys. Rev. B 81 (2010) 075428, http://dx.doi.org/10.1103/PhysRevB.81.075428 URL ⟨http://link.aps.org/doi/10.1103/PhysRevB.81.075428⟩.
[235] R. Bertacco, F. Ciccacci, Phys. Rev. B 59 (1999) 4207–4210, http://dx.doi.org/10.1103/PhysRevB.59.4207 URL ⟨http://link.aps.org/doi/10.1103/PhysRevB.59.4207⟩.
[236] F. Bisio, R. Moroni, M. Canepa, L. Mattera, R. Bertacco, F. Ciccacci, Phys. Rev. Lett. 83 (1999) 4868–4871, http://dx.doi.org/10.1103/PhysRevLett.83.4868 URL ⟨http://link.aps.org/doi/10.1103/PhysRevLett.83.4868⟩.
[237] M. Nývlt, F. Bisio, J. Franta, C.L. Gao, H. Petek, J. Kirschner, Phys. Rev. Lett. 95 (2005) 127201, http://dx.doi.org/10.1103/PhysRevLett.95.127201 URL ⟨http://link.aps.org/doi/10.1103/PhysRevLett.95.127201⟩.
[238] W. Feng, H.L. Meyerheim, K. Mohseni, O. Brovko, V.S. Stepanyuk, N. Jedrecy, R. Felici, J. Kirschner, Phys. Rev. Lett. 110 (2013) 235503, http://dx.doi.org/10.1103/PhysRevLett.110.235503 URL ⟨http://link.aps.org/doi/10.1103/PhysRevLett.110.235503⟩.
[239] A.G. Sault, Appl. Surf. Sci. 74 (3) (1994) 249–262, http://dx.doi.org/10.1016/0169-4332(94)90006-X URL ⟨http://www.sciencedirect.com/science/article/pii/016943329490006X⟩.
[240] M. Seo, J. Lumsden, R. Staehle, Surf. Sci. 50 (2) (1975) 541–552, http://dx.doi.org/10.1016/0039-6028(75)90043-6 URL ⟨http://www.sciencedirect.com/science/article/pii/0039602875900436⟩.
[241] G.W. Simmons, D.J. Dwyer, Surf. Sci. 48 (2) (1975) 373–392, http://dx.doi.org/10.1016/0039-6028(75)90413-6 URL ⟨http://www.sciencedirect.com/science/article/pii/0039602875904136⟩.
[242] K. Freindl, E. Partyka-Jankowska, W. Karaś, M. Zając, E. Madej, N. Spiridis, M. Ślęzak, T. Ślęzak, D. Wiśnios, J. Korecki, Surf. Sci. 617 (2013) 183–191, http://dx.doi.org/10.1016/j.susc.2013.07.011 URL ⟨http://www.sciencedirect.com/science/article/pii/S0039602813002021⟩.
[243] J.A. Stroscio, D.T. Pierce, A. Davies, R.J. Celotta, M. Weinert, Phys. Rev. Lett. 75 (1995) 2960–2963, http://dx.doi.org/10.1103/PhysRevLett.75.2960 URL ⟨http://link.aps.org/doi/10.1103/PhysRevLett.75.2960⟩.
[244] M.M.J. Bischoff, T.K. Yamada, C.M. Fang, R.A. de Groot, H. van Kempen, Phys. Rev. B 68 (2003) 045422, http://dx.doi.org/10.1103/PhysRevB.68.045422 URL ⟨http://link.aps.org/doi/10.1103/PhysRevB.68.045422⟩.
[245] V.A. Ukraintsev, Phys. Rev. B 53 (1996) 11176–11185 http://dx.doi.org/10.1103/PhysRevB.53.11176 URL ⟨http://link.aps.org/doi/10.1103/PhysRevB.53.11176⟩.
[246] M. Passoni, F. Donati, A. Li Bassi, C.S. Casari, C.E. Bottani, Phys. Rev. B 79 (2009) 045404, http://dx.doi.org/10.1103/PhysRevB.79.045404 URL ⟨http://link.aps.org/doi/10.1103/PhysRevB.79.045404⟩.
[247] J. Middeke, R.-P. Blum, M. Hafemeister, H. Niehus, Surf. Sci. 587 (3) (2005) 219–228, http://dx.doi.org/10.1016/j.susc.2005.03.065 URL ⟨http://www.sciencedirect.com/science/article/pii/S0039602805005236⟩.
[248] D. Vlachos, S.D. Foulias, M. Kamaratos, J. Phys.: Condens. Matter 21 (44) (2009) 445004 URL ⟨http://stacks.iop.org/0953-8984/21/i=44/a=445004⟩.
[249] K. Amemiya, M. Sakamaki, Appl. Phys. Lett. 98 (1) (2011) 012501, http://dx.doi.org/10.1063/1.3531668 URL ⟨http://scitation.aip.org/content/aip/journal/apl/98/1/10.1063/1.3531668⟩.
[250] C. Wu, M.R. Castell, J. Goniakowski, C. Noguera, Phys. Rev. B 91 (2015) 155424, http://dx.doi.org/10.1103/PhysRevB.91.155424 URL ⟨http://link.aps.org/doi/10.1103/PhysRevB.91.155424⟩.
[251] A. Picone, G. Fratesi, M. Riva, G. Bussetti, A. Calloni, A. Brambilla, M. I. Trioni, L. Duò, F. Ciccacci, M. Finazzi, Phys. Rev. B 87 (2013) 085403, http://dx.doi.org/10.1103/PhysRevB.87.085403 URL ⟨http://link.aps.org/doi/10.1103/PhysRevB.87.085403⟩.
[252] A. Brambilla, G. Berti, A. Calloni, A. Picone, M. Riva, G. Bussetti, S. Nappini, E. Magnano, M. Finazzi, L. Duò, F. Ciccacci, J. Appl. Phys. 114 (12), (2013) 123905 http://dx.doi.org/10.1063/1.4822164, URL ⟨http://scitation.aip.org/content/aip/journal/jap/114/12/10.1063/1.4822164⟩.
[253] A. Davies, J.A. Stroscio, D.T. Pierce, R.J. Celotta, Phys. Rev. Lett. 76 (1996) 4175–4178, http://dx.doi.org/10.1103/PhysRevLett.76.4175 URL ⟨http://link.aps.org/doi/10.1103/PhysRevLett.76.4175⟩.
[254] B. Nonas, K. Wildberger, R. Zeller, P.H. Dederichs, Phys. Rev. Lett. 80 (1998) 4574–4577, http://dx.doi.org/10.1103/PhysRevLett.80.4574 URL ⟨http://link.aps.org/doi/10.1103/PhysRevLett.80.4574⟩.
[255] J.P. Perdew, K. Burke, M. Ernzerhof, Phys. Rev. Lett. 77 (1996) 3865–3868, http://dx.doi.org/10.1103/PhysRevLett.77.3865 URL ⟨http://link.aps.org/doi/10.1103/PhysRevLett.77.3865⟩.
[256] J. Goniakowski, C. Noguera, Phys. Rev. B 79 (2009) 155433 http://dx.doi.org/10.1103/PhysRevB.79.155433 URL ⟨http://link.aps.org/doi/10.1103/PhysRevB.79.155433⟩.
[257] A. Picone, G. Bussetti, M. Riva, A. Calloni, A. Brambilla, L. Duò, F. Ciccacci, M. Finazzi, Phys. Rev. B 86 (2012) 075465 http://dx.doi.org/10.1103/PhysRevB.86.075465 URL ⟨http://link.aps.org/doi/10.1103/PhysRevB.86.075465⟩.
[258] I.O. Thomas, A. Fortunelli, Eur. Phys. J. B 75 (1) (2010) 5–13, http://dx.doi.org/10.1140/epjb/e2010-00018-5 URL ⟨http://dx.doi.org/10.1140/epjb/e2010-00018-5⟩.
[259] M. Ondráček, F. Máca, J. Kudrnovský, J. Redinger, A. Biedermann, C. Fritscher, M. Schmid, P. Varga, Phys. Rev. B 74 (2006) 235437, http://dx.doi.org/10.1103/PhysRevB.74.235437 URL ⟨http://link.aps.org/doi/10.1103/PhysRevB.74.235437⟩.
[260] J.A. Venables, G.D.T. Spiller, M. Hanbucken, Rep. Prog. Phys. 47 (4)(1984) 399 URL ⟨http://stacks.iop.org/0034-4885/47/i=4/a=002⟩.
[261] T. Michely, J. Krug, Springer, 2004.
[262] H. Brune, Surf. Sci. Rep. 31 (46) (1998) 125–229, http://dx.doi.org/10.1016/S0167-5729(99)80001-6 URL ⟨http://www.sciencedirect.com/science/article/pii/S0167572999800016⟩.
[263] J. Evans, P. Thiel, M. Bartelt, Surf. Sci. Rep. 61 (12) (2006) 1–128, http://dx.doi.org/10.1016/j.surfrep.2005.08.004 URL ⟨http://www.sciencedirect.com/science/article/pii/S0167572906000021⟩.
[264] M. Copel, M.C. Reuter, E. Kaxiras, R.M. Tromp, Phys. Rev. Lett. 63 (1989) 632–635, http://dx.doi.org/10.1103/PhysRevLett.63.632 URL ⟨http://link.aps.org/doi/10.1103/PhysRevLett.63.632⟩.
[265] J. Camarero, J. Ferrón, V. Cros, L. Gómez, A.L. Vázquez de Parga, J. M. Gallego, J.E. Prieto, J.J. de Miguel, R. Miranda, Phys. Rev. Lett. 81 (1998) 850–853, http://dx.doi.org/10.1103/PhysRevLett.81.850 URL ⟨http://link.aps.org/doi/10.1103/PhysRevLett.81.850⟩.
[266] J. Ferrón, L. Gómez, J. Gallego, J. Camarero, J. Prieto, V. Cros, A.V. de Parga, J. de Miguel, R. Miranda, Surf. Sci. 459 (12) (2000) 135–148, http://dx.doi.org/10.1016/S0039-6028(00)00459-3 URL ⟨http://www.sciencedirect.com/science/article/pii/S0039602800004593⟩.
[267] M.C.G. Passeggi, J.E. Prieto, R. Miranda, J.M. Gallego, Phys. Rev. B 65 (2001) 035409, http://dx.doi.org/10.1103/PhysRevB.65.035409 URL ⟨http://link.aps.org/doi/10.1103/PhysRevB.65.035409⟩.
[268] J.A. Stroscio, D.T. Pierce, M.D. Stiles, A. Zangwill, L.M. Sander, Phys. Rev. Lett. 75 (1995) 4246–4249, http://dx.doi.org/10.1103/

PhysRevLett.75.4246 URL ⟨http://link.aps.org/doi/10.1103/PhysRevLett.75.4246⟩.
[269] P. Bonanno, M. Canepa, P. Cantini, R. Moroni, L. Mattera, S. Terreni, Surf. Sci. 454–456 (2000) 697–701, http://dx.doi.org/10.1016/S0039-6028(00)00114-X URL ⟨http://www.sciencedirect.com/science/article/pii/S003960280000114X⟩.
[270] M. Kamiko, H. Mizuno, H. Chihaya, J. Xu, I. Kojima, R. Yamamoto, Thin Solid Films 515 (18) (2007) 7203–7208, http://dx.doi.org/10.1016/j.tsf.2007.02.105 URL ⟨http://www.sciencedirect.com/science/article/pii/S0040609007002799⟩.
[271] J. Vrijmoeth, H.A. van der Vegt, J.A. Meyer, E. Vlieg, R.J. Behm, Phys. Rev. Lett. 72 (1994) 3843–3846, http://dx.doi.org/10.1103/PhysRevLett.72.3843 URL ⟨http://link.aps.org/doi/10.1103/PhysRevLett.72.3843⟩.
[272] S. Esch, M. Hohage, T. Michely, G. Comsa, Phys. Rev. Lett. 72 (1994) 518–521, http://dx.doi.org/10.1103/PhysRevLett.72.518 URL ⟨http://link.aps.org/doi/10.1103/PhysRevLett.72.518⟩.
[273] M. Riva, A. Picone, D. Giannotti, A. Brambilla, G. Fratesi, G. Bussetti, L. Duò, F. Ciccacci, M. Finazzi, Phys. Rev. B 92 (2015) 115434, http://dx.doi.org/10.1103/PhysRevB.92.115434 URL ⟨http://link.aps.org/doi/10.1103/PhysRevB.92.115434⟩.
[274] A. Tange, C. Gao, W. Wulfhekel, J. Kirschner, Phys. Rev. B 81 (2010) 220404, http://dx.doi.org/10.1103/PhysRevB.81.220404 URL ⟨http://link.aps.org/doi/10.1103/PhysRevB.81.220404⟩.
[275] L. Li, A. Kida, M. Ohnishi, M. Matsui, Surf. Sci. 493 (13) (2001) 120–125, http://dx.doi.org/10.1016/S0039-6028(01)01198-0 URL ⟨http://www.sciencedirect.com/science/article/pii/S0039602801011980⟩.
[276] R. Nünthel, T. Gleitsmann, P. Poulopoulos, A. Scherz, J. Lindner, E. Kosubek, C. Litwinski, Z. Li, H. Wende, K. Baberschke, S. Stolbov, T. Rahman, Surf. Sci. 531 (1) (2003) 53–67, http://dx.doi.org/10.1016/S0039-6028(03)00438-2 URL ⟨http://www.sciencedirect.com/science/article/pii/S0039602803004382⟩.
[277] H.L. Meyerheim, D. Sander, R. Popescu, W. Pan, I. Popa, J. Kirschner, Phys. Rev. Lett. 99 (2007) 116101, http://dx.doi.org/10.1103/PhysRevLett.99.116101 URL ⟨http://link.aps.org/doi/10.1103/PhysRevLett.99.116101⟩.
[278] A. Calloni, A. Picone, A. Brambilla, M. Finazzi, L. Duò, F. Ciccacci, Surf. Sci. 605 (2324) (2011) 2092–2096, http://dx.doi.org/10.1016 /j.susc.2011.08.013 URL ⟨http://www.sciencedirect.com/science/article/pii/S0039602811003499⟩.
[279] M. Riva, A. Picone, G. Bussetti, A. Brambilla, A. Calloni, G. Berti, L. Duò, F. Ciccacci, M. Finazzi, Surf. Sci. 621 (2014) 55–63, http://dx.doi.org/10.1016/j.susc.2013.10.016 URL ⟨http://www.sciencedirect.com/science/article/pii/S0039602813003129⟩.
[280] A. Calloni, G. Berti, A. Brambilla, M. Riva, A. Picone, G. Bussetti, M. Finazzi, F. Ciccacci, L. Duò, J. Phys.: Condens. Matter 26 (44) (2014) 445001 URL ⟨http://stacks.iop.org/0953-8984/26/i=44/a=445001⟩.
[281] Y. Kim, C. Westphal, R. Ynzunza, Z. Wang, H. Galloway, M. Salmeron, M.V. Hove, C. Fadley, Surf. Sci. 416 (12) (1998) 68–111, http://dx.doi.org/10.1016/S0039-6028(98)00506-8 URL ⟨http://www.sciencedirect.com/science/article/pii/S0039602898005068⟩.
[282] M. Finazzi, L. Duò, F. Ciccacci (Eds.), Wiley-VCH Verlag GmbH & Co. KGaA, Weinheim, 2010. http://dx.doi.org/10.1002/9783527630370.
[283] S. Masuda, Y. Harada, H. Kato, K. Yagi, T. Komeda, T. Miyano, M. Onchi, Y. Sakisaka, Phys. Rev. B 37 (1988) 8088–8095, http://dx.doi.org/10.1103/PhysRevB.37.8088 URL ⟨http://link.aps.org/doi/10.1103/PhysRevB.37.8088⟩.
[284] Y. Joseph, W. Ranke, W. Weiss, J. Phys. Chem. B 104 (14) (2000) 3224–3236, http://dx.doi.org/10.1021/jp9932012.
[285] A. Rota, S. Altieri, S. Valeri, Phys. Rev. B 79 (2009) 161401, http://dx.doi.org/10.1103/PhysRevB.79.161401 URL ⟨http://link.aps.org/doi/10.1103/PhysRevB.79.161401⟩.
[286] M. Busch, M. Gruyters, H. Winter, Surf. Sci. 600 (13) (2006) 2778–2784, http://dx.doi.org/10.1016/j.susc.2006.05.003 URL ⟨http://www.sciencedirect.com/science/article/pii/S0039602806005991⟩.
[287] M. Soldemo, Y. Niu, A. Zakharov, E. Lundgren, J. Weissenrieder, Surf. Sci. 639 (2015) 13–19, http://dx.doi.org/10.1016/j.susc.2015.04.008 URL ⟨http://www.sciencedirect.com/science/article/pii/S0039602815000990⟩.
[288] D. Cappus, M. Haßel, E. Neuhaus, M. Heber, F. Rohr, H.-J. Freund, Surf. Sci. 337 (3) (1995) 268–277, http://dx.doi.org/10.1016/0039-6028(95)00624-9 URL ⟨http://www.sciencedirect.com/science/article/pii/0039602895006249⟩.
[289] H. Nishimura, T. Tashiro, T. Fujitani, J. Nakamura, J. Vac. Sci. Technol. A 18 (4), (2000).
[290] W. Meyer, D. Hock, K. Biedermann, M. Gubo, S. Müller, L. Hammer, K. Heinz, Phys. Rev. Lett. 101 (2008) 016103, http://dx.doi.org/10.1103/PhysRevLett.101.016103 URL ⟨http://link.aps.org/doi/10.1103/PhysRevLett.101.016103⟩.
[291] W. Ranke, M. Ritter, W. Weiss, Phys. Rev. B 60 (1999) 1527–1530, http://dx.doi.org/10.1103/PhysRevB.60.1527 URL ⟨http://link.aps.org/doi/10.1103/PhysRevB.60.1527⟩.
[292] H. Zeuthen, W. Kudernatsch, G. Peng, L.R. Merte, L.K. Ono, L. Lammich, Y. Bai, L.C. Grabow, M. Mavrikakis, S. Wendt, F. Besenbacher, J. Phys. Chem. C 117 (29) (2013) 15155–15163, http://dx.doi.org/10.1021/jp4042638.
[293] C. Noguera, J. Phys.: Condens. Matter 12 (31) (2000) R367 URL ⟨http://stacks.iop.org/0953-8984/12/i=31/a=201⟩.
[294] J. Goniakowski, F. Finocchi, C. Noguera, Rep. Prog. Phys. 71 (1) (2008) 016501 URL ⟨http://stacks.iop.org/0034-4885/71/i=1/a=016501⟩.